

UNCLASSIFIED

AD NUMBER

AD819301

NEW LIMITATION CHANGE

TO

Approved for public release, distribution  
unlimited

FROM

Distribution authorized to U.S. Gov't.  
agencies and their contractors; Critical  
Technology; Aug 1967. Other requests shall  
be referred to AFRPL [RPPR-STINFO],  
Edwards AFB, CA 93523.

AUTHORITY

AFRPL ltr, 27 Oct 1971

THIS PAGE IS UNCLASSIFIED

This Document  
Reproduced From  
Best Available Copy

AFRPL-TR-67-211 - VOL II

AD819301

PROJECT SOPHY - SOLID PROPELLANT HAZARDS PROGRAM  
Volume II -- Appendixes

R. B. Elwell  
O. R. Irwin  
R. W. Vail, Jr.  
Aerojet-General Corporation

TECHNICAL REPORT AFRPL-TR-67-211 - VOL II

August 1967

"This document is subject to special export controls and each transmittal to foreign governments or foreign nationals may be made only with prior approval of AFRPL (RPPR-STINFO), Edwards, California 93523."

Air Force Rocket Propulsion Laboratory  
Research and Technology Division  
Edwards Air Force Base, California  
Air Force Systems Command, United States Air Force

## **REPRODUCTION QUALITY NOTICE**

**This document is the best quality available. The copy furnished to DTIC contained pages that may have the following quality problems:**

- **Pages smaller or larger than normal.**
- **Pages with background color or light colored printing.**
- **Pages with small type or poor printing; and or**
- **Pages with continuous tone material or color photographs.**

**Due to various output media available these conditions may or may not cause poor legibility in the microfiche or hardcopy output you receive.**



**If this block is checked, the copy furnished to DTIC contained pages with color printing, that when reproduced in Black and White, may change detail of the original copy.**

**(This document contains  
blank pages that were  
not filmed)**

## NOTICES

"When U. S. Government drawings, specifications, or other data are used for any purpose other than a definitely related Government procurement operation, the Government thereby incurs no responsibility nor any obligation whatsoever, and the fact that the Government may have formulated, furnished or in any way supplied the said drawings, specifications, or other data, is not to be regarded by implication or otherwise, as in any manner licensing the holder or any other person or corporation, or conveying any rights or permission to manufacture, use, or sell any patented invention that may in any way be related thereto."

**PROJECT SOPHY - SOLID PROPELLANT HAZARDS PROGRAM**  
**Volume II -- Appendixes**

R. B. Elwell  
O. R. Irwin  
R. W. Vail, Jr.

"This document is subject to special export controls and  
each transmittal to foreign governments or foreign nationals  
may be made only with prior approval of AFRPL (RPPR-STINFO),  
Edwards, California 93523."

## TABLE OF CONTENTS

Appendix No.		Page No.
I.	One-Dimensional Lattice Model of Detonation in Heterogeneous Explosives.....	1
II.	Comments on the RUBY Code.....	25
III.	Test CD-96 Data.....	39
IV.	Jetting Phenomenon.....	45
V.	Critical Geometry Data, AAB-3189.....	61
VI.	Microscopic Methods for Determining Void Content.....	67
VII.	Shock Pressure Attenuation in Plexiglas...	75
VIII.	Shock Pressure and Wave Area Data.....	81
IX.	Flyer Plate Data.....	85
X.	Combined Blast Data.....	91
	DISTRIBUTION.....	137
	DD FORM 1473.....	147

## APPENDIX I

### One-Dimensional Lattice Model of Detonation in Heterogeneous Explosives

R. F. Chaiken  
Technical Consultant  
Aerojet-General Corporation  
Downey, California

#### INTRODUCTION

The problem of defining the reaction-zone in detonating heterogeneous explosives is of prime concern in critical diameter studies. This arises from the fact that the reaction-zone length and the related detonation reaction time determine the space-time region where chemical support of the detonation front occurs. Hence, the detonation reaction-zone and the detonation reaction time likewise establish, in part, the rates of energy loss by side expansion which would be required to extinguish the detonation.

Eyring (Reference I-1), in his classical grain burning theory, suggested that for granular explosives the detonation reaction time can be expressed as

$$\tau_r = \frac{R_g}{\lambda k_r} \quad (I-1)$$

where

$\tau_r$  = detonation reaction time

$R_g$  = average radius of the explosive granules

$\lambda$  = thickness of a monolayer of explosive

$(k_r)^{-1}$  = lifetime of an explosive molecule

For the case of ammonium nitrate and ammonium perchlorate explosives, this grain burning expression was modified by Andersen and Chaiken (References I-2 and I-3), who suggested that  $\lambda k_r$  in these cases is the linear pyrolysis rate,  $B$ , of the solid under high surface heat-flux conditions.

Furthermore, these authors pointed out that the Eyring grain burning expression implicitly assumes that ignition of grain burning occurs instantaneously after passage of the detonation front; however, under certain conditions, the time of ignition may be significant in establishing the detonation reaction time. In this connection, it was suggested that the expression for  $\tau_r$  be modified to include a grain burning ignition time, i.e.,

$$\tau_r = \tau_o + \tau_b \quad (I-2)$$

where

$\tau_o$  = time to ignition of grain burning

$\tau_b$  = grain burning time (Equation I-1)

The requirement of an ignition time in any complete expression for  $\tau_r$  becomes clear when we consider the case of a heterogeneous explosive in the limit of  $R_g \rightarrow 0$ . In this limit, the explosive becomes homogeneous in nature, and  $\tau_r$  from Equation I-2 would become identical to the ignition time,  $\tau_o$ . Indeed, this is believed to be the case for liquid explosives such as nitromethane (References I-4 and I-5).

However, while  $\tau_r$  may be clearly defined in the limit of negligible  $\tau_o$  or negligible  $\tau_b$ , it is certainly not clearly defined when  $\tau_o$  and  $\tau_b$  are of comparable magnitude. In these cases, the simple addition rule of Equation I-2 does not obviously account for the fact that the ignition and grain burning reactions might proceed simultaneously, rather than consecutively; hence, its applicability to defining the detonation reaction-zone is questionable.

It is the purpose of this paper to describe a model of the detonation reaction-zone which treats ignition as an integral part of the detonation reaction. The model utilizes the concepts of both the Bowden hot-spot ignition theory and the Eyring grain burning theory, and enables the derivation of an expression for  $\tau_r$  in which the physical significance of  $\tau_o$  and its relationship to  $\tau_b$  is more clearly defined. The expression for detonation reaction time also appears to have direct applicability to the detonation of solid composite propellants.

## ONE-DIMENSIONAL LATTICE MODEL

### Development of the Model

In the discussions that follow, it is considered that a heterogeneous explosive is a lattice network, composed of initiation sites of finite volume connected by a continuous medium. When a detonation front overtakes a region in the explosive, the initiating sites react to form hot spots. The formation of a hot spot is accompanied (with zero delay) by a reaction growing from the hot spot and spreading into the continuum. Complete reaction of the lattice network defines the detonation reaction-zone.

For a one-dimensional treatment of the lattice model, the continuum reaction rate is assumed to be described by a constant linear velocity,  $B$ . The initiating sites may be of different types ( $i$ ) characterized by a length  $L_i$  and a reaction rate constant  $k_i$ . The lattice at any time  $t$  from the instant of passage of the detonation front will consist of  $N_i(t)$  sites of type  $i$  per unit length and  $N^*_T(t) = \sum N_i^*(t)$  total hot spots per unit length. Assuming hot spot formation to be a first-order kinetic process, the rate of formation of hot spots is given by

$$dN_i^*(t)/dt = k_i N_i(t) \quad (I-3a)$$

and

$$dN_T^*(t)/dt = \sum_i \frac{dN_i^*(t)}{dt} = \sum_i k_i N_i(t) \quad (I-3b)$$

where  $k_i$  is the rate constant  $(\text{sec})^{-1}$  for formation of the hot spot and  $(k_i)^{-1}$  can be considered as an ignition time for the  $i$ th type of initiating site.

At time  $t = \Phi$ , the number of hot spots formed is simply

$$dN_T^*(t) = \sum_i dN_i^*(\Phi) = \sum_i k_i N_i(\Phi) d\Phi \quad (I-4)$$

At time  $t > \Phi$ , the total fraction of lattice consumed by formation of and reaction spreading from the  $dN_T^*(\Phi)$  hot spots is

$$df(\Phi) = \sum_i [2B(t-\Phi) + L_i] dN_i^*(\Phi) \quad (I-5)$$

or

$$df(\Phi) = 2B(t-\Phi) \sum_i k_i N_i(\Phi) d\Phi + \sum_i L_i k_i N_i(\Phi) d\Phi \quad (I-6)$$

The total fraction of lattice that is consumed by reaction spreading from all hot spots formed for all values of  $\phi$  up to  $\phi = t$  is then

$$f(t) = \int_{\phi=0}^{\phi=t} df(\phi) = 2B \sum k_i \int_{\phi=0}^{\phi=t} (t-\phi) N_i(\phi) d\phi + \sum L_i k_i \int_{\phi=0}^{\phi=t} N_i(\phi) d\phi \quad (I-7)$$

or

$$f(t) = 2B \sum \int_0^{N^*_i(t)} (t-\phi) dN^*_i(\phi) + \sum L_i \int_0^{N^*_i(t)} dN^*_i(\phi) \quad (I-8)$$

The rate of lattice reaction is given by the time derivative of Equation I-8 which yields

$$\frac{df(t)}{dt} = 2BN^*_T(t) + \sum L_i \frac{dN^*_i(t)}{dt} \quad (I-9)$$

The detonation reaction time,  $\tau_r$ , can be defined as  $t = \tau_r$  when  $f(t) = 1$ .

Integrating Equation I-9, i.e.,

$$\int_{f(0)=0}^{f(\tau_r)=1} df(t) = 2B \int_{t=0}^{t=\tau_r} N^*_T(t) dt + \sum L_i \int_{t=0}^{t=\tau_r} dN^*_i(t) \quad (I-10)$$

therefore yields

$$1 = 2B \int_0^{\tau_r} N^*_T(t) dt + \sum L_i N^*_i(\tau_r) \quad (I-11)$$

which in terms of a time-averaged concentration of hot spots,  $\bar{N}^*_T$ , becomes

$$\frac{1}{\tau_r} = 2B\bar{N}^*_T + \frac{1}{\tau_r} \sum L_i N^*_i (\tau_r) \quad (I-12)$$

or

$$\tau_r = \frac{1}{2B\bar{N}^*_T} \left[ 1 - \sum L_i N^*_i (\tau_r) \right] \quad (I-13)$$

where

$$\bar{N}^*_T = \frac{1}{\tau_r} \int_0^{\tau_r} N^*_T(t) dt \quad (I-14)$$

It is interesting to note that when the hot spots have no dimension, and when the average concentration of hot spots is considered to be the concentration of explosive granules, Equation I-13 reduces directly to the grain-burning expression which was suggested for ammonium nitrate and ammonium perchlorate explosives (References I-2 and I-3), i.e.,

$$\tau_r = \bar{R}_g / D \quad (I-15)$$

The equivalence of Equations I-13 and I-15 is readily seen by recognizing that in this case  $(N^*_T)^{-1}$  is simply the average distance between the centers of the explosive granules.

The question now arises as to the effect of finite ignition times on  $\tau_r$ . It is apparent that a finite  $\tau_0$  will modify the value of  $N^*_T(t)$  in Equation I-14. Thus we must obtain an expression for  $N^*_T(t)$  which, from Equation I-3, depends upon the time distribution of initiating sites.

Now the total rate of decrease of type  $i$  initiating sites is given by

$$\frac{-dN_i}{dt} = k_i N_i + \frac{N_i df(t)}{dt} \quad (I-16)$$

The first term in the above rate expression is simply the first-order activation process to form hot spots, while the second term is the rate of destruction of initiating sites by action of the

continuum reaction. That is, when the continuum reaction overtakes an initiating site, that site number is no longer available to form a hot spot.

Substituting Equation I-9 into I-14 we obtain

$$\frac{-dN_i}{dt} = k_i N_i + N_i \left[ 2BN^*_T + \sum L_i \frac{dN^*_i(t)}{dt} \right] \quad (I-17)$$

Summing over all  $i$  and utilizing Equation I-3, Equation I-17 becomes a phaffian differential equation in more than two variables, i.e.,

$$dN_T + (1+N_T L) dN^*_T + 2BN^*_T N_T dt = 0 \quad (I-18)$$

where  $N_T = \sum N_i$ , the total concentration of initiating sites, and  $L = \sum L_i dN^*_i / \sum dN^*_i$ , the number average length of a hot spot.

Unfortunately, Equation I-18 does not lend itself to ready solution. At this time, however, an approximation approach will be pursued which should have some applicability to those cases where only sites with ignition times less than  $\tau_r$  (i.e.,  $k_{it}\tau_r > 1$ ) need be considered.

#### Approximation Solution for Sites with Ignition Times Smaller than the Detonation Reaction Time

In the approximation approach, it is assumed that the major loss of initiating sites is through self activation to form hot spots. Hence, Equation I-16 can be written as

$$\frac{-dN_i}{dt} \approx k_i N_i \quad (I-19)$$

or

$$N_i(t) = N_{i0} \exp(-k_i t) \quad (I-20)$$

Where  $N_{i0}$  is the initial concentration of the  $i$ th type initiating site. Substitution of Equation I-20 into Equation I-4 and solving for  $N^*_T(t)$  yields

$$N^*_T(t) = \sum N_{i0} (1 - e^{-k_i t}) \quad (I-21)$$

The average concentration of hot spots is given by

$$\bar{N}^k_T = (1/\tau_r) \left\{ N_{io} \tau_r + \sum_i \frac{N_{io}}{k_i} \left[ \exp(-k_i \tau_r) - 1 \right] \right\} \quad (I-22)$$

Comparing the above expression with Equation I-13 finally yields

$$\tau_r = \frac{1}{2BN_{To}} \left[ 1 - \sum_i L_i N^k_i(\tau_r) \right] + \sum_i \frac{F_i}{k_i} \left[ 1 - \exp(-k_i \tau_r) \right] \quad (I-23)$$

where  $N_{To} = \sum_i (N_i)_o$ , and  $F_i = (N_i)_o / N_{To}$  is the initial fraction of the  $i^{th}$  type of initiating site. It should be emphasized that the only sites to be considered in Equation I-23 are those for which  $k_i \tau_r > 1$ , since it is only for these sites that the approximation of Equation I-19 can be valid. Within this constraint, the value of  $N^k_i(\tau_r)$  is  $\sim (N_i)_o$  (i.e., each site leads to a hot spot), and the term  $[1 - \exp(-k_i \tau_r)]$  is  $\approx 1$ . Hence, a reasonable approximation to Equation I-23 is

$$\tau_r = \frac{1}{2B} \left[ \frac{1}{N_{To}} - \sum_{i=1}^n \frac{L_i N_{io}}{N_{To}} \right] + \sum_{i=1}^n \frac{N_{io}}{k_i N_{To}} \quad (I-24)$$

or

$$\tau_r = \frac{(S/n) - L}{2B} + \bar{\tau}_o \quad (I-25)$$

Here,  $n$  is the number of different types of initiating sites and  $S = n/N_{To}$ ,  $L = \sum_i L_i N_{io}/N_{To}$ ,  $\bar{\tau}_o = \sum_i N_{io}/k_i N_{To}$  are simply number-weighted average parameters of the initiating sites; viz., the distance between centers ( $S$ ), the length ( $L$ ), and the ignition time ( $\bar{\tau}_o$ ).

The above expression for the detonation reaction time is now in a form that can be readily applied to various explosive situations.

#### **APPLICATION OF APPROXIMATION APPROACH TO EXPLOSIVE SYSTEMS CONTAINING ONE AND TWO TYPES OF INITIATING SITES**

##### **Case of a Single Type of Initiating Site ( $n = 1$ )**

Let us consider an explosive with only one type of initiating site which meets the criterion  $k_i \tau_r > 1$ . In this case  $n = 1$  and the number weighted average site parameters in Equation I-25 become

actual site parameters, i.e.,

$$\tau_r = \frac{1}{2B} [S - L] + \tau_0 \quad (I-26)$$

The similarity between the above expression and Equation I-2 is obvious, suggesting that the simple addition rule is reasonably applicable in this case. It should be noted that Equation I-26 extrapolates to the expected  $\tau_r$  for both negligible ignition time and for negligible grain burning time. The latter extrapolation is expected to be applicable to the case of homogeneous explosives, which can now be considered as those explosives where  $(S - L) \approx 0$ . This might be expected when S, and hence L, approach molecular dimensions.

In the case of finite size initiating sites ( $\tau_0$ , still negligible) Equation I-26 is identical to the detonation reaction time expression used at Aerojet (Reference I-7) to describe detonation in 2 to 10% RDX-adulterated solid composite propellant. In this case, it was considered that the RDX particles would act as initiating sites, and that the propellant medium separating the RDX would act as the grain burning continuum. The reaction time expression was derived in terms of the mass fraction,  $f_{RDX}$ , of RDX particles, i.e.,

$$\tau_r = \frac{L_{RDX}}{2B} \left[ \left( \frac{\pi \rho_{RDX}}{6 \rho_f RDX} \right)^{1/3} - 1 \right] \quad (I-27)$$

where  $\rho$  and  $\rho_{RDX}$  are the propellant and RDX densities, respectively, and  $L_{RDX}$  the diameter of the RDX particles. It can be readily shown that for spherical RDX particles the bracketed term in the above expression is identical with  $(S/L - 1)^{1/3}$ .

It is noteworthy that the use of Equation I-27 has led to a successful correlation of the critical diameter of solid composite propellants as a function of  $f_{RDX}$  in the range  $0.02 \leq f \leq 0.1$  (Reference I-7).

\*Since  $N_{To}$  is the number of RDX particles per unit length, it is also equal to the cube root of the number of RDX particles per unit of propellant volume.

Case of Two Types of Initiating Sites ( $n = 2$ )

For this case, Equation I-25 can be expressed directly as

$$\tau_r = \frac{1}{2B(N_{1o} + N_{2o})} - \frac{F_i(L_1 - L_2)}{2B} + F_i(\tau_{1c} - \tau_{2o}) + \tau_{2o} \quad (I-28)$$

where  $F_i = N_{io}/N_{To}$  is the number fraction of sites of type  $i$  initially present (i.e.,  $\sum F_i = 1$ ).

It is interesting to examine the above expression in light of the previous work at Aerojet (Reference I-7), in which Equation I-27 was modified to account for the effect of inherent initiating sites on the detonation reaction time of solid composite propellant containing only small amounts of RDX (i.e.,  $f_{RDX} < 0.02$ ). Here, it was suggested that the inherent sites (e.g., flaws, voids) acted as an additional weight fraction  $c$  of RDX particles. Therefore, Equation I-27 becomes

$$\tau_r = \frac{L_{RDX}}{2B} \left[ \left( \frac{\pi^p RDX}{6P(f_{RDX} + c)} \right)^{1/3} - 1 \right] \quad (I-29)$$

or

$$\tau_r = \frac{C_1}{(f_{RDX} + c)^{1/3}} - C_2 \quad (I-30)$$

In the same terminology, Equation I-28 (assuming negligible ignition times) yields

$$\tau_r = \frac{L_{RDX}}{2B} \left[ \frac{(\pi^p RDX/6P)^{1/3}}{(f_{RDX})^{1/3} + c'} - \frac{f_{RDX}^{1/3} + c' (L_x/L_{RDX})}{(f_{RDX})^{1/3} + c'} \right] \quad (I-31)$$

where  $c' = (f_x P_{RDX}/\rho_x)^{1/3} (L_{RDX}/L_x)$ , the subscript  $x$  referring to the inherent initiating sites. Since Equation I-31 has the form of

$$\tau_r = \frac{C_1 - C_3 (f_{RDX}^{1/3} + C_4)}{(f_{RDX})^{1/3} + c'} \quad (I-32)$$

It is evident that Equation I-31 and the Aerojet expression given by Equations I-29 or I-30 are not equivalent. In the inherent sites in Equation I-31 are assumed to have a diameter and density equivalent to that of RDX, the 1-D lattice expression for  $\tau_r$  reduces to

$$\tau_r = \frac{L_{RDX}}{2B} \left[ \frac{(\pi r_{RDX}/6\rho)^{1/3}}{(f_{RDX})^{1/3} + c'} - 1 \right] = \frac{C_1}{(f_{RDX})^{1/3} + c'} \quad (I-33)$$

This expression while similar to Equation I-30 is still not identical to it except in the limit of  $f_{RDX} = 0$ . A more detailed quantitative comparison between these various reaction time expressions will be given in a later section of this report when critical diameter data are discussed.

#### Case Where the Number of Types of Sites Varies with $\tau_r$

It was emphasized earlier that the general Equations I-24 and I-25 were applicable only to systems with initiating sites that form hot-spots in a time less than the reaction time (i.e.,  $k_i\tau_r > 1$ ). Also, it was shown in the previous sections that the reaction time will generally increase as the concentration of one type of site decreases (e.g., the case of RDX adulterated propellant). Hence, a possible situation presents itself in which an explosive with many potential types of initiating sites has only one type of site active at short reaction times, but as conditions change to increase the reaction time (e.g., decrease in loading density or decrease in primary hot-spot concentration), other sites become active. This phenomena may have implications with respect to the contrasting behavioral patterns in high explosives that is discussed in Price (Reference I-8) as well as with respect to the role of inherent impurities in the case of RDX-adulterated propellants.

In the simplest case, where only two types of sites are considered and where the concentration of the primary site is being varied, the expression for the detonation reaction time might be described in terms of three different regions of  $\tau_r$ , viz.,

##### a. Primary Region:

$\tau_{10} < \tau_r < \tau_{20}$ , corresponding to significant values of  $N_{10}$ :

$\tau_r$  is simply given by Equation I-26, i.e.,

$$\tau_r = \frac{1}{2BN_{1o}} - \frac{L_1}{2B} + \tau_{1o} \quad \underline{\tau_{1o} \ll \tau_r} \quad (I-34)$$

$$\tau_r = \frac{1}{2B} \left( \frac{1}{N_{1o}} - L_1 \right) \quad (I-35)$$

b. Transition region:

$\tau_{1o} \ll \tau_r \approx \tau_{2o}$ , corresponding to small values of  $N_{1o}$ :

Under this set of conditions, Equation I-28 is approximated by

$$\tau_r = \frac{1}{2BN_{1o}} \left[ 1 - L_1 N_{1o} - L_2 N_{2o} \right] \quad (I-36)$$

Since  $L_1 N_{1o} \ll L_2 N_{2o}$ , this equation can be written as

$$\tau_r = \frac{1}{2BN_{1o}} \left[ 1 - L_2 N_{2o} \right] \quad (I-37)$$

c. Secondary region:

$\tau_{1o} < \tau_{2o} < \tau_r$ , corresponding to negligible values of  $N_{1o}$ :

Again,  $\tau_r$  is simply given by Equation I-26, i.e.,

$$\tau_r = \frac{1}{2BN_{2o}} - \frac{L_2}{2B} + \tau_{2o} \quad (\tau_{2o} \ll \tau_r) \quad (I-38)$$

$$= \frac{1}{2B} \left[ \frac{1}{N_{2o}} - L_2 \right] \quad (I-39)$$

### CORRELATION OF EXPERIMENTAL CRITICAL DIAMETER DATA

In Reference I-7 it was shown by both theoretical and experimental arguments that the critical diameter,  $d_c$ , of RDX adulterated solid composite propellant<sup>2</sup> should be directly proportional to the detonation reaction time at the critical detonation velocity, i.e.,

$$d_c = K(\tau_r)_c \quad (I-40)$$

<sup>2</sup>Conventional propellant based upon AP, Al, and rubber binder in which varying amounts of AP were replaced by RDX (15  $\mu$  particles).

where  $K$  is a proportionality factor which remains relatively constant over an RDX range of 0 to 10%.

Also described in Reference I-7 as well as in Reference I-9 are experimental critical diameter data for RDX adulterated propellant in which  $d_c$  was varied from  $\sim 2$  in. to  $\sim 70$  in. as the RDX content was varied from  $\sim 10\%$  to 0%.<sup>3</sup> The reported critical diameter data are shown in Table I-I.

It is interesting to examine these data in light of Equation I-41 and the expressions for  $\tau_r$  which were derived in the preceding sections.

#### Case of a Single Initiating Site

If the RDX particles are the sole source of initiating sites then the expression for the reaction time becomes that given by Equation I-27. Combining this expression with Equation I-40 then yields an expression for  $d_c$  of the form

$$d_c = \frac{K_1}{(f_{RDX})^{1/3}} - K_2 \quad (I-41)$$

As noted earlier, Equation I-41 is identical to that derived in Reference I-7. A best experimental fit to the data was reported when  $K_1 = 15.3$  and  $K_2 = -30.9$  ( $d_c$  in in.). The best fit of the data in Table I-I with Equation I-41 is shown in Figure I-1. It is readily seen that in the range of  $f_{RDX} > 0.02$ , Equation I-41 fits the data quite well; however, at lower values of  $f_{RDX}$ , the theoretical curve (based upon the best values of  $K_1$  and  $K_2$ ) predicts values of  $d_c$  which are too large. This fact combined with the fact that  $d_c$  approaches infinity as  $f_{RDX}$  approaches zero led O. R. Irwin at Aerojet (Reference I-7) to suggest that there were additional initiating sites inherent to the propellant which act as an effective constant weight fraction of RDX (see Equation I-29).

In any case it would appear from Figure I-1 that all the experimental  $d_c$  data can not be correlated by the  $\tau_r$  expression for a single type of initiating site.

<sup>3</sup>This work was carried out by Aerojet-General Corporation as part of the Air Force Solid Propellant Hazards Program (Project SOPHY).

Table I-I. Experimental Critical Diameter Data for  
RDX-Adulterated Solid Composite Propellant  
(References I-7 and I-9).

Mass Fraction of RDX $(f_{RDX})$	Critical Diameter $(d_c)$ (in.)	$(f_{RDX})^{1/3}$
0.10	2.12	0.4642
0.092	2.66	0.4514
0.071	5.25	0.4141
0.0475	11.25	0.3621
0.021	23.5	0.2759
0.00375	48.0	0.1554
0	{60 (No Go)} 72 (Go)*	0

\*Results of one test at each diameter.

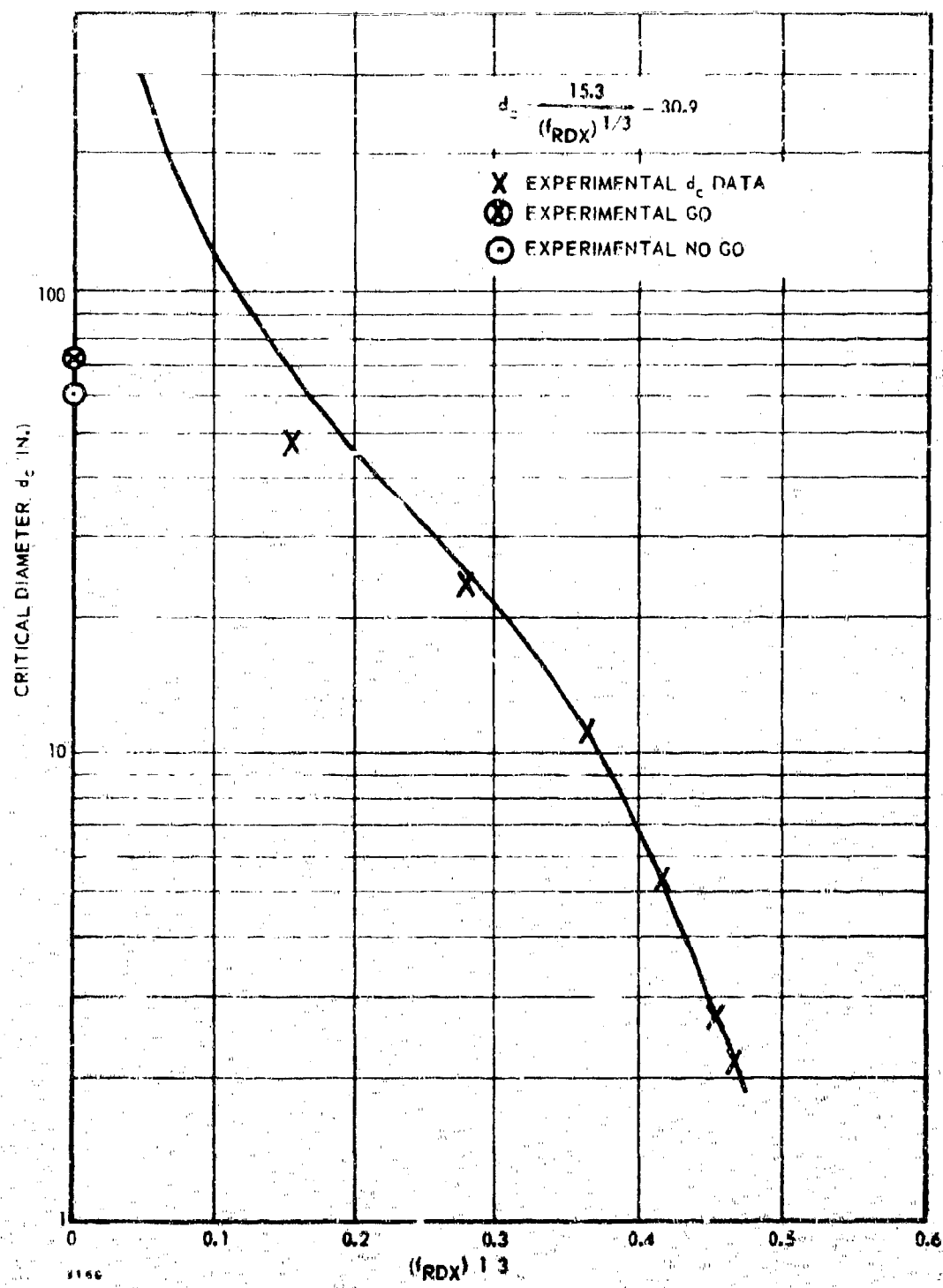


Figure I-1. Correlation of Critical Diameter Data -- One Type of Initiation Site.

Case of Two Types of Initiating Sites, with Negligible Initiation Times

In this case, the one-dimensional lattice model expression for  $\tau_r$  (i.e., Equation I-31) and Equation I-40 yields

$$d_c = \frac{K'_1}{(f_{RDX})^{1/3} + c'} - K'_2 (f_{RDX})^{1/3} \quad (I-42)$$

The best fit to the experimental data of Table I-I is found for the parameter values  $K'_1 = 24.55$ ,  $K'_2 = -50.54$ , and  $c' = 0.19$ . The correlation of Equation I-42 with the data is shown in Figure I-2. Also shown is Irwin's correlation curve (References I-7 and I-9) which corresponds to the use of Equation I-29 for  $\tau_r$ , i.e.,

$$d_c = \frac{K_1}{(f_{RDX} + c)^{1/3}} - K_2 \quad (I-43)$$

It is readily seen that both expressions for  $d_c$  correlate the data very well for  $f_{RDX} \geq 0.00375$ ; however, the results of the two experimental tests at zero percent RDX appear to favor Equation I-43.

If one assumes that the experimental  $d_c$  data reflect the existence of inherent RDX-like initiating sites, then one might conclude that Irwin's expression for  $\tau_r$  (Equation I-29) may be more appropriate than the corresponding one-dimensional lattice model expression (i.e., Equation I-33). It is noted here that the primary discrepancy between the two expressions lies in the difference between the factors  $(f_{RDX} + c)^{-1/3}$  and  $(f_{RDX}^{1/3} + c')^{-1}$ , which in essence describe the average distance between centers of all initiating sites. The factor  $(f_{RDX}^{1/3} + c')^{-1}$  results from averaging the one-dimensional concentration expressed as number of sites/unit length, i.e.,

$$\bar{s} \propto (\sum f_i^{1/3})^{-1} \quad (I-44)$$

or

$$\bar{s} \propto (f_{RDX}^{1/3} + c')^{-1} \quad (I-45)$$

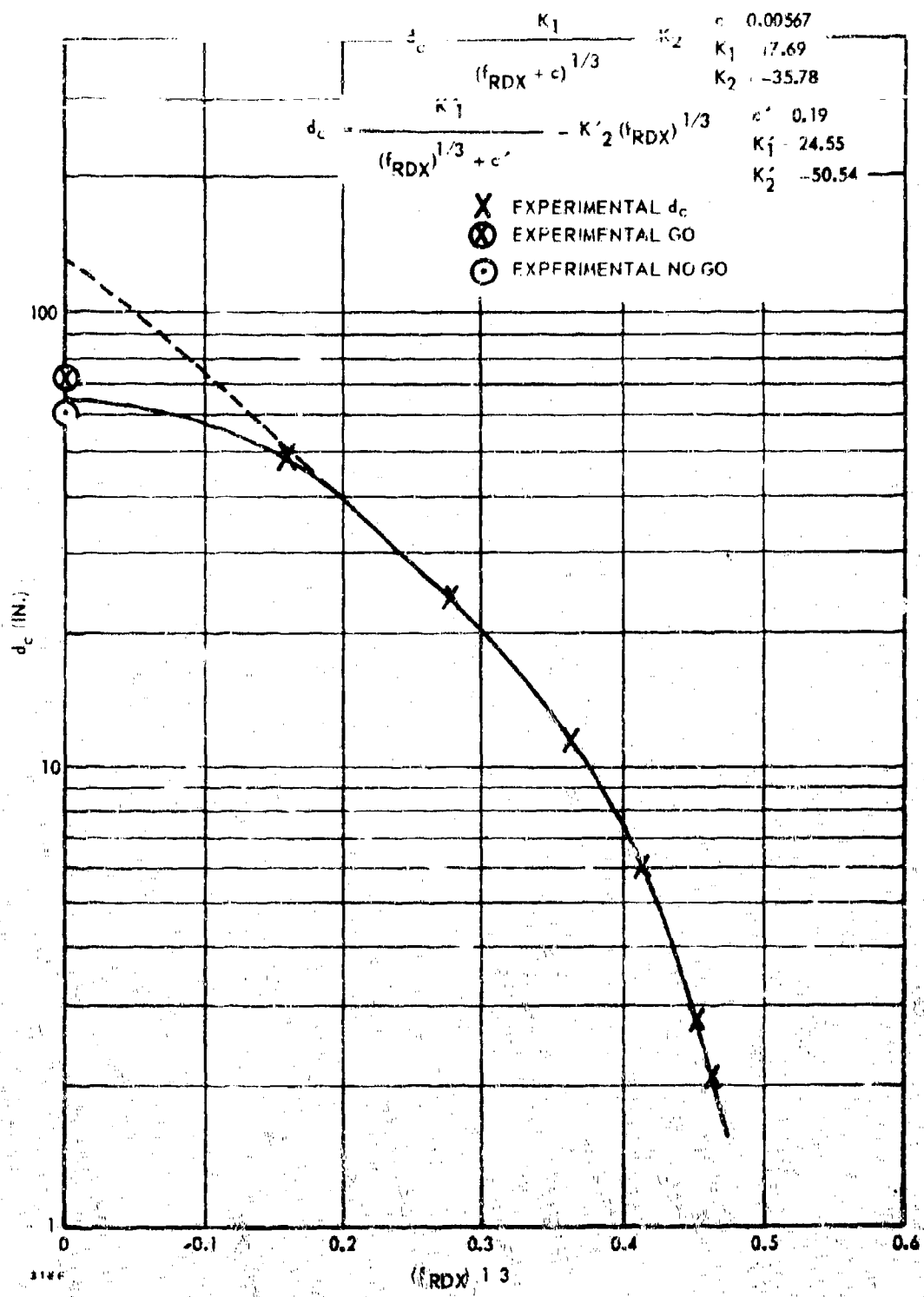


Figure 1-2. Correlation With Two Types of Initiation Sites.

However, in three dimensions the average distance between sites should be based upon an average of the number of sites/unit volume. This would probably lead to

$$\bar{S} \propto (\sum f_i)^{-1/3} \quad (I-46)$$

or

$$\bar{S} \propto (f_{RDX} + c)^{-1/3} \quad (I-47)$$

Thus if the assumption of inherent RDX-like initiating sites is valid then the better fit of Irwin's expression to the experimental  $d_c$  data would suggest that a three-dimensional lattice model may be required for a more quantitative description of detonation in heterogeneous explosives. Unfortunately, the three-dimensional approach to the problem brings up additional mathematical problems, and is not available at this time.

Alternatively, the fact that the apparent  $d_c$  for  $f_{RDX} = 0$  falls below the value that is predicted by Equation I-42, while the  $d_c$  data for  $f_{RDX} \geq 0.02$  follow Equation I-41 quite well (i.e., single type of initiating site) might indicate that the inherent initiating sites are active only for very small values of  $f_{RDX}$  (i.e., only for large  $\tau_r$ ). This brings us to the possible situation described earlier in this section which is applied to the  $d_c$  data in the following paragraphs.

#### Case Where the Number of Types of Initiating Sites Varies with $\tau_r$

If one assumes that the  $d_c$  data of Table I-I reflect the existence of inherent initiating sites which become active only when  $\tau_r$  exceeds a certain value, then in accordance with the approximation treatment shown earlier in this section the data of Table I-I should be fit by three different but related expressions for  $d_c$  based upon three different regions of  $\tau_r$ .

##### a. Primary region:

$$(\tau_0)_{RDX} \ll \tau_r < (\tau_0)_X$$

In the primary region, only the RDX particles are active initiating sites, hence Equations I-35 and I-40 obviously yield an expression for  $d_c$  which is the same as Equation I-41. From Figure I-1, it can be estimated that the primary region extends over the range  $2.12 \leq d_c \leq 23.5$  in.

It is now useful to express the constants of Equation I-41 in terms of more fundamental quantities. Noting that

$$N_i = \left[ \frac{6\rho}{\pi \rho_i L_i^3} \right]^{1/3} (f_i)^{1/3} = a_i f_i^{1/3} \quad (I-48)$$

where  $\rho$  is the propellant density. Equation I-41 can now be expressed as

$$(d_c)_p = \frac{K}{2B_c} \left[ \frac{1}{a_i f_i^{1/3}} - L_1 \right] \quad (I-49)$$

where the subscript 1 now represents RDX. Comparison of the constants of Equation I-49 with those of Equation I-41 yields

$$K_1 = K/2a_1 B_c = 15.3 \quad (I-50)$$

$$K_2 = KL_1/2B_c = -30.9 \quad (I-51)$$

These parameters can now be used in the expression for  $d_c$  in the transition region.

b. Transition region:

$$(\tau_o)_{RDX} \ll \tau_r \approx (\tau_o)_x$$

Combining Equations I-37, I-40, and I-48, yields

$$(d_c)_t = \frac{K}{2a_1 B_c f_1^{1/3}} - \frac{KL_1}{2B_c} - \frac{KN_{20} L_2}{2B_c a_1 f_1^{1/3}} \quad (I-52)$$

where the subscript 2 refers to the inherent initiation sites.

Utilizing Equations I-50 and I-51, the expression for  $d_c$  can be expressed as

$$(d_c)_t = \frac{K_1}{f_1^{1/3}} - K_2 - \frac{K_1 K_3}{f_1^{1/3}} \quad (I-53)$$

where  $K_3 = N_{20} L_2$  (dimensionless).

Assuming that  $d_c = 48$  in. represents the transition region yields a value of  $K_3 = 9.1994$ . The resulting empirical relationship for  $d_c$  in the transition region is

$$(d_c)_{\text{transition}} = \frac{12.25}{(f_{\text{RDX}})^{1/3}} - 30.9 \text{ (inches)} \quad (\text{I-54})$$

A comparison of Equation I-54 with the experimental data is shown in Figure I-3; also shown is a replot of Equation I-41 for the primary region.

c. Secondary region:

$$(\tau_o)_{\text{RDX}} < (\tau_o)_x < \tau_r$$

Application of Equations I-39, I-40, and I-48 to the secondary yields

$$(d_c)_s = a_1 L_2 \left[ \frac{K_1}{K_3} - K_1 \right] \quad (\text{I-55})$$

Since  $(d_c)_s$  depends only upon the inherent ignition sites, it must be a constant of the propellant system. This is shown in Figure I-3 where  $(d_c)_s$  is estimated from the experimental data to be 70 in. The actual variation of  $d_c$  with  $f_{\text{RDX}}$  is then assumed to follow the dashed curve of Figure I-3, which is merely an estimated interpolation of how the three different detonation regions transform into each other.

Obviously, the approach taken above in correlating the experimental data does not offer the predictive characteristics of the cases previously described; however, it does serve to offer a possible alternate route to explaining the detonative behavior of RDX adulterated propellants.

It is interesting to note that the above type of data correlation is not completely devoid of predictive capabilities, since choosing the constant  $(d_c)_s$  at 70 in. sets the value of  $a_1 L_2$  at 1.265 in. From Reference I-7,  $a_1$  can be estimated as  $2.07 \times 10^3$  which yields a value of  $L_2 = 6.11 \times 10^{-4}$  in. Thus, assuming that the above analysis is correct, the inherent hot-spot diameter is  $\sim 16 \mu$ . Also, since  $N_{2o} = K_3/L_2$ , the resulting distance between hot-spot centers (i.e.,  $1/N_{2o}$ ) becomes  $\sim 80 \mu$ .

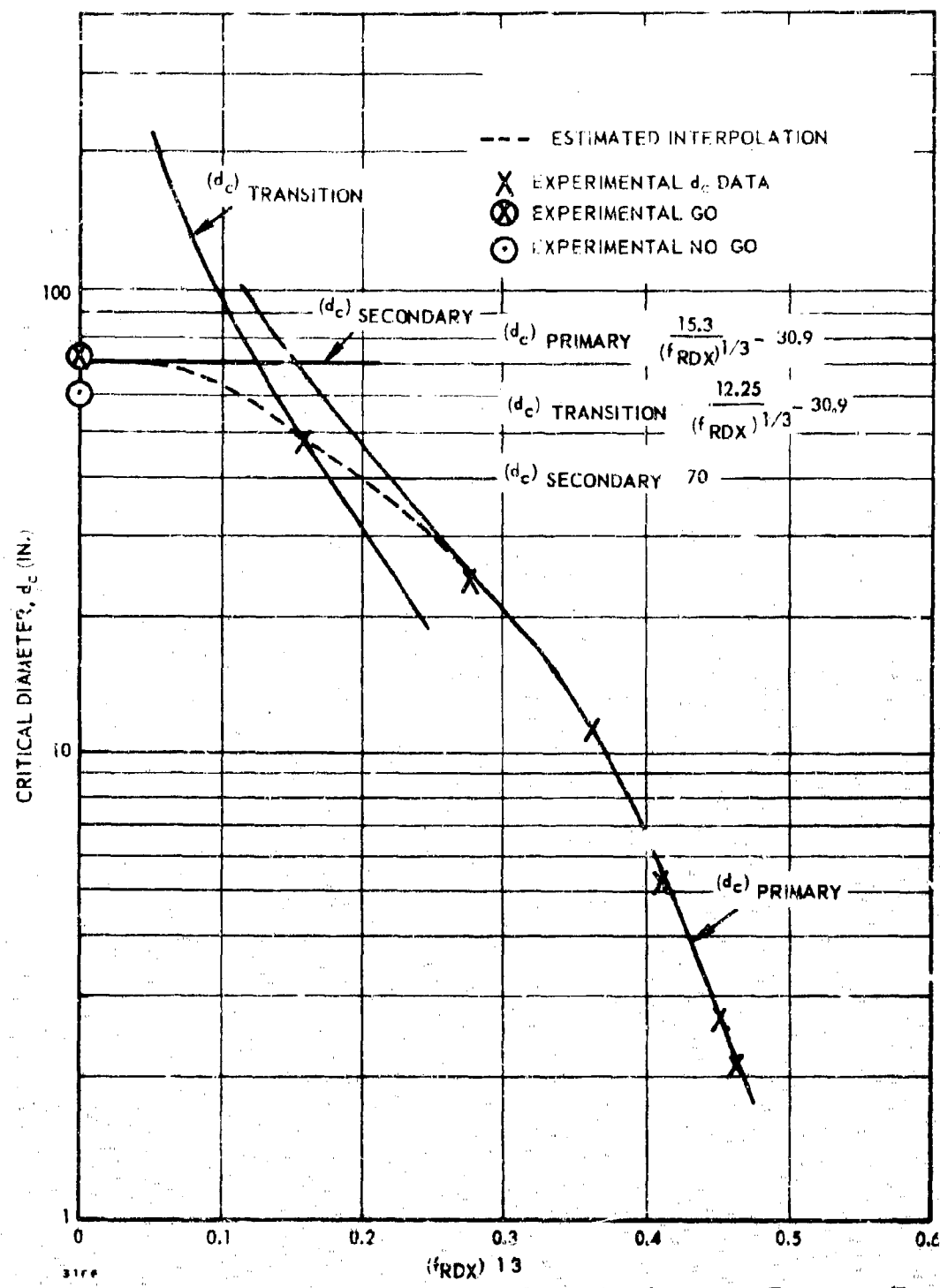


Figure I-3. Correlation of Critical Diameter Data -- Types of Sites Varying with  $\tau_r$ .

The grain burning distance between hot-spots then becomes  $S \sim L_2$   $\approx 64 \mu$ . It is interesting to note that in the propellant under consideration, the AP content was composed of a bimodal distribution in which  $\sim 60\mu$  radius particles (peak size) comprised  $\sim 50\%$  of the propellant mass, and  $\sim 6\mu$  radius particles comprised  $\sim 18\%$  of the propellant mass. It is suggestive from the values found for  $L_2$  and  $N_{20}$  that the inherent initiation sites might be the small AP particles, which, along with aluminum, reside in the interstices between the large AP particles. The distance between the interstices of the large AP particles can be shown from simple geometric considerations to be  $\sim 70\mu$ . It should be emphasized that at present this suggestion must be considered highly speculative.

#### SUMMARY AND CONCLUSIONS

A lattice model of detonation of heterogeneous explosives has been described based upon the concepts of both hot-spot ignition theory and grain burning theory.

Through a one-dimensional treatment of the model it has been possible to derive the classical Eyring grain burning equation and to define the assumptions underlying the use of the Eyring equation, viz: (1) that hot-spots have no finite dimension or ignition time; and (2) the average concentration of hot-spots is equal to the concentration of explosive granules (i.e., one hot-spot per granule). In addition, it has been possible to relax these assumptions and to extend the one-dimensional treatment to other explosive situations, i.e., (1) where the time to ignition of grain burning is nonnegligible compared to the overall detonation time, and (2) where there may be several types of ignition sites, each type having a discretely different ignition time. Such explosive situations appear to have application to the detonability of RDX adulterated solid composite propellant.

For the case of RDX adulterated propellant in which the RDX particles are the sole source of hot-spots, the one-dimensional treatment of the lattice model leads to a detonation reaction time expression which is identical to an expression previously proposed by Dr. Irwin at Aerojet. The proposed expression for  $T_r$  has already been shown to be very satisfactory in describing the variation of critical diameter of composite propellant containing varying amounts of RDX in the range of 2 to 10%.

For the case of propellant containing less than 2% RDX the critical diameter data suggest that RDX cannot be a sole source of hot-spots. Extending the lattice model to this case results in expressions for  $r_r$  which differ somewhat from an expression which was proposed and successfully applied by Dr. Irwin for the same explosive situation. However, the differences are relatively slight and may simply involve the use of a one-dimensional approach rather than a three-dimensional approach in describing the average concentration of hot-spots.

In any case, it would appear that the present lattice model of detonation serves as a fundamental basis for the description of propellant detonation which had been initially developed at Aerojet.

It would be of future interest to undertake a more rigorous mathematical treatment of the lattice model in which certain constraints (viz., those involved in the approximation of Equation I-19) were removed from the one-dimensional treatment. Also, the treatment of the lattice model should be extended to three dimensions.

Finally the lattice model should be extended to include the effects of lateral quenching waves (i.e., rarefaction waves) on the overall detonation reaction time. Such an extension could lead to a description of nonideal detonation phenomenon such as fading detonation and charge diameter effects.

#### REFERENCES FOR APPENDIX I

- I-1. Eyring, H., R. E. Powell, G. H. Duffy, and R. B. Parlin, Chem. Rev., 45, 69 (1949).
- I-2. Andersen, W. H., and R. F. Chaiken, ARS Journal, 29, 49 (1959).
- I-3. Andersen, W. H., and R. F. Chaiken, ARS Journal, 31, 1379 (1961).
- I-4. Chaiken, R. F., Eighth Symposium (International) on Combustion, Williams and Wilkins, Baltimore (1962), p. 759.
- I-5. Campbell, A. W., W. C. Davis, and J. B. Ramsey, Phys. Fluids, 4, 498 (1961).
- I-6. Bowden, F. B., and A. D. Yoffe, Initiation and Growth of Explosion in Liquids and Solids, University Press, Cambridge (1952).
- I-7. Aerojet-General Corporation, Technical Documentary Report AFRPL-TR-65-211 on Contract AF04(611)9945 (November 1965).
- I-8. Price, D., "Contrasting Patterns in the Behavior of High Explosives," Eleventh Symposium (International) on Combustion, Berkeley, California, 14-20 August 1966.
- I-9. Aerojet-General Corporation, Technical Documentary Reports AFRPL-TR-66-25 (June 1966) and AFRPL-TR-66-26 (September 1966) on Contract AF04(611)10919.

## APPENDIX II

## COMMENTS ON THE RUBY CODE

R. F. Chaiken, Technical Consultant  
 Aerojet-General Corporation,  
 Downey, California

## INTRODUCTION

The RUBY Code (Reference II-1) is a FORTRAN computer program designed to calculate the ideal detonation properties of high explosives utilizing Chapman-Jouguet (C-J) theory. The program is based on the assumption that the gaseous products obey the Becker-Kistiakowsky-Wilson (BKW) equation of state (References II-2 and II-3), which can be written as

$$\frac{PV}{nRT} = 1 - X \exp (\beta X) \quad (II-1)$$

where

$$X = \frac{x \sum_i k_i n_i}{V (T + \theta)^{\alpha} \sum_i n_i}$$

Here,  $\alpha$ ,  $\beta$ ,  $x$ ,  $\theta$ ,  $k_i$  are constants, and  $n_i$  is the mole fraction of the  $i$ th gaseous product.

In RUBY, this P, V, T relation is used to express the one-dimension detonation conservation equations and C-J hypothesis (i.e.,  $D = C_J + W_J$ ) in terms of P, V, T variables, and also to describe the fugacity of the gaseous reaction products as a function of pressure and temperature. In addition, RUBY employs an equation of state of the form

$$P = \sum_{j=0}^4 a_j \left(\frac{P}{P_{s,o}}\right)^j + \sum_{k=0}^1 b_k \left(\frac{P}{P_{s,o}}\right)^k T + \sum_{m=0}^2 c_m \left(\frac{P}{P_{s,o}}\right)^{-m} T^2 \quad (II-2)$$

to handle the possible existence of one or two solid detonation products.

The C-J state is assumed to be at thermodynamic equilibrium (minimum free energy) and is calculated by a method of steepest descent, which is described by White, et al (Reference II-4).

The main use of RUBY to date has been in the calculation of ideal detonation properties of CHNO explosives (References II-2, II-3, II-5, II-6)<sup>4</sup>. The general approach has been to determine the BKW constants (i.e.,  $\alpha$ ,  $\beta$ ,  $x$ ,  $\theta$ ,  $k_1$ ) which allow the best fit to the experimental  $D(P_0)$  and  $P_J(f_0)$  data for one or two specific explosives (e.g., RDX, PETN), and after selecting these constants, to apply RUBY to other explosives.

Generally, the RUBY calculated  $D(P_0)$  and  $P_J(P_0)$  for CHNO explosives are in fair agreement with experiment; however, there is apparently no single set of BKW parameters which yields good agreement with all 20 of the explosives considered. For example, Table 4 in Reference II-5 illustrates that detonation velocities and pressures may be in error by as much as 10% and 15%, respectively. Also, while there is a lack of reliable experimental data on detonation temperatures, it would appear that RUBY values of  $T_J$  may be up to 40% too low.

The purpose of this report is to examine the results of the RUBY program and to determine its usefulness in calculating the ideal detonation properties of conventional solid propellants containing ammonium perchlorate, aluminum, and oxygen-deficient rubber-type binders. Of particular interest is the use of RUBY to determine the effect of incomplete chemical reaction on the ideal detonation properties ( $D$ ,  $P_J$ ,  $T_J$ ). Toward this end, RUBY calculations have been carried out for ammonium perchlorate (AP), alone and in combination with typical propellant ingredients, and for RDX/aluminum mixtures. Computer-input techniques were developed to allow various amounts of aluminum to remain unreacted. These calculations brought out certain apparent internal inconsistencies which suggest that RUBY should not be used to predict the detonation properties of aluminized explosives.

## RUBY CALCULATIONS

### Ammonium Perchlorate

The detonation properties of ammonium perchlorate (AP) have been calculated by RUBY over the range of loading densities  $0.8 \leq P_0 \leq 1.5$  gm/cc. Various sets of BKW constants have been employed to

<sup>4</sup> References II-2 and II-3 do not refer to RUBY calculations per se, but to similar calculations using the BKW equation of state.

attempt to match the reported experimental data (References II-7 and II-8), as well as to ascertain the sensitivity of the computed detonation properties to changes in the BKW constants.

The results of these calculations are shown in Figures II-1 through II-3 where ideal detonation velocity ( $D$ ), Chapman-Jouguet pressure ( $P_J$ ), and Chapman-Jouguet temperature ( $T_J$ ) are plotted against  $P_0$ . The notes for Figures II-1 through II-3 describe the conditions for obtaining curves A through F. These results show that by suitable adjustment of the BKW constants ( $\alpha$ ,  $\beta$ ,  $\chi$ ,  $\theta$ , and in particular,  $k_i$  for the principal gas products, e.g., HCl) almost any linear  $D(P_0)$  curve can be obtained.

However, the constants that have been derived for best fit with CHNO explosives (e.g., curve A and B), although yielding reasonable agreement with the experimental  $P_J$  value at  $P_0 = 1.0$  gm/cc, do not yield good agreement with the experimental  $D$  value. Even curve E, which is presumably the result of SRI's attempt (Reference II-8) to optimize the BKW constants for AP, falls short of being in good agreement with experimental detonation velocities.

With regard to the RUBY-calculated Chapman-Jouguet temperatures, it is readily seen that an increase in  $P_0$  results in a decrease in  $T_J$ . This  $T_J(P_0)$  relationship appears to be common to all RUBY calculations, including those for CHNO explosives (References II-2, II-3, II-5, and II-6). This undoubtedly arises from the fact that the BKW equation of state considers only a repulsive potential between the detonation products. On the other hand, curve F, which corresponds to calculations with Cook's covolume equation of state (Reference II-9), shows  $T_J(P_0)$  to be an increasing function of loading density. Cook's covolume depends only on volume and hence does not consider the potential energy arising from intermolecular interaction. Unfortunately, the present lack of reliable experimental  $T_J$  data precludes a clear-cut answer as to whether  $T_J$  should be an increasing or decreasing function of  $P_0$ .

In the case of high-density CHNO explosives, it has been argued (Reference II-2) that since the C-J density ( $P_J$ ) is generally greater than the explosive crystal density, the distances between atomic and molecular species in the C-J plane are so small so that the interactions between the species are primarily repulsive (hence, the BKW-type of equation of state).

In this case, even though the total change in specific internal energy of detonation increases with  $P_0$ , the net result could be to increase the potential energy of the C-J system at the expense of the kinetic energy.

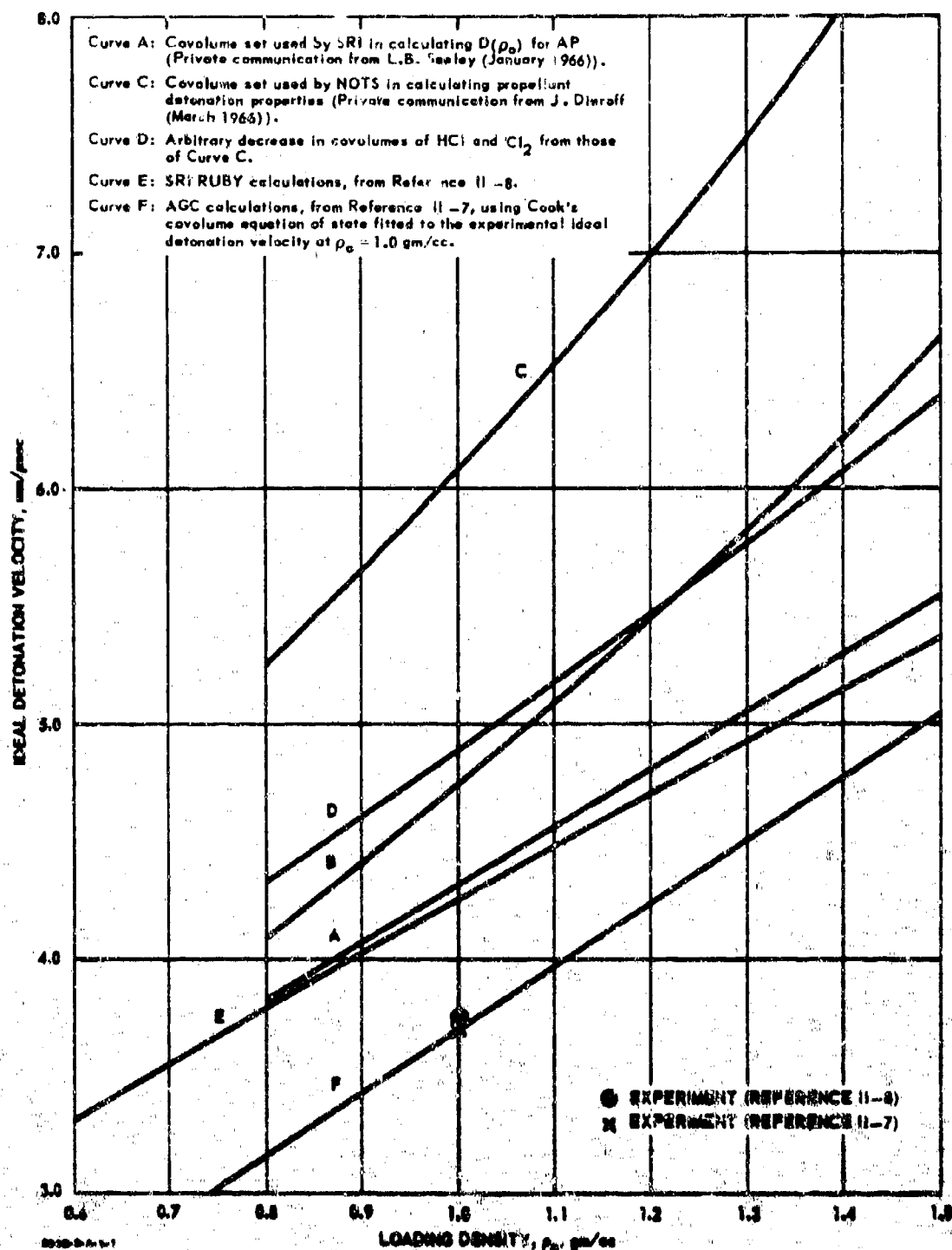


Figure III-1. Calculated Detonation Velocities of Ammonium Perchlorate.

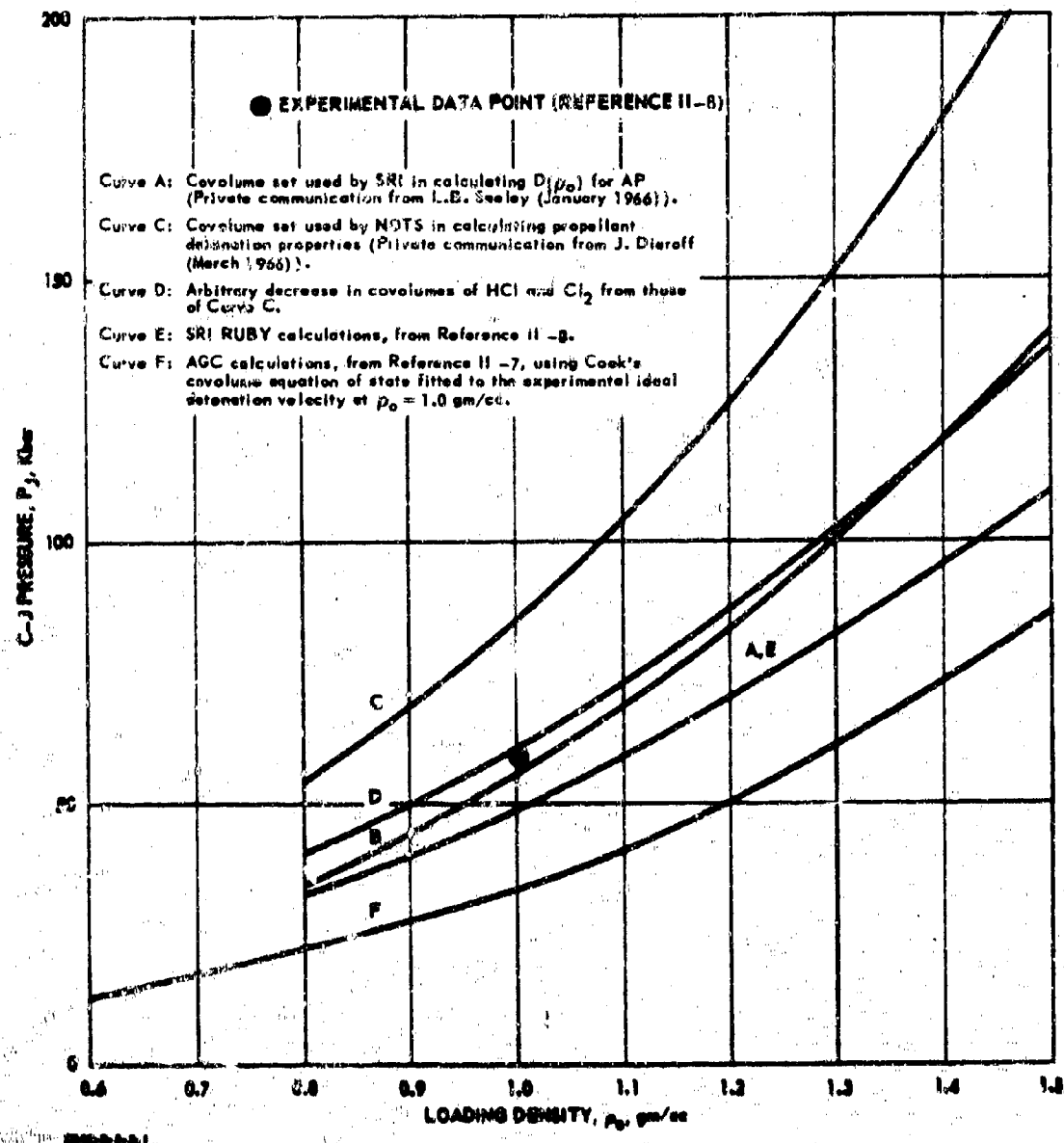


Figure II-2. Calculated Detonation Pressures of Ammonium Perchlorate.

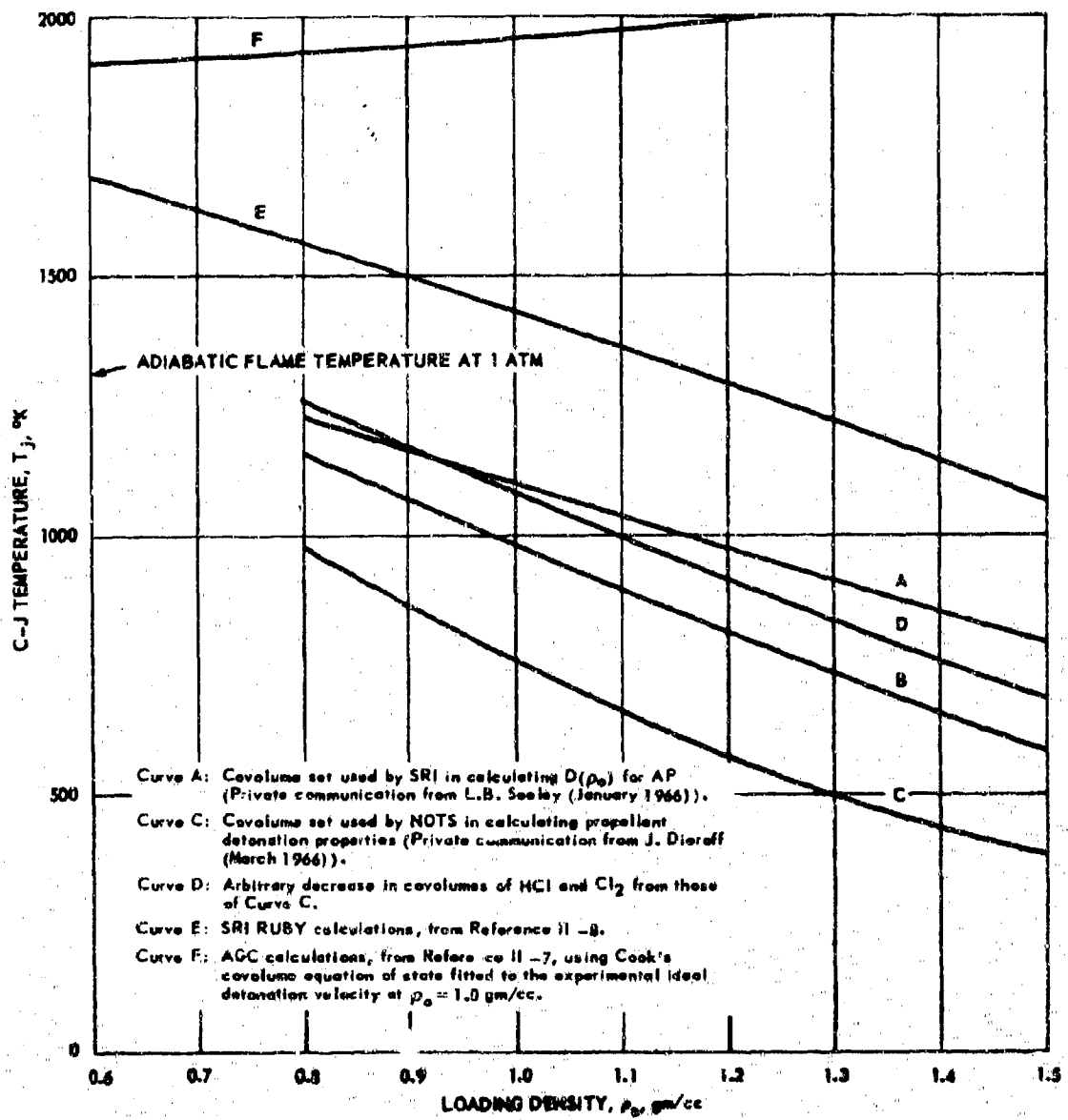


Figure II-3. Calculated Detonation Temperatures of Ammonium Perchlorate.

## NOTES FOR FIGURES II-1 THROUGH II-3

### Curves A and B

RUBY calculations to determine the effect of a change in BKW constants, using the same thermodynamics data:

Curve A:  $a = 0.5; \beta = 0.09; \chi = 11.85; \theta = 400$

Curve B:  $a = 0.5; \beta = 0.16; \chi = 10.91; \theta = 400$

The BKW set for curve A corresponds to the set used by Cowan and Fickett (Reference II-2) for curve-fitting 65/35 RDX/TNT  $D(P_o)$  data. The BKW set for curve B corresponds to the set used by Mader (Reference II-3) for curve fitting RDX  $D(P_o)$  data.

### Curves A, C, and D

RUBY calculations to determine the effect of a change in covolume constants using the same BKW constants.  
Values of  $k_i$  for curves A, C, and D:

	Curve C	Curve D	Curve A
H <sub>2</sub> O	360	360	250
H <sub>2</sub>	180	180	180
N <sub>2</sub>	380	380	380
NH <sub>3</sub>	476	476	476
N <sub>2</sub> O	670	670	670
NO	336	386	386
O <sub>2</sub>	350	350	350
NO <sub>2</sub>	670	670	600
HCl	1588	794	643
Cl <sub>2</sub>	1157	578	532

However, for ammonium perchlorate at the loading densities considered here,  $P_J$  is less than the crystal density (1.95 gm/cc). It is difficult therefore to understand why the above argument should still be valid under these conditions. It is believed that the RUBY-calculated decrease in  $T_J$  as  $P_0$  increases is unrealistic for AP. On the other hand, it should be stated that the  $T_J$  values obtained for AP by use of the Cook-covolume equation of state, which are 600 to 700°K higher than the AP adiabatic flame temperature (1 atm), might also be unreasonable. However, the increasing  $T_J(P_0)$  function that is obtained by such a covolume equation of state is, at least to this writer, intuitively plausible.

#### Solid Composite Propellant

RUBY calculations have been carried out for a solid composite propellant composition containing AP, aluminum, and PBAN binder (polybutadiene-acrylonitrile copolymer). The effect of replacing part of the AP with RDX on the detonation properties has been calculated, as well as the effect of nonreaction of the aluminum. This latter effect corresponds to a current theory that the aluminum oxidation reaction proceeds too slowly to occur within the detonation reaction zone (Reference II-10).

Prevention of aluminum oxidation in the RUBY calculation is readily accomplished by replacing all or part of the aluminum in the explosive composition by the fictitious metal AlX. The AlX has all the thermodynamic properties of Al, but no oxidation products (e.g.,  $AlX_2O_3$ ,  $AlX_2O_2$ ,  $AlXCl_3$ ).

The results of the RUBY calculations with the BKW constants and thermal data corresponding to curve C in Figures II-1 through II-3 are shown in Table II-I. The data for propellant A (normal case, w/ 100% Al reaction) are comparable to data obtained for high explosives with similar heats of explosion. A comparison of propellant C (9.2% RDX adulterated propellant) with propellant A shows that the detonation parameters ( $E$ ,  $P_J$ ,  $T_J$ ,  $E_J - E_0$ ) all increase when the more energetic RDX ( $\Delta Q \approx 1300$  Kcal/gm) replaces AP ( $\Delta Q \approx 300$  Kcal/gm). These results are to be expected. The effect of replacing aluminum (reactive) with AlX (unreactive) is that  $P_J$ ,  $T_J$ ,  $E_J - E_0$  decrease as might be expected, but there is a 4% increase in the detonation velocity. This is evident by comparing propellant A with propellant B.

**Table II-I. Detonation Properties of AP Propellant as Calculated by RUBY.**

Propellant A: AP/Al/PBAA = 0.69/0.15/0.16 (100% Al reaction)

Propellant B: AP/Al/PBAA = 0.69/0.15/0.16 (5% Al reaction)\*

Propellant C: AP/Al/PBAA/RDX = 0.598/0.15/0.16/0.092 (100% Al reaction)

DETONATION PROPERTIES	Propellant		
	$P_0 = 1.73$	$P_0 = 1.73$	$P_0 = 1.715$
D, mm/ $\mu$ sec	7.14	7.40	7.25
P <sub>j</sub> , Kbar	226	206	232
T <sub>J</sub> , °K	3198	1091	3217
V <sub>J</sub> , cc/mole of gas	12.39	14.41	12.61
$P_0/P_j$	0.743	0.783	0.743
E <sub>J</sub> - E <sub>0</sub> , cal/gm HE	401	308	415
BKW parameter	5.71	11.38	5.86
C-J composition, 10 <sup>-3</sup> moles/gm HE			
Total Gases (*,**)	28.85	27.74	28.67
CH <sub>4</sub>	5.19	5.69	5.76
CO	4.25	nil	4.70
CO <sub>2</sub>	1.65	5.40	1.88
Cl	5.73	nil	4.91
ClO	nil	5.04	nil
H <sub>2</sub>	0.19	nil	0.15
H <sub>2</sub> O	8.44	8.29	6.95
N <sub>2</sub>	2.61	2.83	3.44
NH <sub>3</sub>	0.65	0.20	0.69
AlCl	0.14	nil	0.18
AlCl <sub>3</sub>	nil	0.28	nil
Total Solids (*,**)	2.71	5.28	2.69
Al(l)	--	5.28	--
Al <sub>2</sub> O <sub>3</sub>	2.71	nil	2.69
C (graphite)	nil	--	nil

(\*) Unreacted Al goes to Al(l) as a detonation product.

(\*\*) Only products 10<sup>-3</sup> moles/gm HE are included.

(\*\*) A dash indicates the product was not programmed.

Examination of the gaseous detonation products shows that the total amount of gas is the same in the two cases, and that except for an increase in  $\text{CO}_2$  with an accompanying decrease in  $\text{CO}$ , there is little change in gas products when aluminum does not react. From the heats of formation of  $\text{Al}_2\text{O}_3$ ,  $\text{CO}$ , and  $\text{CO}_2$ , the net enthalpy loss from the explosive system with  $\text{AlX}$  would be  $\sim 350$  cal/gm of explosive. It would be difficult to reconcile an increase in detonation velocity with this energy loss. Undoubtedly, the calculated increase in  $D$  stems from the value of the BKW parameter ( $X$  in Equation II-1), which does change appreciably. Since  $k_i$  for  $\text{CO}_2$  is 670 vs 390 for  $\text{CO}$  in these calculations, it is seen that the value of  $k \gamma_{ikin}$  in Equation II-1 will increase when  $\text{CO}$  is converted to  $\text{CO}_2$ . (When aluminum does not react, there is more oxygen available in the explosive for reaction with carbon. Thus, a greater portion of the carbon is converted to  $\text{CO}_2$  than would be the case if aluminum reacted to  $\text{Al}_2\text{O}_3$ .)

When this increase is combined with a decrease in C-J temperature (which results from the  $\text{AlX}$  not reacting), the BKW parameter becomes excessively large. It is apparent that the accompanying increase in  $V_J$  (which results from a lower  $P_J$ ) is far from enough to prevent the excessively high value of the BKW parameter. The apparent result is an increase in the detonation velocity, which conflicts with the general expectation that  $D$  is an increasing function of  $E_J - E_0$  for any given explosive. Similar results are obtained for RUBY calculations with RDX/Al mixtures.

#### Aluminized Explosives

Table II-II shows the results of RUBY calculations for RDX in combination with Al,  $\text{AlX}$ , and  $\text{Al}_2\text{O}_3$  (80/20 mixtures) at the same loading density ( $\rho_0 = 1.94$  gm/cc). For additional comparison, the results of a similar calculation for RDX at a slightly different density ( $\rho_0 = 1.8$  gm/cc) are also shown. These calculations were carried out with the same set of thermodynamic data and BKW constants. (The set of input data are those obtained from UCRL except for the addition of input data required for the aluminum-containing products:  $\text{AlO}(r)$ ,  $\text{Al}_2\text{O}(g)$ ,  $\text{Al}_2\text{O}_2(g)$ ,  $\text{Al}(l)$ , and  $\text{Al}_2\text{O}_3(c)$ . Presumably, the UCRL data set has been optimized for RDX.)

While a direct comparison of the calculated properties of explosive A (pure RDX) with explosive B (20% aluminum) is not possible because the loading densities are not the same in both cases, the addition of reacting aluminum greatly increases the detonation temperature ( $\Delta T_J \approx 2000^\circ\text{K}$ ). This is further borne out by the drastic drop in  $T_J$  when the aluminum is prevented from reacting (explosive C).

Table II-II. Detonation Properties of RDX Explosives  
as Calculated by RUBY.

Explosive A: RDX

Explosive B: RDX/Al = 80/20 (100% Al reaction)

Explosive C: RDX/AlX = 80/20 (0% Al reaction)\*

Explosive D: RDX/Al<sub>2</sub>O<sub>3</sub> = 80/20

DETONATION PROPERTIES	Explosives			
	A	B	C	D
P <sub>0</sub> , gm/cc	1.80	1.94	1.94	1.94
D, mm/ $\mu$ sec	8.03	8.56	9.11	8.28
P <sub>J</sub> , Kbar	287	359	332	297
T <sub>J</sub> , °K	1824	3882	2262	2428
V <sub>J</sub> , cc/mole of gas	11.71	12.28	11.58	12.05
P <sub>0</sub> /P <sub>J</sub>	0.752	0.747	0.794	0.776
E <sub>J</sub> - E <sub>0</sub> , cal/gm HE	472	464	421	410
BKW parameter	9.23	6.86	8.71	8.09
C-J composition, 10 <sup>-3</sup> moles/gm HE				
Total Gases (*,**)	33.80	25.32	27.06	27.21
CH <sub>4</sub>	0.38	3.33	0.04	0.36
CO	0.10	4.47	0.17	0.57
CO <sub>2</sub>	7.09	2.48	5.45	5.73
H <sub>2</sub>	nil	0.04	nil	nil
H <sub>2</sub> O	12.72	2.85	10.53	9.57
N <sub>2</sub>	13.50	10.38	10.74	10.64
NH <sub>3</sub>	0.01	0.83	0.13	0.34
NO	nil	0.05	nil	nil
Al <sub>2</sub> O	--	0.91	--	nil
Total Solids (*,**)	5.92	3.31	12.55	6.09
Al(1)	--	--	7.41	--
Al <sub>2</sub> O <sub>3</sub>	--	2.80	--	1.96
C (graphite)	5.92	0.51	5.14	4.13

(\*) Unreacted Al goes to Al(1) as a detonation product.

(\*\*) Only products > 10<sup>-3</sup> moles/gm HE are included.

(\*\*) A dash indicates the product was not programmed.

As in the aluminized propellant case, it is readily seen that non-reaction of aluminum (explosive C) causes an increase in D, while  $P_J$ ,  $T_J$ , and  $E_J$  all decrease. Again, the relatively large increase in the BKW parameter with AlX suggests that the conversion of CO to  $CO_2$  may be responsible for this effect.

However, it appears that replacing aluminum by  $Al_2O_3$  (explosive D) does not show a similar effect, even though in this case  $Al_2O_3$  can be considered as an inert ingredient in the same manner as AlX. A comparison of the detonation products of explosives C and D does not appear to offer any significant clues to the different effects of the two inert additives on RDX. However, the effective heats of formation used for the two RDX mixtures were somewhat different: 76.8 cal/gm for explosive C vs 686 cal/gm for explosive D. It is suggested that under these circumstances a direct comparison of the two cases may not be too meaningful without experimental data for both RDX/Al and RDX/ $Al_2O_3$  mixtures.

There are abundant experimental data on aluminized high explosives which show that aluminum lowers the detonation velocity of the pure explosives (Reference II-9). It has been proposed that the aluminum either behaves as an inert diluent or that it reacts to  $Al_2O(g)$  with an overall endothermic effect. The results of the RUBY code appear to be inconsistent with the experimental results as well as with either of these explanations.

#### DISCUSSION AND CONCLUSIONS

From the RUBY calculations carried out for CHNO explosives and for AP propellants, it is apparent that with sufficient adjustment of the many available parameters in the BKW equation of state, suitable  $D(P_0)$  and  $P(P_0)$  data can be calculated for any given explosive. However, it is likewise apparent that the extension of the RUBY calculations to other explosives with selected BKW constants may lead to highly questionable results, particularly when those explosives involve new gaseous products. Although this point had already been made clear by Cowan and Fickett in their original paper (Reference II-2), it has apparently not been emphasized by subsequent investigators who have reported RUBY calculations.

In spite of any agreement that one can obtain between RUBY-calculated and experimental detonation velocities and pressures, there are certain internal inconsistencies which throw doubt on the usefulness of the BKW equation of state in calculating detonation properties. These internal inconsistencies involve (1) a calculated C-J temperature which consistently decreases as  $P_0$  increases for any given explosive, and (2) the increase in detonation velocity

when the aluminum in aluminized explosives does not react to contribute energy to the C-J state. Both of these effects appear to be related to the BKW equation of state which considers the energy of molecular interaction to be solely repulsive. Under the detonation conditions which are normally calculated by RUBY, it is felt that such an equation of state will overemphasize the role of pressure and underemphasize the role of temperature in determining the product distribution and the detonation properties.

In this connection, it is interesting to examine the actual value of the apparent molar covolume (i.e., the excluded volume) that results from the RUBY calculations presented for propellants in Table II-I. By comparing Equation II-1 with a covolume equation of state, i.e.,

$$P(V-b) = nRT \quad (\text{II-3})$$

it can be readily shown that the apparent molar covolume  $b/n$  can be expressed as

$$b/n = \frac{RT}{P} \times \exp \beta X \quad (\text{II-4})$$

For propellants A, B, and C the values of  $b/n$  are 11.0, 13.5, and 11.3 cc/mole, respectively. These values represent approximately 90 to 95% of the calculated molar gas volume ( $V_J$ ), thus indicating an extremely compact C-J state. It seems unlikely that such a state can exist and still be composed of recognizably independent molecular species.

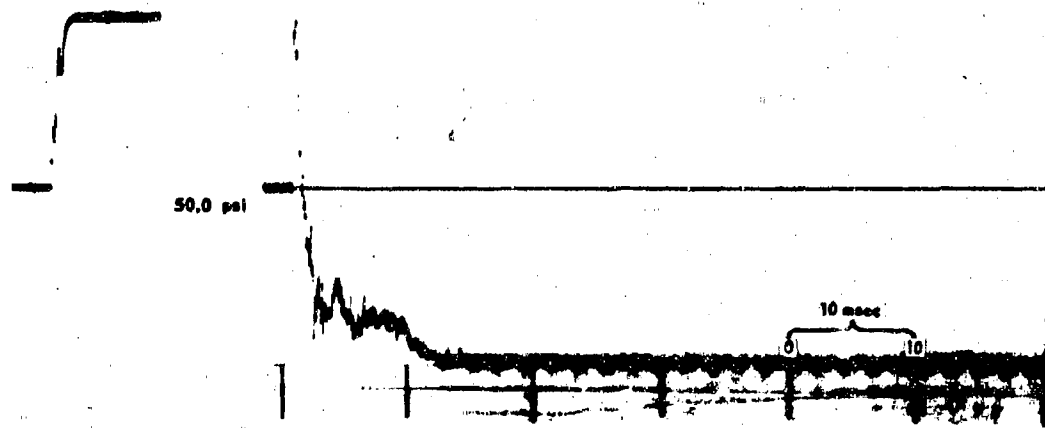
Although the RUBY calculations that have been carried out to date do not exclude the possibility that the noted inconsistencies can be resolved by a complete change in the BKW constants, they do indicate the unsatisfactory nature of the present code with regard to calculating detonation properties of propellants and aluminized explosives. In view of this, and the arguments presented against an equation of state that implies solely repulsive forces, it is suggested that further work with the RUBY code not be continued.

Pending development of a more satisfactory computer program (presumably incorporating a more realistic product equation of state), it is proposed that the Parlin-Andersen-Miller procedure (References II-11 and II-12) used in the SOPHY I program continue to be used to estimate the ideal detonation velocity.

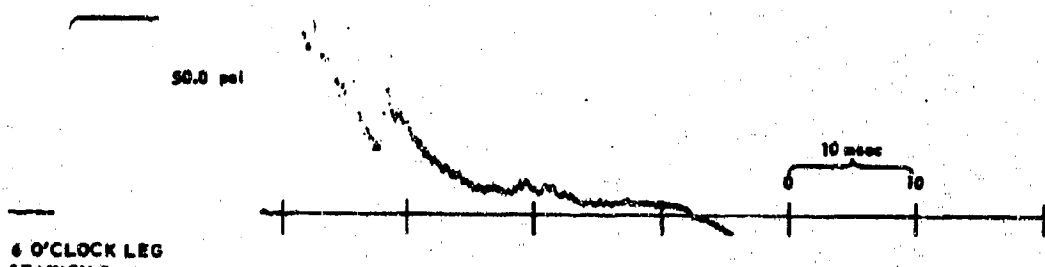
## REFERENCES FOR APPENDIX II

- II-1. Levine, H. B., and R. E. Sharples, Operator's Manual for RUBY, UCRL 6815 (20 March 1962).
- II-2. Cowan, R. D., and W. Fickett, J. Chem. Phys. 24, 932 (1956).
- II-3. Mader, C. L., Los Alamos Report LA-2900 (Feb. 1963).
- II-4. White, W. B., S. M. Johnson, and G. B. Dantzig, J. Chem. Phys., 28, 751 (1958).
- II-5. Price, D., and H. Hurwitz, USNOL, NOLTR 63-216 (1 Nov. 1963).
- II-6. Hurwitz, H., USNOL, NOLTR 63-205 (31 March 1965).
- II-7. Andersen, W. H., and R. E. Pesante, Eighth Symposium (International) on Combustion, Williams & Wilkins Co., Baltimore, Md., p. 705 (1962).
- II-8. Evans, M. W., B. O. Reese, and L. B. Seely, The Fourth Symposium on Detonation, Vol. II of Preprints, p. C-78 (12-15 Oct. 1965).
- II-9. Cook, M. A., The Science of High Explosives, Reinhold, New York, ch. 4 (1958).
- II-10. Salzman, P. K., O. R. Irwin, W. H. Andersen, AIAA Journal, 3, 2230 (1965).
- II-11. Andersen, W. H., and R. E. Parlin, Technical Report No. 28, 31 Oct. 1953, Institute for the Study of Rate Processes, University of Utah.
- II-12. Miller, R. O., Progress in Astronautics and Rocketry; Detonation and Two-Phase Flow, Vol. 6, Academic Press, New York, pp 623-652 (1960).

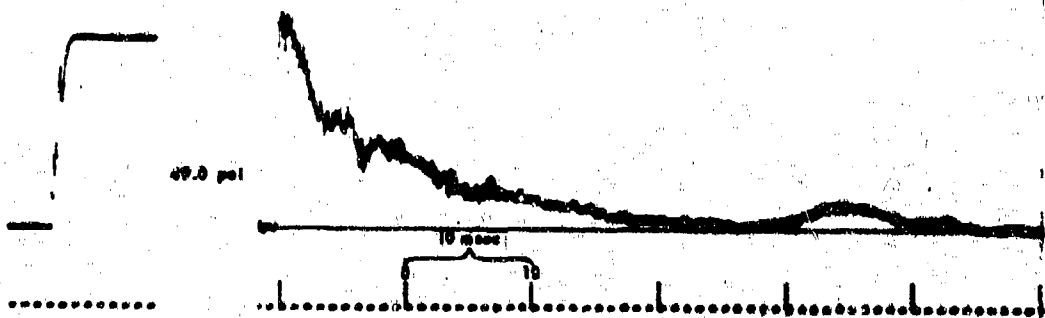
APPENDIX III  
TEST CD-96 DATA



10 O'CLOCK LEG  
STATION 5 - CALIBRATION STEP AND PRESSURE-TIME SHOCK PROFILE



6 O'CLOCK LEG  
STATION 5 - CALIBRATION STEP AND PRESSURE-TIME SHOCK PROFILE



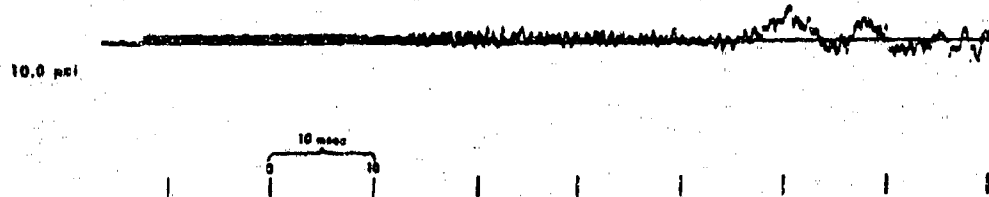
2 O'CLOCK LEG  
STATION 5 - CALIBRATION STEP AND PRESSURE-TIME SHOCK PROFILE

Figure III-1. Side-On Overpressure, Station 5, Test CD-96.

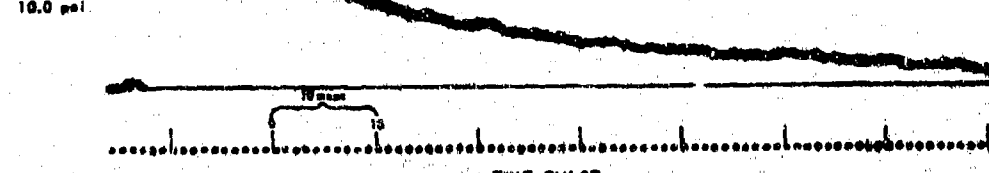
Note

NO GAUGE WAS INSTALLED

10 O'CLOCK LEG  
STATION 6 CALIBRATION STEP AND PRESSURE-TIME SHOCK PROFILE

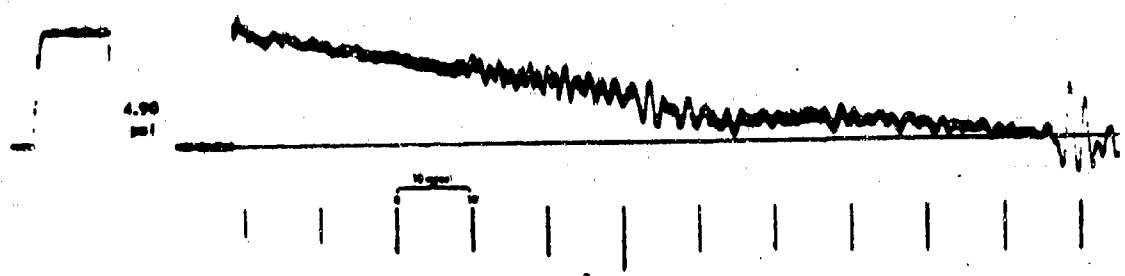


6 O'CLOCK LEG  
STATION 6 CALIBRATION STEP AND PRESSURE-TIME SHOCK PROFILE

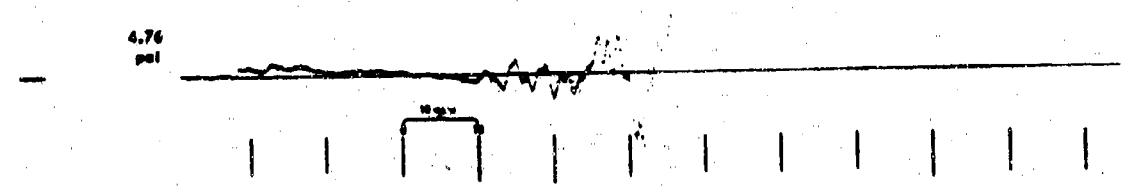


2 O'CLOCK LEG  
STATION 6 CALIBRATION STEP AND PRESSURE-TIME SHOCK PROFILE

Figure III-2. Side-On Overpressure, Station 6, Test CD-96.



12 O'CLOCK LEG  
STATION 7 CALIBRATION STEP AND PRESSURE-TIME SHOCK PROFILE

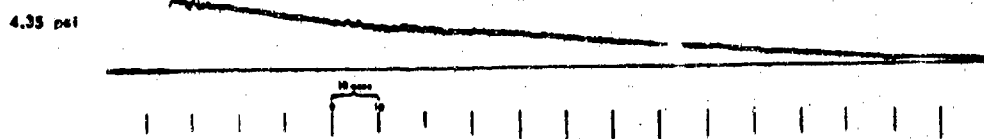


6 O'CLOCK LEG  
STATION 7 CALIBRATION STEP AND PRESSURE-TIME SHOCK PROFILE

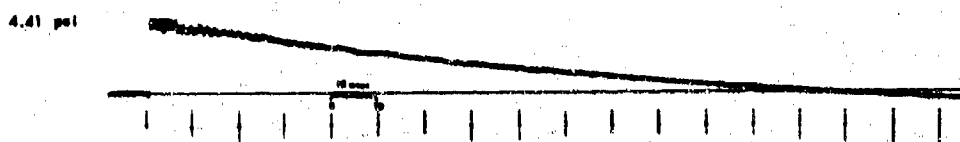


2 O'CLOCK LEG  
STATION 7 CALIBRATION STEP AND PRESSURE-TIME SHOCK PROFILE

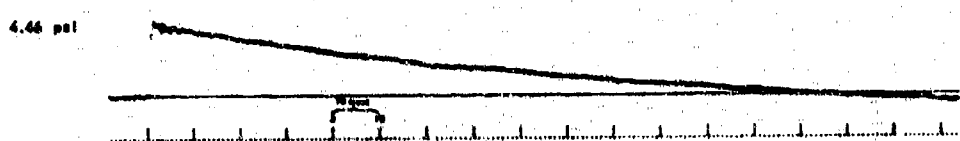
Figure III-3. Side-On Overpressure, Station 7, Test CD-96.



10 O'CLOCK LEG  
STATION 8 CALIBRATION STEP AND PRESSURE-TIME SHOCK PROFILE



6 O'CLOCK LEG  
STATION 8 CALIBRATION STEP AND PRESSURE-TIME SHOCK PROFILE



2 O'CLOCK LEG  
STATION 8 CALIBRATION STEP AND PRESSURE-TIME SHOCK PROFILE

TIME PULSE

Figure III-4. Side-On Overpressure, Station 8, Test CD-96.

1.76 psi

10 O'CLOCK LEG  
STATION 9 CALIBRATION STEP AND PRESSURE-TIME SHOCK PROFILE

1.76 psi

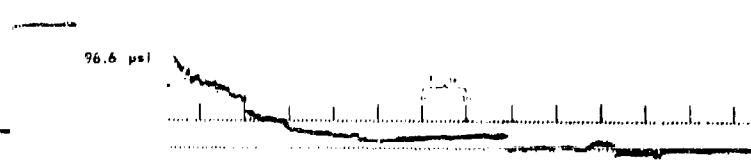
6 O'CLOCK LEG  
STATION 9 CALIBRATION STEP AND PRESSURE-TIME SHOCK PROFILE

1.76 psi

2 O'CLOCK LEG  
STATION 9 CALIBRATION STEP AND PRESSURE-TIME SHOCK PROFILE

TIME PULSE

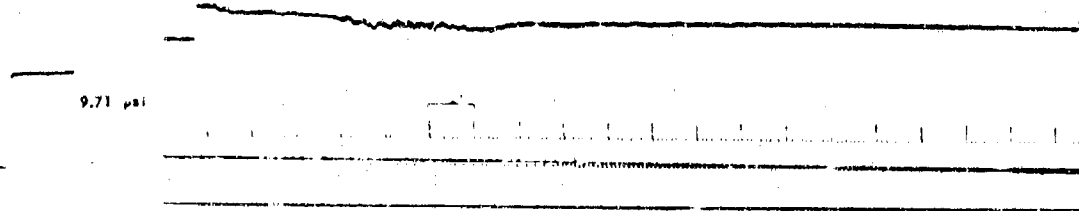
Figure III-5. Side-On Overpressure, Station 9, Test CD-96.



5 O'CLOCK LEG  
STATION 5 CALIBRATION STEP AND PRESSURE-TIME SHOCK PROFILE



6 O'CLOCK LEG  
STATION 6 CALIBRATION STEP AND PRESSURE-TIME SHOCK PROFILE



6 O'CLOCK LEG  
STATION 8 CALIBRATION STEP AND PRESSURE-TIME SHOCK PROFILE

TIME PULSE

Figure III-6. Face-On Overpressure, Test CD-96.

## APPENDIX IV

### JETTING PHENOMENON

Streak-camera observations of previous critical geometry tests of hollow cylindrical samples showed that an abrupt cessation of an apparently steady detonation occurs at some point along the length of the sample (Reference IV-1). The location of this point appeared to be determined by the web thickness of the grain when the results obtained for only one propellant formulation were analyzed. Since it is observed that a high-velocity jet is produced in the core of an end-initiated hollow cylinder, the responsibility for the anomalous behavior of hollow cylindrical samples may be ascribed to effects caused by the jetting phenomenon. Therefore, a series of tests was designed to investigate the manner in which jetting affects the detonation reaction of hollow cylinders. These tests include studies of the effect of core diameter (ID), sample length, and web thickness on the behavior of hollow cylinders.

#### EFFECT OF CORE DIAMETER

Hollow samples cast from AAB-3189 propellant having web thickness equal to 1.4 in. were prepared in several sizes in which only the ID varied. Core diameters of 0.06, 0.12, 0.25, 0.50, 0.80, 1.5, and 3.0 in. were chosen. All sample lengths were four times the OD. The samples were instrumented with four sets of ionization probes in circuit with four rasteroscillographs to obtain distance-time data on the reactive shock wave and the jet. Three sets of probes placed in the propellant gather the data at radial positions 1/4-, 1/2-, and 3/4-web in. from the outside of the samples. The fourth set of probes monitors the travel of the jet along the charge axis. Figure IV-1 shows the test setup.

A 1-in. thick Plexiglas plate is placed between the Composition B booster and the propellant acceptor. The Plexiglas attenuates the velocity of the shock wave entering the acceptor. This allows better resolution of the initial behavior of the reactive shock wave in the propellant by preventing its being masked by the normal attenuation of a highly overboostered initiating wave in the acceptor, which would occur if the booster charge were placed directly on the propellant sample. The Plexiglas barrier also prevents the booster shock wave from forming a jet in the hollow acceptor before the propellant detonation reaction produces its jet. The 1-in. thick attenuator does not reduce the shock pressure below the minimum level required to initiate detonation in these samples.

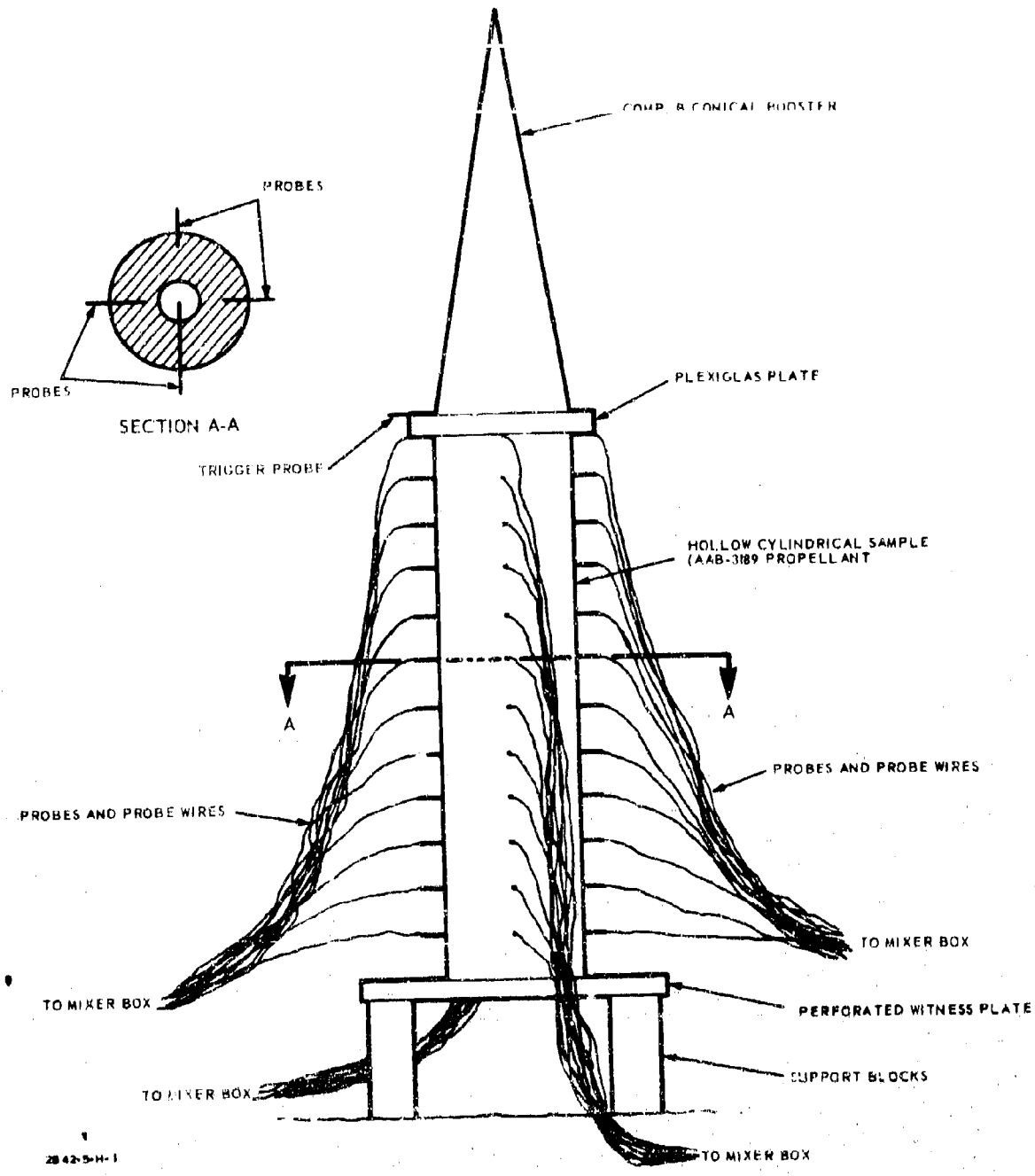


Figure IV-1. Jetting Phenomena Test Setup.

The specific purpose of these tests was to determine the influence of the ID on the location of the point along the charge length where detonation ceases. It is of interest to learn whether a minimum core diameter exists below which the jet has no effect on the propellant behavior, and whether a maximum core diameter of reasonable proportions exists above which the jet has no effect on the propellant behavior.

The distance-vs-time data were reduced for plotting the detonation velocity vs distance along the sample at each radial distance into the sample.

Figure IV-2 is a plot of the data obtained at the 1/4-web depth. Only straight lines were used to connect the individual data points, because to have fit the data to smooth curves would have made it more difficult to isolate the data of any one sample size from the others. From these data it is evident that regardless of the size of the ID the detonation began to fade after 7 in. of travel in the samples.

The results obtained at 1/2-web depth are shown in Figure IV-3 and are consistent with the preceding. The data indicate that from the middle of the web toward the outer surface of the hollow samples the detonation wave front is perpendicular to the charge axis until rapid fading begins.

The data obtained at the 3/4-web depth (Figure IV-4) are much more erratic than those from locations more removed from the inner surface. They also show no correlation with core size, but do indicate that fading begins somewhat sooner at this position, i.e., at 5 to 6 in.

The jet-velocity data (Figure IV-5) show some oscillatory behavior. More important, there is evidently a correlation between the size of the perforation and the velocity of the jet. It was observed that higher jet velocities occurred at smaller core sizes. This would be expected because the Mach interaction that produces the jet would be greatest when the core size is minimum.

Some experimental difficulty in probe placement with the 0.06-in.-ID samples prevented jet-velocity data from being obtained beyond the 4-in. distance. Probes further down the charge indicated low velocities more typical of the values obtained within the web, and these were assumed to have been owing to failure to reach the small core with the probes.

From these tests, it is concluded that the abortion of sustained detonation velocity is independent of core size over the 50-fold range from 0.06-in. to 3.0-in. ID.

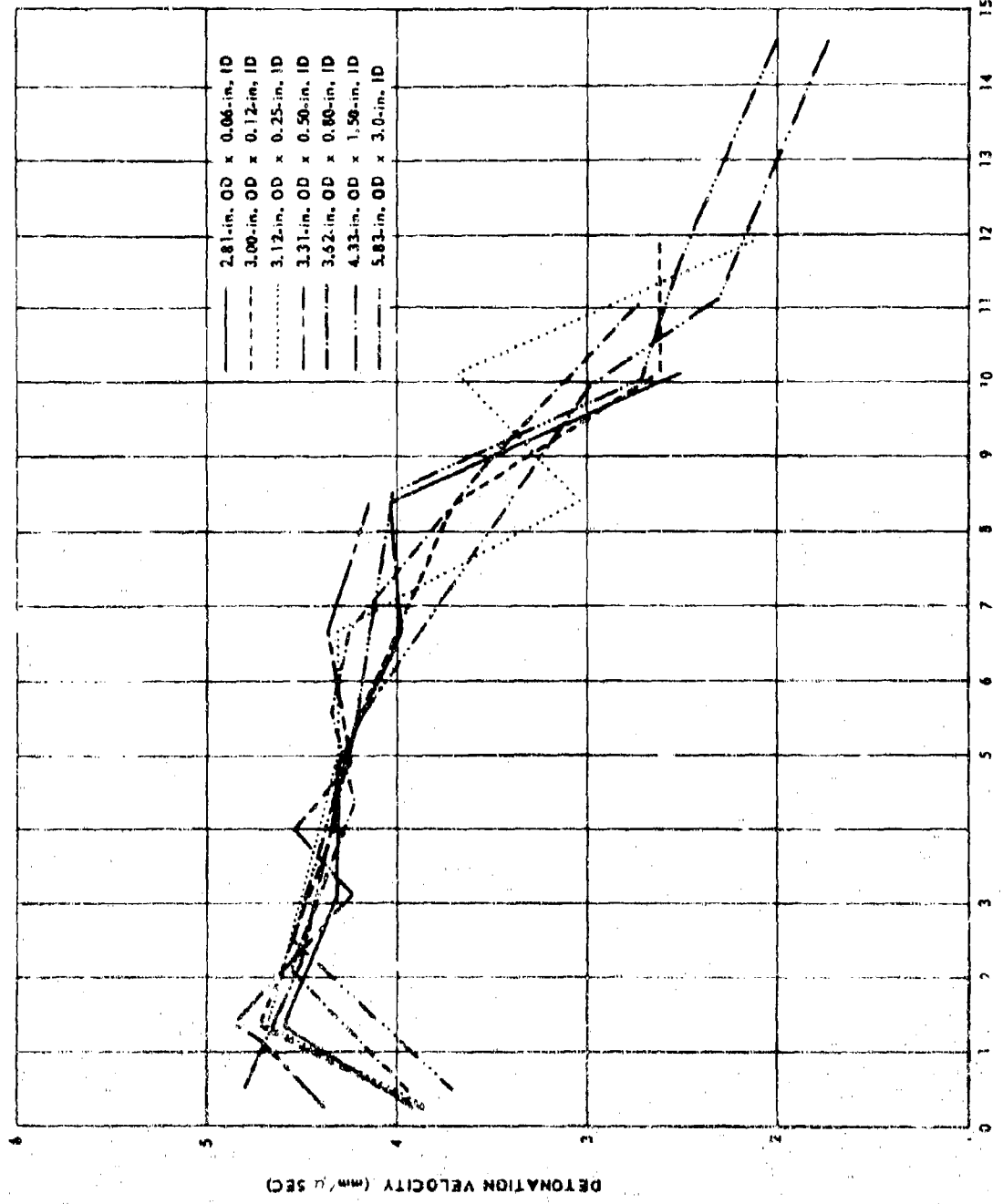


Figure IV-2. Detonation Velocity Behavior in 1.4-in. Web, Hollow Cylinders of AAB-3189. (Obtained at Points 1/4 Web into the Samples)

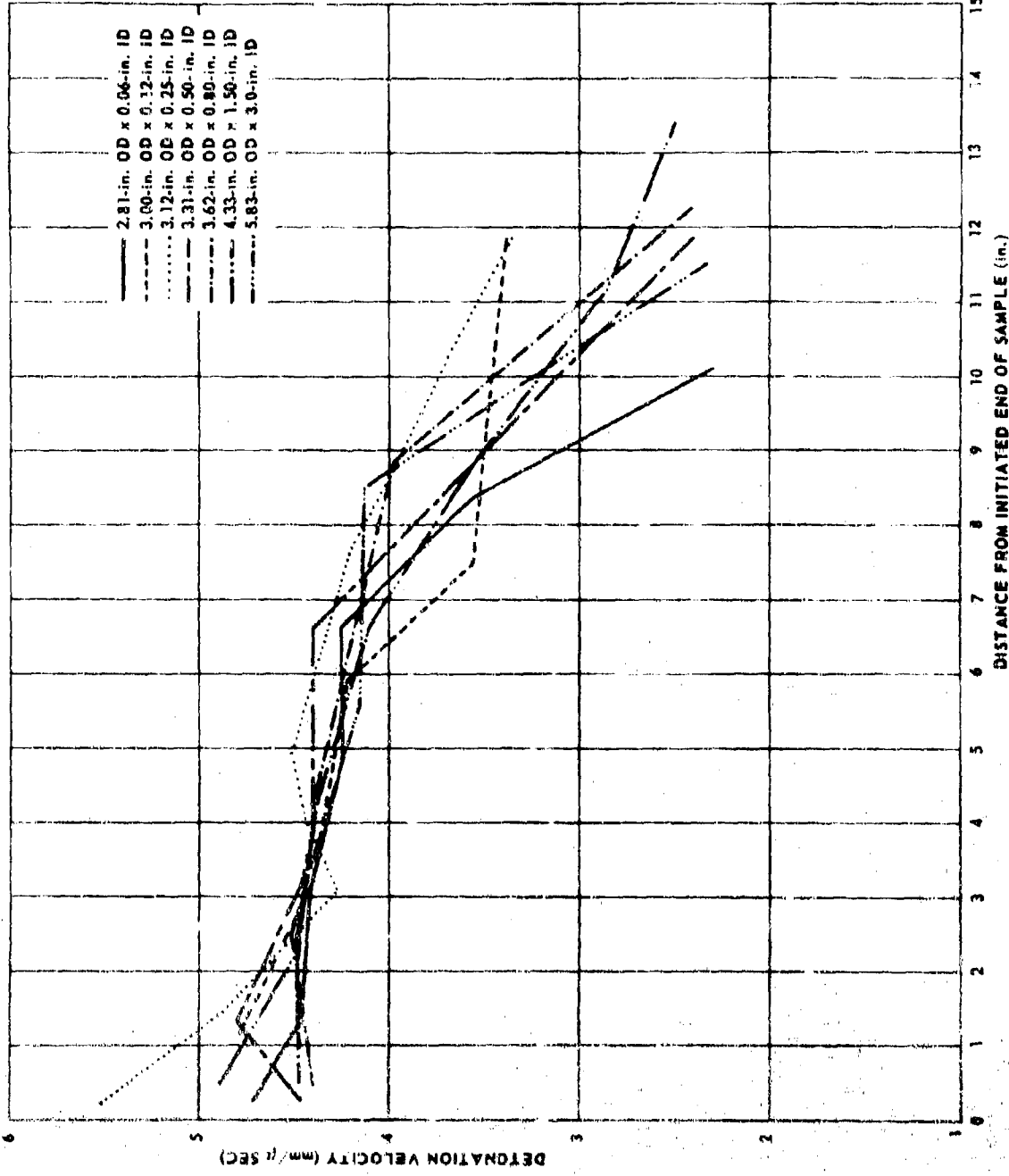


Figure IV-3 Detonation Velocity Behavior in 1 1/4-in. Web, Hollow Cylinders  
of AAB-3189. (Obtained at Points 1/2-Web into the Samples)

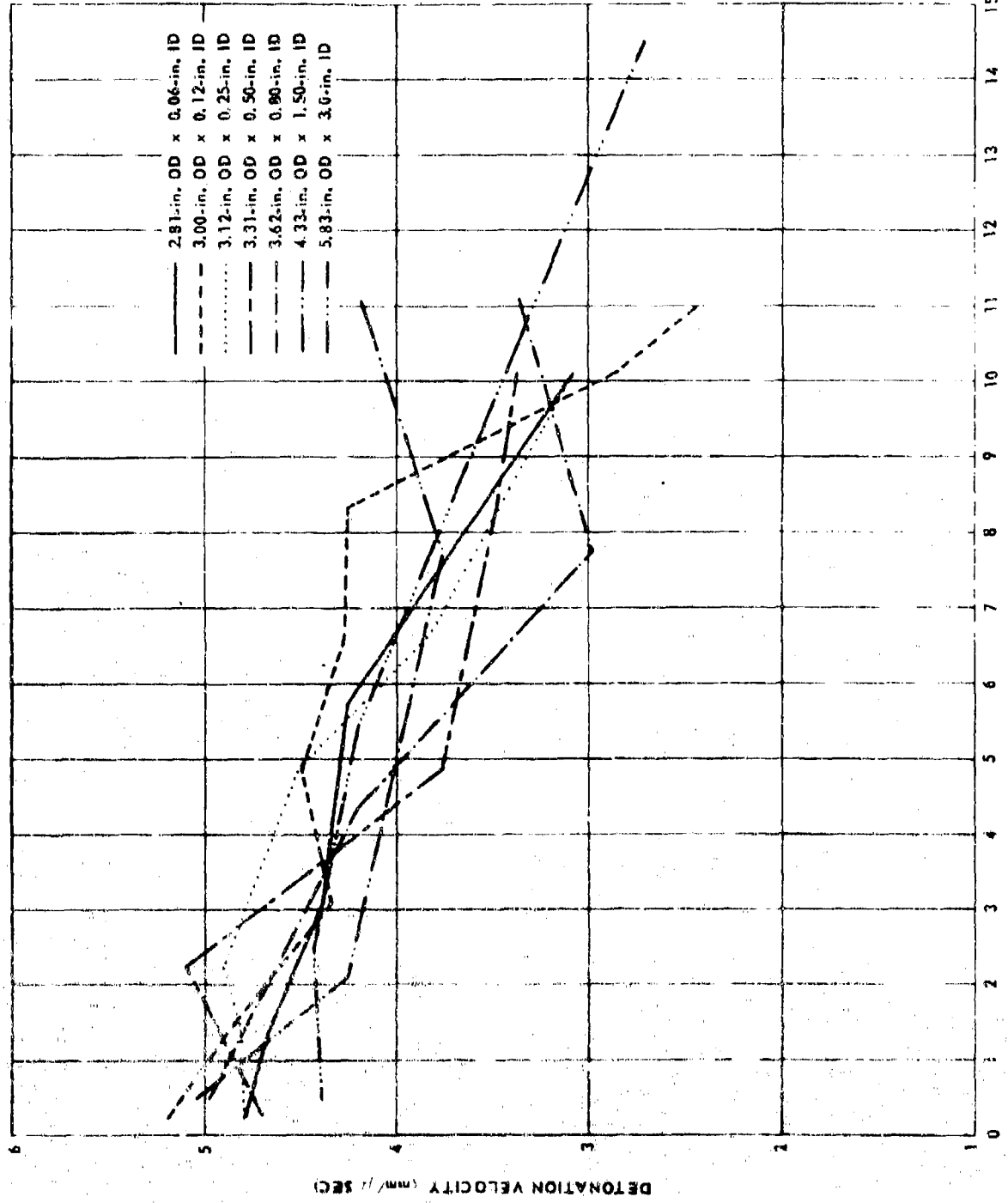


Figure IV-4. Detonation Velocity Behavior in 1.4-in. Web, Hollow Cylinders  
of AAB-3139. (Obtained at Points 3/4-Web into the Samples.)

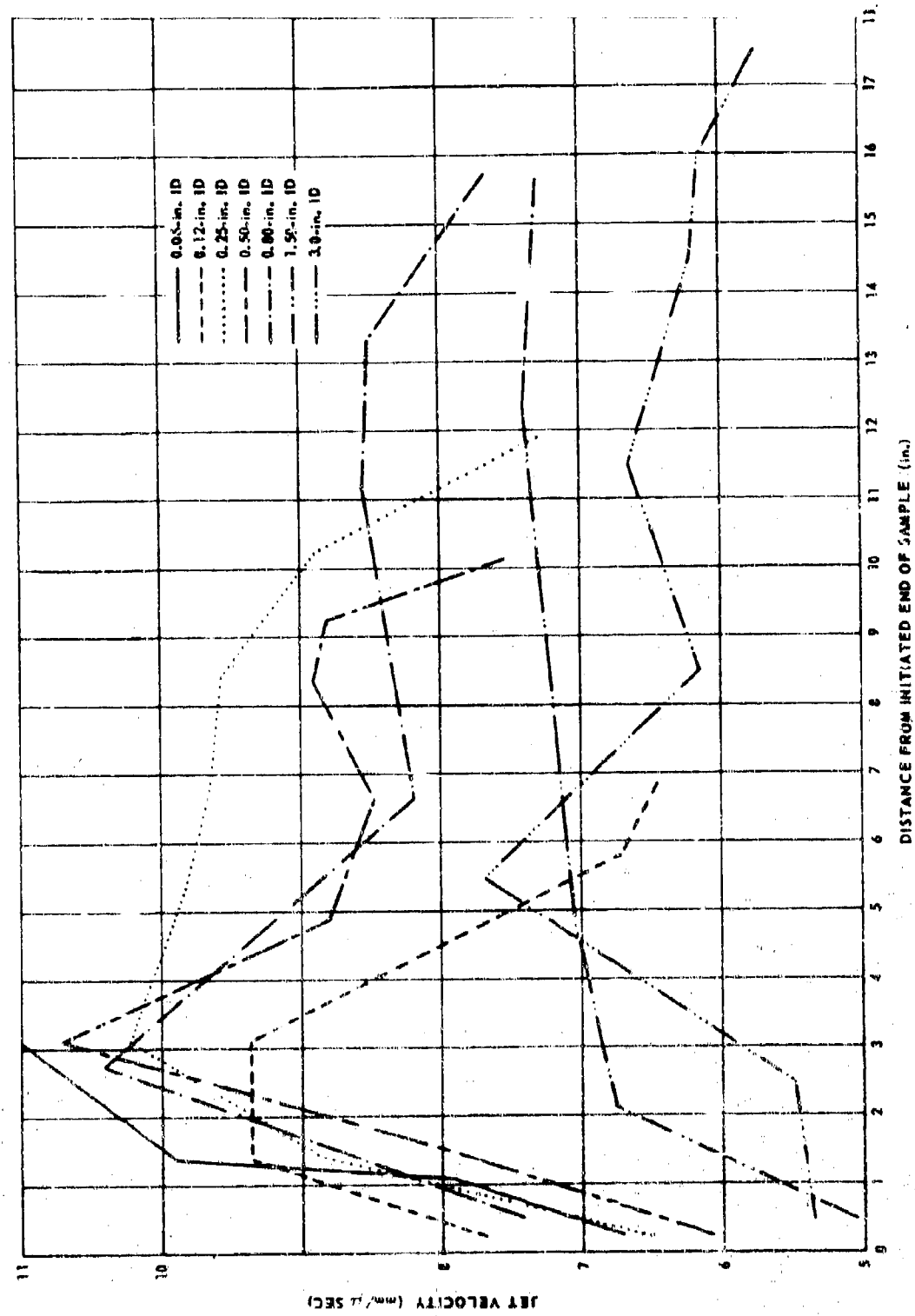


Figure IV-5. Jet Velocity in Hollow Cylinders of AAB-3189 Having 1.4-in. Web. (Obtained at Points on Axis of Sample)

## EFFECT OF LENGTH

To determine whether the abortion of steady-state detonation is caused by an end-effect mechanism, it is necessary to test samples that vary in length. In the series of tests described in the paragraphs entitled Effect of Core Diameter, samples having lengths equal to four times the OD were used. Since the web thickness was held constant the OD varied in the same increments as the ID, and the lengths, therefore, varied over a two-fold range. Since no correlation was found between the location of the fadeout point and the ID it follows that no correlation existed with the sample lengths either. However, a series of tests planned explicitly to investigate the length effect using samples of identical cross-section (4.50-in. OD by 1.50-in. ID).

Four sample lengths were tested: 18 in. ( $4 \times$  OD), 22.5 in. ( $5 \times$  OD), 27 in. ( $6 \times$  OD), and 36 in. ( $8 \times$  OD). The probe instrumentation was limited to two lengths: one set inserted to  $1/4$ -web thickness, the other to  $3/4$ -web thickness. Lexiglas was used to attenuate the booster shock wave.

Figure IV-6 shows the data obtained from the outer set of probes, reduced to detonation velocity vs distance along the sample. It is evident from these data that the sudden fading of the detonation velocity is not caused by an end effect. The fading begins after approximately 24 in., and it is therefore not observed in the two smaller lengths. It should be noted in comparing the results for the 1.5-in. web thickness extend the distance along the sample, through which a sustained detonation velocity occurs, from 7 to 24 in. This shows proof that, for a given material, the web size is the principal influence on the duration of a sustained detonation velocity, as judged by velocity data obtained near the outer surface of hollow samples.

Figure IV-7 reveals the extraordinary detonation velocity data obtained from the inner set of probes. The velocities increase due to near  $7.5$  mm/usec at the .4-in. distance. Again, to be prior of the detonation near the inner surface of hollow cylinders is seen to differ significantly from that near the outer surface. The outer portion of the web behaves more normally until the point is reached where the detonation fades. Since the inner portion is relatively more erratic, it is clear that a true steady state sustained detonation occurs for only a short distance and this detonation is in fact a transient phenomenon.

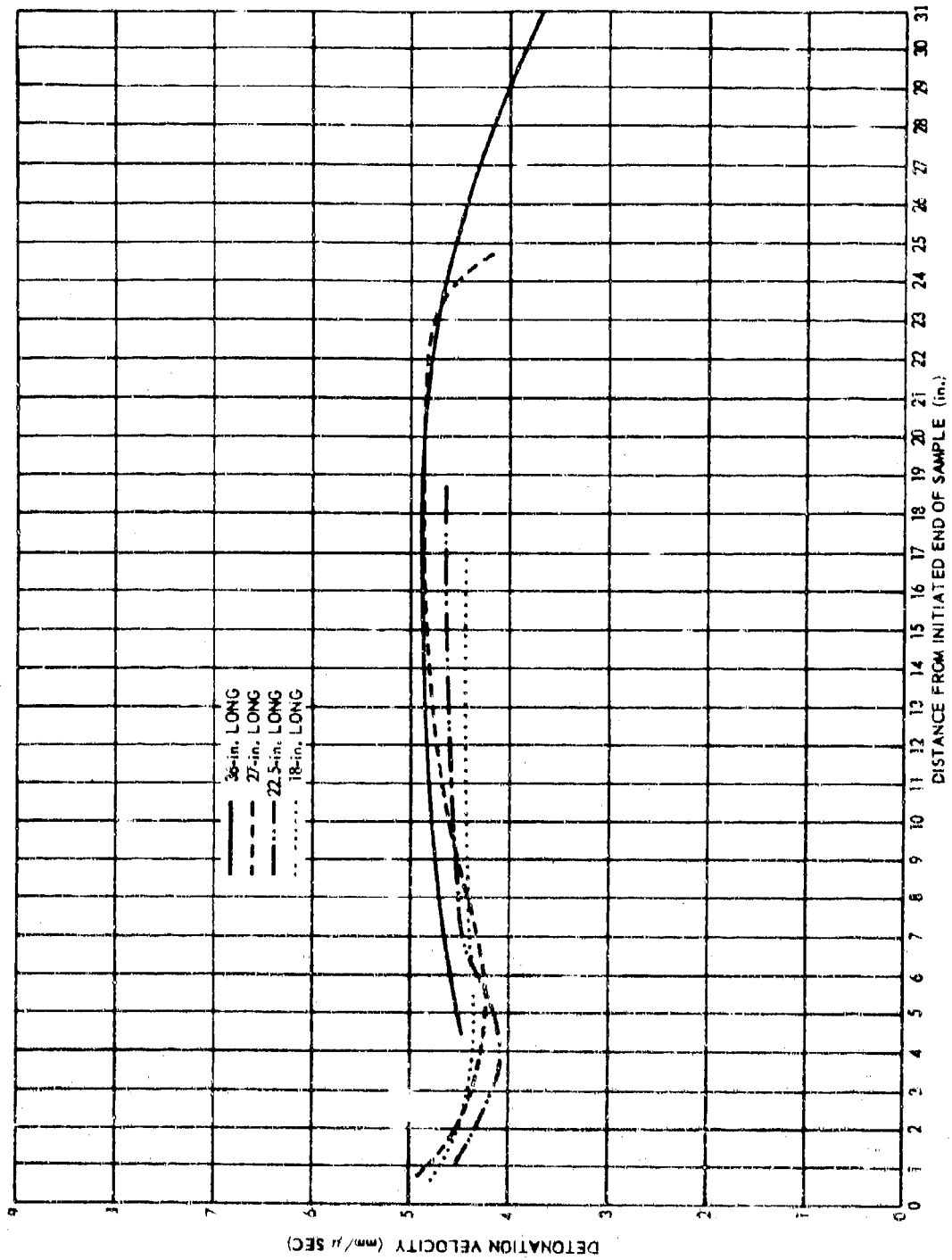


Figure IV-6. Detonation Velocity Behavior in 1.5-in. Web by 1.5-in. ID Hollow Cylinders of AAB-3189. (Obtained at Points 1/4-W into the Sample.)

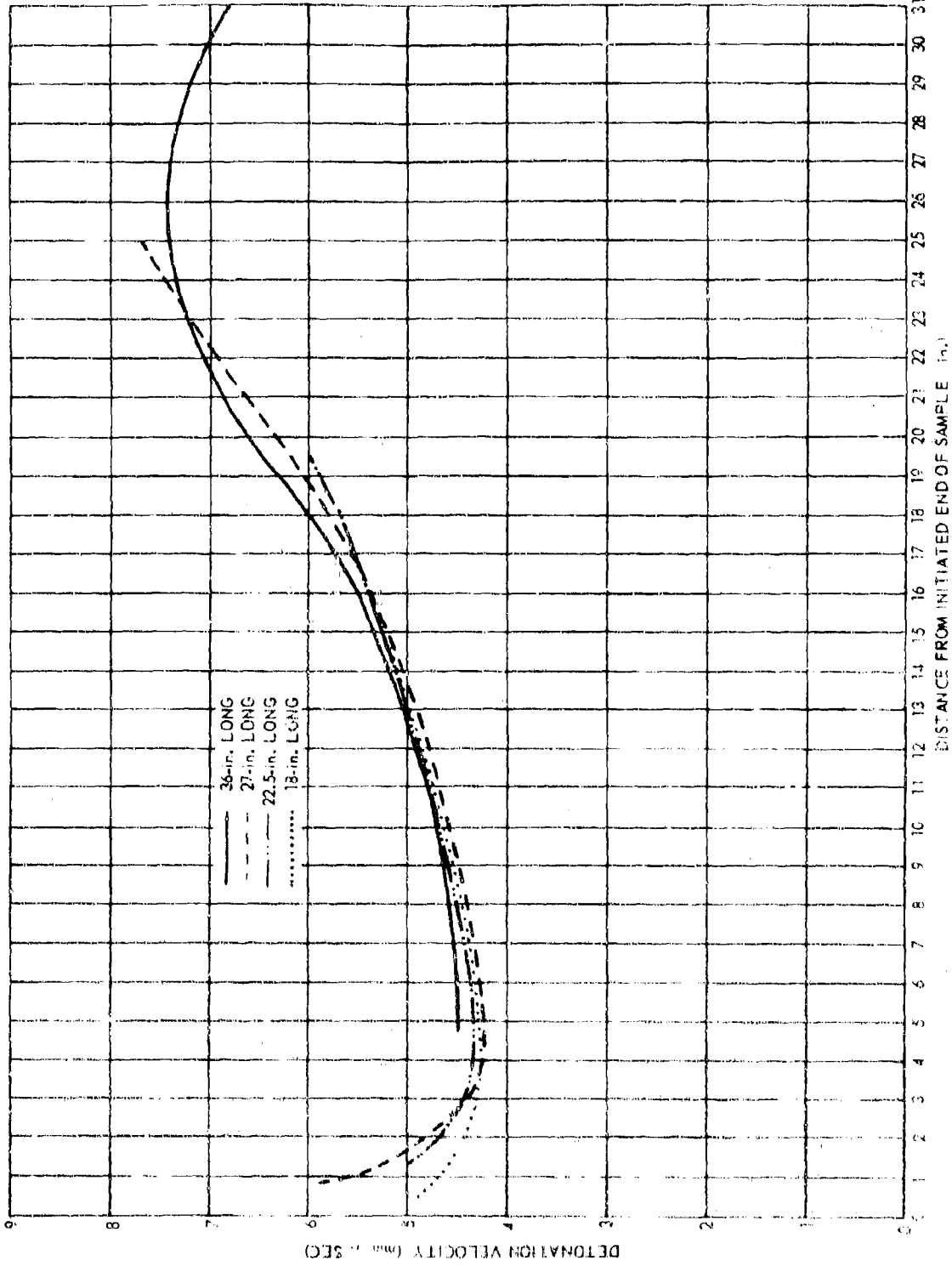


Figure IV-7. Detonation Velocity Behavior in 1.5-in. Web by 1.5-in. ID Hollow Cylinders of AB-389. (Obtained at Points  $\frac{3}{4}$  Web into the Sample)

## EFFECT OF WEB THICKNESS

Two samples of AAB-318<sup>9</sup> propellant were tested that measured 8-in. OD by 1.5-in. ID by 32-in. long. These were fired under the same conditions and with the same type of instrumentation as that shown in Figure IV-1. The data from the two tests were self-consistent. Figure IV-8 shows the velocity-vs-distance record of these tests and illustrates the behavior of detonation velocity in a hollow cylinder that has a web thickness (3.25 in.) that is much larger than the predicted pseudocritical web thickness (1.3 in.).<sup>5</sup>

Throughout the entire sample length the velocity of the wave over the outer half of the web remains constant (4.8 mm/ $\mu$ sec). At the 3/4-web depth, the same velocity is maintained for 10 in. and then the velocity increases very rapidly to reach an eventual maximum of 9.5 mm/ $\mu$ sec. The jet velocity increases to between 9.6 and 9.5 mm/ $\mu$ sec after 12.5 in.

Detonation of propellant at 9.5 mm/ $\mu$ sec is difficult to accept. Since this velocity agrees with the jet velocity, an alternative explanation for the high velocity registered by the 3/4-web probes can be postulated. Assume that the jet front causes ignition of propellant at the inner surface as it proceeds down the perforation. This is reasonable because of the high temperature and high pressure characteristics of the jet. Assume further that because of the high pressure in the perforation behind the jet front the propellant will burn at a fast rate. It follows that at a sufficient distance down the sample enough time would elapse between the passage of the high-velocity igniting jet front and the arrival of the lower-velocity reactive wave in the propellant to permit the burning propellant surface to reach the inner probes before the reactive wave in the propellant. Since the probes are triggered by shorting through a highly ionized medium, they could be triggered when the burning surface reaches them. The apparent velocity deduced from the inner (3/4-web) probes from that point on should be identical to the jet velocity, because the vector describing the regression of the burning inner surface in the longitudinal direction is equal to the velocity vector of the jet in the same direction (assuming a constant radial burning-rate vector).

<sup>5</sup>See paragraphs entitled Conclusions for a discussion of the critical geometry of hollow cylinders, and the definition of pseudocritical.

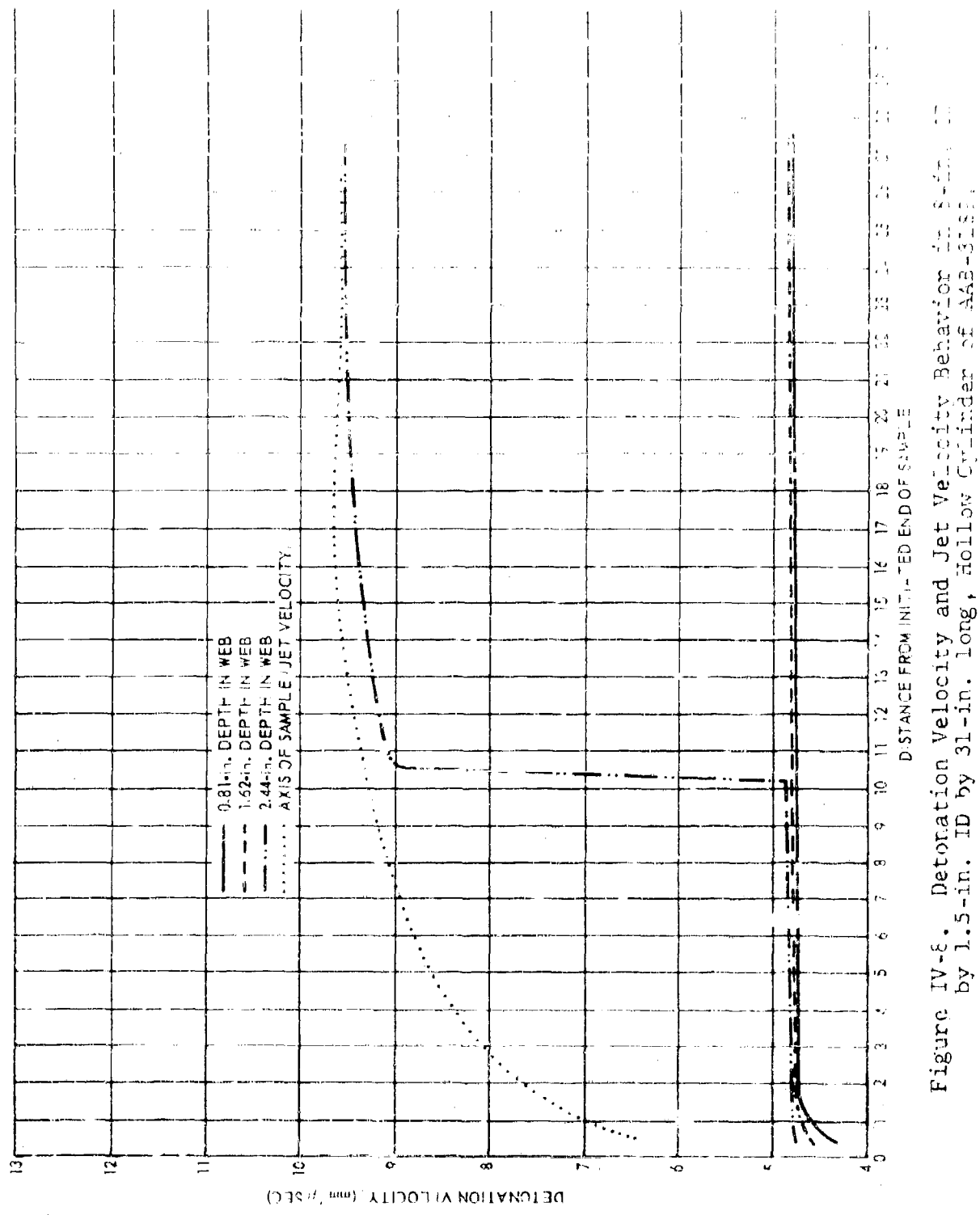


Figure IV-5. Detonation Velocity and Jet Velocity Behavior in a 31-in. long, hollow cylinder of AAB-333 by 1.5-in. ID by 31-in. long, hollow cylinder of AAB-333.

During the reported tests, it was found that the burning rate of ammonium perchlorate at 0.45 mm/min. was 0.03 mm/min. per centimeter of the jet front. For 0.45 mm/min. probability of detonation in 90 minutes requires an average burning rate of 0.45 mm/min. to produce flame burning, with data have been made. Using this rate extrapolation of the ammonium perchlorate burning-rate expression developed in Reference 17-2 yields an estimate of the pressure required to cause burning at 0.45 mm/min. This pressure estimate is approximately 5 and 10 kbar, using this equation:

$$B = 0.70 \sinh (1.59 \times 10^{-4} P) \quad (17-1)$$

where  $B$  is the burning rate (ips) at pressure  $P$  (psig). No measurement of the static pressure within a cylindrical jet cavity exists, so there is no way to determine the probability that such high burning rates are possible.

#### CONCLUSIONS

Based on the reported findings of the jetting phenomena test series, the following conclusions are made. By all considerations, these conclusions are subject to revision and correction pending further study of this complex problem..

- a. Core diameter does not affect the abnormal behavior of the detonation wave in hollow cylindrical samples.
- b. The abnormal behavior of the detonation wave is not caused by an end-effect mechanism.
- c. The principal cause for abnormal behavior of the detonation process in hollow cylindrical samples is the web thickness; specifically, the size of the web that exceeds a pseudocritical value, which is defined as that size below which no transitory sustainment occurs.
- d. The mechanism that causes abnormal quenching of the detonation process consists of a radial burning, directed outward from the inner surface, which proceeds at a high rate and reduces the web size to below the pseudocritical value.

The last conclusion expresses the present interpretation of the test results which does not consider any other perturbation to steady-state behavior than the high burning rate process. If such a process can continue unabated, clearly no classically supercritical hollow cylinder is possible. However, the duration

at high performance at a fixed distance does the projectile must penetrate the cylinder, because the jet slug must travel through length. Therefore it is possible that in hollow-core sample could be made having a web thickness by trigger time (or pseudocritical size) to receive supercritical value the limited jetting problem has consumed a portion of the inner web surface.

The entire jetting problem is not well enough understood in its basic fundamentals to allow further speculation about this and other possibilities. The primary question that remains unanswered is how a jet traveling at about twice the velocity of a detonation reaction in the web of a hollow sample continues to receive energy from that reaction despite the continuously increasing separation of the two fronts. If the jet velocity exceeds the detonation-wave velocity, steady-state conditions would be impossible in hollow-core samples. This fact alone rules out discussion of critical size and supercritical size, when speaking of the hollow cylinder. These terms need to be modified by using the prefix pseudo. Thus, pseudocritical geometry is defined as the minimum geometry in which detonation can be sustained for a minimal distance, and pseudosupercritical geometry is defined as any geometry larger than the pseudocritical geometry.

REFERENCES - WORK ACCOMPLISHED

IV-1. Large Solid-Propellant Binders Explosive Hazards Study Program (Project 80917), Technical Documentary Report AFRL-TR-65-214, Aerojet-General Report 0866-01(0)FP, 24 November 1965.

IV-2. Liwin, O. R., P. K. Selzman, and W. H. Andersen, "Deflagration Characteristics of Ammonium Perchlorate at High Pressures," Ninth Symposium (International) on Combustion, Academic Press, New York, pp 358-364. 1963.

## APPENDIX V

## CRITICAL GEOMETRY DATA, AAB-3149

Table V-I, Batch 4EH-85 Cylinders.

Diameter Mean (in.)	Standard Deviation (in.)	Density (gm/cc)	Results of Test	Average Detonation Velocity (mm/ $\mu$ sec)	Test No.
2.60	0.006	1.726	Go	4.28	3.2.1.62
2.60	0.004	1.725	Go	4.28	3.2.1.40
2.60	0.003	1.723	No go	--	3.2.1.35
2.60	0.005	1.723	Go	4.25	3.2.1.37
2.60	0.005	1.722	Go	4.33	3.2.1.38
2.61	0.004	1.735	Go	4.26	3.2.1.61
2.61	0.001	1.729	No go	--	3.2.1.63
2.61	0.002	1.729	Go	4.26	3.2.1.64
2.61	0.003	1.728	Go	4.31	3.2.1.42
2.61	0.001	1.727	Go	4.25	3.2.1.60
2.61	0.003	1.724	Go	4.30	3.2.1.31
2.61	0.004	1.724	Go	4.25	3.2.1.36
2.61	0.005	1.724	Go	4.29	3.2.1.33
2.61	0.004	1.721	No go	--	3.2.1.32
2.61	0.005	1.721	No go	--	3.2.1.34
2.61	0.005	1.721	No go	--	3.2.1.29
2.66	0.025	1.725	Go	4.38	3.2.1.47
2.67	0.005	1.731	Go	4.33	3.2.1.52
2.67	0.007	1.729	Go	4.34	3.2.1.57
2.67	0.003	1.728	Go	4.32	3.2.1.55
2.70	0.004	1.725	Go	4.33	3.2.1.30
2.73	0.006	1.732	Go	4.37	3.2.1.56
2.73	0.012	1.723	Go	4.35	3.2.1.41
2.72	0.002	1.716	Go	4.36	3.2.1.46
2.74	0.003	1.729	Go	4.32	3.2.1.59
2.74	0.004	1.728	Go	4.37	3.2.1.58
2.78	0.002	1.738	Go	4.38	3.2.1.69
2.78	0.007	1.729	Go	4.41	3.2.1.68
2.78	0.005	1.723	Go	4.38	3.2.1.45
2.78	0.006	1.715	Go	4.36	3.2.1.28
2.79	0.006	1.735	Go	4.40	3.2.1.53
2.79	0.004	1.733	Go	4.44	3.2.1.71
2.79	0.003	1.729	Go	4.30	3.2.1.72
2.79	0.004	1.728	Go	4.41	3.2.1.70
2.79	0.002	1.726	Go	(No Record)	3.2.1.44
2.79	0.005	1.721	Go	4.27	3.2.1.27
2.79	0.003	1.719	Go	4.39	3.2.1.67
2.79	0.005	1.719	Go	4.42	3.2.1.54
2.80	0.002	1.729	Go	4.41	3.2.1.51
2.80	0.001	1.727	Go	4.41	3.2.1.50
2.80	0.008	1.726	Go	4.38	3.2.1.43
2.80	0.003	1.720	Go	4.39	3.2.1.66
2.81	0.002	1.728	Go	4.38	3.2.1.48
2.81	0.006	1.724	Go	4.38	3.2.1.49

Average Density = 1.726 gm/cc

Standard Deviation = 0.0048 gm/cc

Table VIII. Batch 46H-35 Gy Iudex.

Row No.	Standard Deviation (cm.)	Density (gm./cc.)	Result of Test	Average Detonation Velocity (cm./usec.)	Standard Deviation of Velocity (cm./usec.)	Test No., 3, 2, 1
2.49	0.002	1.731	No go	--	--	76
2.49	0.001	1.728	No go	--	--	74
2.49	0.002	1.726	No go	--	--	77
2.49	0.002	1.722	No go	--	--	75
2.53	0.002	1.726	No go	--	--	79
2.55	0.003	1.725	No go	--	--	86
2.55	0.001	1.724	No go	--	--	84
2.55	0.002	1.723	No go	--	--	84
2.55	0.002	1.722	No go	--	--	85
2.55	0.001	1.722	No go	--	--	80
2.55	0.002	1.722	No go	--	--	78
2.55	0.002	1.721	No go	--	--	83
2.55	0.001	1.721	No go	--	--	82
2.55	0.002	1.721	No go	--	--	87
2.61	0.002	1.727	No go	--	--	96
2.61	0.001	1.725	No go	--	--	95
2.61	0.003	1.725	No go	--	--	93
2.61	0.001	1.725	No go	--	--	88
2.61	0.002	1.724	No go	--	--	97
2.61	0.002	1.724	No go	--	--	94
2.61	0.003	1.724	No go	--	--	91
2.61	0.002	1.724	No go	--	--	92
2.61	0.005	1.723	No go	--	--	89
2.61	0.003	1.721	No go	--	--	90
2.67	0.003	1.728	No go	--	--	99
2.67	0.002	1.727	No go	--	--	100
2.67	0.002	1.727	No go	--	--	104
2.67	0.002	1.726	No go	--	--	105
2.67	0.002	1.725	No go	--	--	101
2.67	0.002	1.722	No go	--	--	106
2.68	0.001	1.728	Go	4.12	0.23	103
2.68	0.001	1.727	Go	4.19	0.11	102
2.68	0.002	1.718	No go	--	--	98
2.74	0.004	1.732	No go	--	--	115
2.74	0.001	1.729	Go	4.21	0.10	111
2.74	0.001	1.729	Go	4.25	0.10	114
2.74	0.001	1.729	Go	4.25	0.10	116
2.74	0.003	1.728	No go	--	--	112
2.74	0.001	1.727	Go	4.25	0.03	109
2.74	0.001	1.727	No go	--	--	113
2.74	0.001	1.727	Go	4.29	0.06	108
2.74	0.001	1.726	Go	4.26	0.09	110
2.74	0.001	1.724	Go	(no record)	--	107
2.79	0.002	1.731	Go	4.21	0.11	120
2.79	0.004	1.725	Go	4.29	0.13	119
2.80	0.002	1.730	Go	4.27	0.06	118
2.80	0.003	1.729	Go	4.21	0.19	121
2.80	0.003	1.728	Go	4.16	0.10	117

Average Density = 1.726 gm./cc.

Standard Deviation = 0.0031 gm./cc. 62

Table V-102 - Width Test Reproducibility

Gate dimension Mean (in.)	Standard Deviation (in.)	Density (gm/cc)	Result of Test	Average Velocity (cm/usec)	Standard Deviation Velocity (mm/usec)	Test No. 3,2,1
2.22	0.012	1.726	No go	--	--	152
2.22	0.024	1.723	No go	--	--	154
2.22	0.010	1.723	No go	--	--	124
2.23	0.006	1.724	No go	--	--	153
2.23	0.006	1.723	No go	--	--	122
2.24	0.006	1.724	No go	--	--	123
2.27	0.009	1.722	No go	--	--	157
2.28	0.011	1.723	No go	--	--	156
2.29	0.029	1.723	No go	--	--	126
2.29	0.009	1.723	No go	--	--	127
2.30	0.019	1.725	No go	--	--	155
2.31	0.008	1.727	No go	--	--	132
2.31	0.017	1.724	No go	--	--	125
2.32	0.014	1.721	No go	--	--	129
2.33	0.010	1.723	No go	--	--	133
2.34	0.015	1.726	No go	--	--	128
2.34	0.017	1.721	No go	--	--	134
2.35	0.014	1.724	No go	--	--	158
2.38	0.050	1.727	No go	--	--	159
2.40	0.028	1.729	No go	--	--	135
2.41	0.031	1.730	No go	--	--	136
2.41	0.030	1.727	No go	--	--	137
2.42	0.011	1.723	No go	--	--	138
2.43	0.012	1.725	No go	--	--	142
2.43	0.037	1.724	No go	--	--	139
2.45	0.010	1.730	No go	--	--	140
2.45	0.010	1.727	No go	--	--	160
2.46	0.016	1.729	No go	--	--	130
2.46	0.004	1.729	No go	--	--	141
2.50	0.015	1.728	Go	4.12	0.211	131
2.50	0.012	1.726	Go	4.23	0.075	146
2.50	0.018	1.723	Go	4.27	0.078	161
2.51	0.007	1.723	Go	4.16	0.281	145
2.53	0.015	1.728	Go	4.30	0.051	144
2.54	0.010	1.727	Go	4.26	0.053	143
2.54	0.017	1.726	Go	4.31	0.124	162
2.55	0.014	1.723	No go	--	--	147
2.57	0.015	1.726	Go	4.28	0.111	164
2.58	0.024	1.728	Go	4.23	0.108	149
2.58	0.024	1.724	Go	4.28	0.078	163
2.60	0.010	1.726	Go	4.27	0.125	165
2.62	0.010	1.726	Go	4.28	0.053	148
2.62	0.013	--	Go	4.29	0.64	150
2.63	0.027	1.728	Go	4.35	0.046	169
2.63	0.025	1.725	Go	4.29	0.070	168
2.65	0.011	1.729	Go	4.35	0.064	167
2.68	0.021	1.727	Go	4.26	0.070	151
2.68	0.019	1.726	Go	4.34	0.069	166
2.68	0.022	1.725	Go	4.31	0.060	172
2.68	0.010	1.725	Go	4.30	0.091	175
2.68	0.016	1.723	Go	4.27	0.075	174
2.70	0.011	1.729	Go	4.29	0.087	173
2.70	0.008	1.726	Go	4.34	0.059	170
2.72	0.023	1.727	Go	4.32	0.054	171

Average Density = 1.725 gm/cc  
 Standard Deviation = 0.0023 gm/cc

Table V-IV. Perfectly Detonated Specimens and Test Data.

Mean Length (in.)	Standard Deviation (in.)	Density (gm/cc)	Average Detonation Velocity (mm/ $\mu$ sec)			Test No.
			Results of Test	Detonation Velocity (mm/ $\mu$ sec)	Test No.	
4.25	0.061	1.732	No go	--	3.3.2.2	
4.35	0.027	1.733	No go	--	3.3.2.3	
4.35	0.047	1.730	No go	--	3.3.2.8	
4.35	0.049	1.729	No go	--	3.3.2.9	
4.37	0.036	1.731	No go	--	3.3.2.10	
4.38	0.030	1.729	No go	--	3.3.2.11	
4.47	0.043	1.730	No go	--	3.3.2.12	
4.48	0.039	1.732	No go	--	3.3.2.13	
4.49	0.038	1.730	No go	--	3.3.2.4	
4.50	0.050	1.734	Go	4.24	3.3.2.1	
4.50	0.069	1.731	Go	4.25	3.3.2.5	
4.50	0.054	1.731	No go	--	3.3.2.15	
4.54	0.038	1.729	Go	4.32	3.3.2.6	
4.54	0.032	1.728	Go	4.26	3.3.2.16	
4.56	0.045	1.731	Go	4.30	3.3.2.7	
4.56	0.061	1.730	Go	4.29	3.3.2.14	
4.64	0.025	1.728	Go	4.34	3.3.2.21	
4.67	0.054	1.730	Go	4.31	3.3.2.20	
4.67	0.065	1.727	Go	4.32	3.3.2.18	
4.70	0.070	1.729	Go	No data	3.3.2.19	
4.75	0.052	1.731	Go	4.41	3.3.2.17	

Table V-V. Batch 4EH-110 1./5-in.-Thick Rectangles.

Geometry (in.)	Width (in.)	Results	Average Detonation Velocity (mm/ $\mu$ sec)		Test No.
			Test	Velocity (mm/ $\mu$ sec)	
2.60	5.00	No go	--		3.3.2.78
2.69	5.75*	No go	--		3.3.2.77
2.69	5.75	No go	--		3.3.2.49
2.66	5.875	No go	--		3.3.2.50
2.66	5.875	No go	--		3.3.2.51
2.71	6.00	No go	--		3.3.2.48
2.71	6.00	No go	--		3.3.2.42
2.71	6.00	Go	4.19		3.3.2.37
2.73	6.125	No go	--		3.3.2.46
2.73	6.125	No go	--		3.3.2.47
2.74	6.25	No go	--		3.3.2.45
2.76	6.50	Go	4.38		3.3.2.44
2.79	7.00	Go	4.24		3.3.2.43
2.86	7.75	Go	4.29		3.3.2.41
2.93	9.00	Go	4.29		3.3.2.38
2.96	9.50	Go	4.13		3.3.2.40
2.99	10.00	Go	4.26		3.3.2.39
3.05	11.75	Go	4.31		3.3.2.35

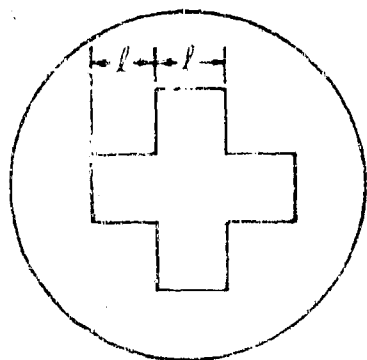
Sample length = 23.5 in  
Average density = 1.726 gm/cc

Velocity vs. Distance Test Data (continued from previous table)

TD (in.)	OD (in.)	Propagation Distance (in.)	Deflection Velocity (cm/ $\mu$ sec.)	Test No.
1.5	4.25	13	4.29	3.3.2.28
1.5	4.25	17	4.32	3.3.2.69
1.5	4.12	2.5	4.23	3.3.2.29
1.5	4.12	4	4.28	3.3.2.70
1.5	4.00	0	--	3.3.2.30
1.5	4.00	0	--	3.3.2.41
1.5	3.88	0	--	3.3.2.31
1.5	3.88	9	--	3.3.2.72
1.5	3.75	0	--	3.3.2.32
1.5	3.75	0	--	3.3.2.73
1.5	3.62	0	--	3.3.2.33
1.5	3.62	0	--	3.3.2.74
3.0	5.75	7	4.23	3.3.2.22
3.0	5.75	8.5	4.28	3.3.2.56
3.0	5.62	4.5	4.22	3.3.2.23
3.0	5.62	5	4.25	3.3.2.75
3.0	5.50	0	4.25	3.3.2.24
3.0	5.50	0	--	3.3.2.55
3.0	5.38	0	--	3.3.2.25
3.0	5.38	0	--	3.3.2.54
3.0	5.25	0	--	3.3.2.26
3.0	5.25	0	--	3.3.2.36
3.0	5.25	0	--	3.3.2.53
3.0	5.12	0	--	3.3.2.27
3.0	5.12	0	--	3.3.2.52

Project No. 971 - Relech 7000 ft. 0.000m. Green Gyl Indent

Width and Length $\ell$ (cm.)	OD (in.)	Propagation Distance (cm.)	Deflection Velocity (mm./sec.)	Test No.
0.5	4.25	8.5	4.33	3.3.2.66
0.5	4.12	8	4.23	3.3.2.65
0.5	4.00	0	--	3.3.2.63
0.5	3.88	0	--	3.3.2.67
0.5	3.75	0	--	3.3.2.65
0.5	3.62	0	--	3.3.2.68
1.0	5.75	8.5	5.35	3.3.2.62
1.0	5.62	8.5	5.28	3.3.2.61
1.0	5.50	6	4.29	3.3.2.60
1.0	5.38	0	--	3.3.2.34
1.0	5.25	0	--	3.3.2.58
1.0	5.12	0	--	3.3.2.57



MICROSCOPIC METHODS FOR DETERMINING VOID CONTENT

J. L. McGuire, Chemical Specialist  
Aerojet-General Corporation  
Sacramento, California

INTRODUCTION

This report is on that phase of the SOPHY program concerned with the evaluation of microscopic methods for determining binder void content. The objectives of this study were: (1) to determine whether small voids in the binder could be recognized with the microscope, (2) to evaluate microscopic methods for determining total binder void volume in a propellant sample, and (3) to determine the size range of voids in a propellant sample with the microscope.

VOID RECOGNITION

In Objective 1, the smallest void previously observed was 100  $\mu$ . Production samples contain voids of a minimum of 15  $\mu$  in diameter. A difference in the ability to recognize voids in this smaller size range results from the method of sample preparation. The propellant is microtomed into thin sections of a predetermined thickness. If this thickness is 30  $\mu$ , any void larger than 30  $\mu$  in diameter will pass completely through the thin section and is easily seen in transmitted light as clear white circles, as shown in Figure VI-1. This section is dry mounted for demonstration purposes; normally the section must be oil mounted, as in Figures VI-2 b, c, and d. If a void smaller than 30  $\mu$  is present, it will be totally included within the section. If oil does not penetrate the void it, in theory, will appear as a black opaque spot such as the dry void inside the AP crystal in Figure VI-2 c. The void is nearly opaque because it acts as a spherical mirror in transmitted parallel light. If parallel light is made to converge on the void with the swing-in substage condenser, a white spot appears in the center of the void as shown in Figure VI-2 d. In this way the void can be distinguished from spherical, completely opaque aluminum particles. This optical interpretation is confirmed when the same void is examined after the oil has penetrated the void and it is seen to transmit light. This reasoning will apply on voids down to about 1  $\mu$  in diameter.

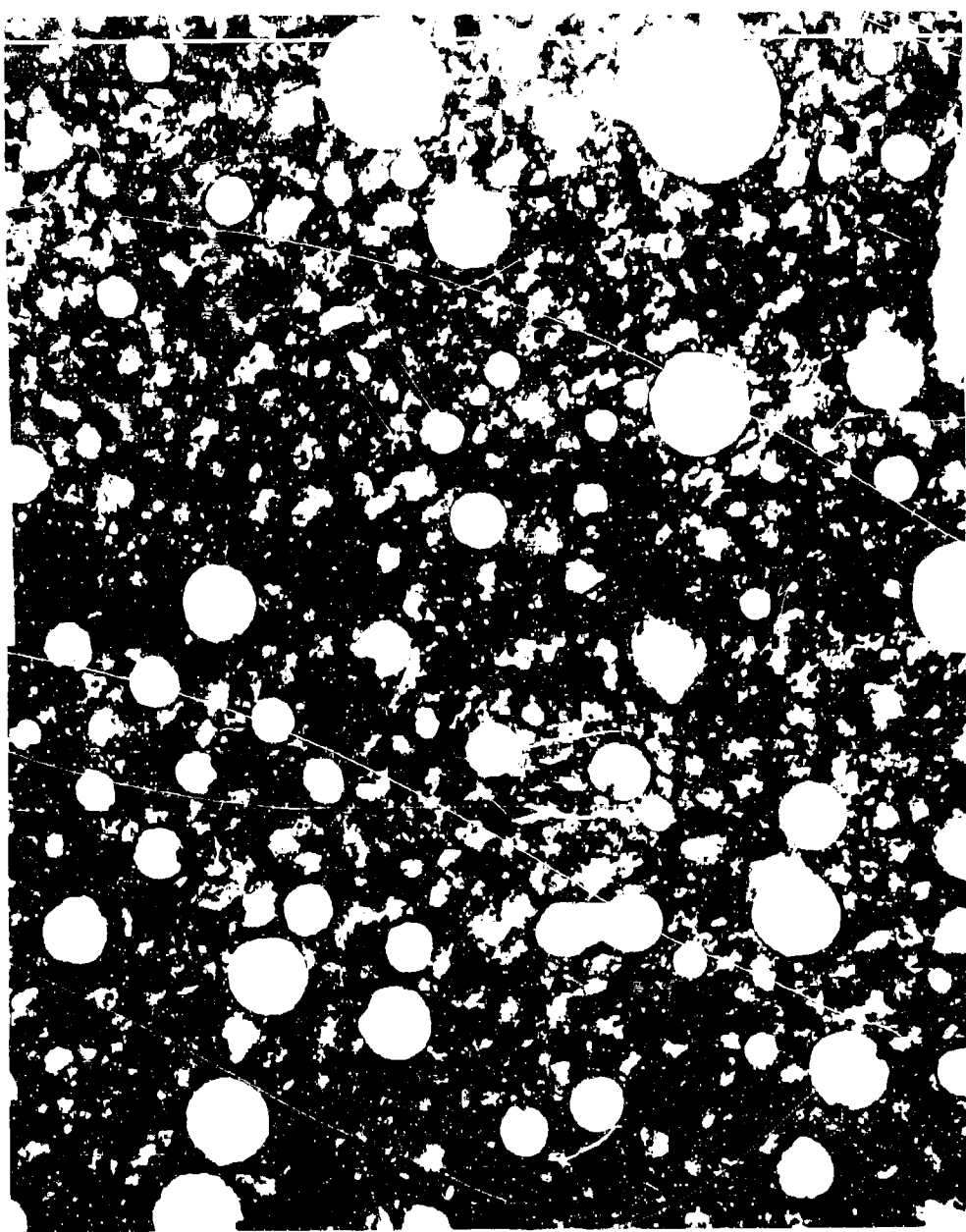
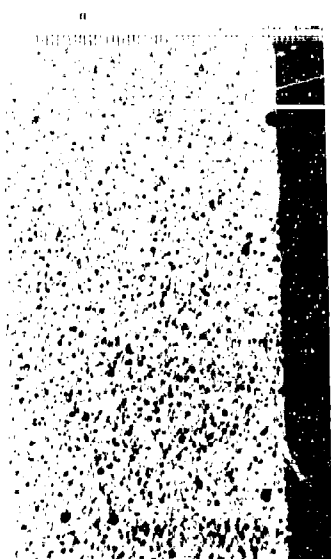
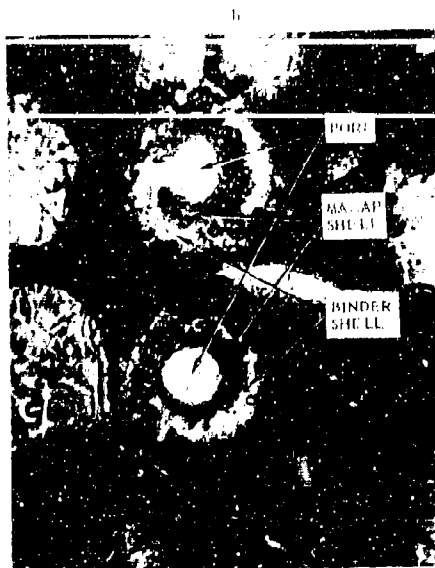


Figure VI-1. Photomicrograph of Porous Propellant (Dry Mounted).



PORES IN INCIDENT LIGHT.

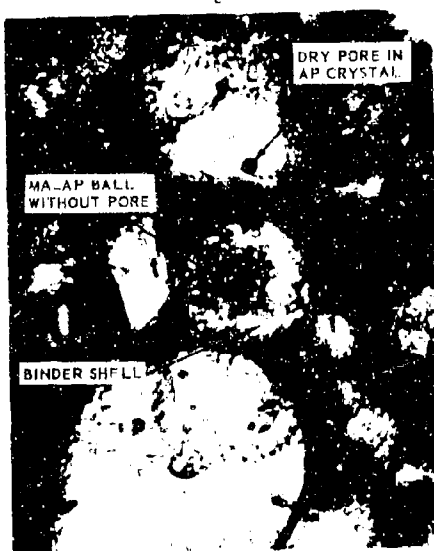
82.



PORE PASSING THROUGH SECTION.

86

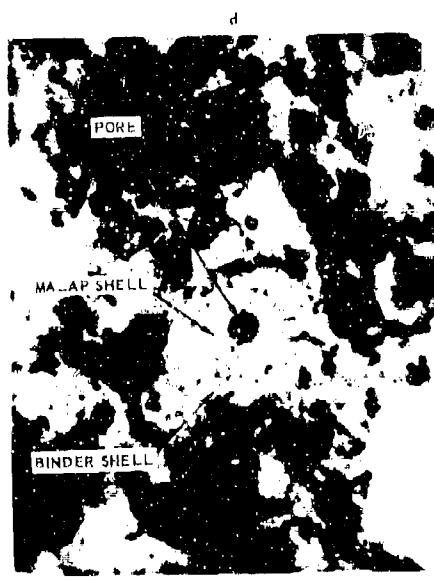
.125X



86

125X

13166-VI-2-1



PORE CONTAINED WITHIN SECTION.

86

.210X

Figure VI-2. Microscopy of Binder Pores.

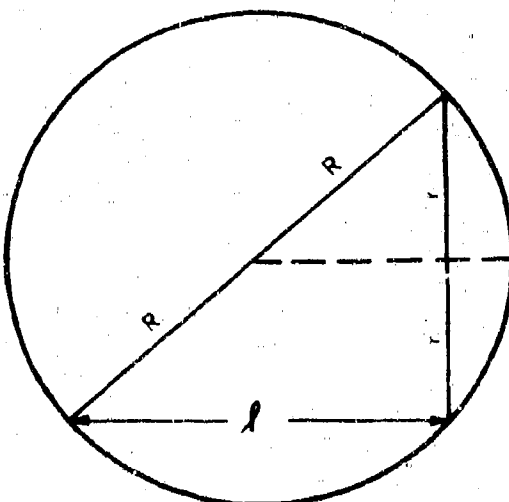
There is a unique morphological structure in the propellant around these small voids shown in Figure VI-2 b and c. The void is surrounded by a shell of MA-AP, which is in turn surrounded by a shell of clear binder. Two of these structures are shown in Figure VI-2 b. In Figure VI-2 c, the void is missing and a ball of MA-AP is off center in the shell of binder. This structure is useful for finding the small voids when counting.

#### THEORETICAL CONSIDERATIONS OF VOID VOLUME AND SIZE DISTRIBUTION

The determination of a volume from microscopic study of a two-dimensional field was mathematically developed by Rosiwal in 1898. Numerous tests were conducted and a review of the procedure by E. S. Larsen and F. S. Miller was published in the Journal of Mineralogical Society of America, Vol. 20, No. 4, April 1935, in which they state "that the linear method of Rosiwal is easily capable of an accuracy within 1 or 2 percent for each constituent."

In SOPHY propellant, the voids are considered to consist of a series of different size spheres, randomly distributed with a loose packing. This condition is slightly different from the Rosiwal problem for an intimately packed crystalline mosaic; however, the technique should be valid.

The distribution of void sizes was given a partial mathematical development by R. Farris of Aerojet-General by limiting the problem to spherical voids of one size, and is as follows:



If  $\ell$  is the chord length of a sphere of radius  $R$ , then  $2r$  is the other leg of the triangle normal to  $\ell$  and  $2R$  is the hypotenuse of a right triangle passing through the center of the sphere,

$$\left. \begin{aligned} (2R)^2 &= \ell^2 + (2r)^2 && \text{OR} \\ r &= \sqrt{R^2 - \ell^2/4} \end{aligned} \right\} \quad (\text{VI-1})$$

If a line of normal incidence intersects the sphere at distance of radius  $r$ , the circle formed by this radius represents the locus of all chords of length  $\ell$ . So that

$$\begin{aligned} \text{when } \ell &= 2R, & r &= 0 \\ \text{and } \ell &= 0, & r &= R \end{aligned} \quad (\text{VI-2})$$

If the probability of intersecting any point on the circle is the same, then the probability  $P$  of measuring a chord length from  $\ell = 0$  to  $\ell$  is

$$P(\ell) - P(0) = \frac{\pi r^2}{\pi R^2} \Big|_0^\ell = \frac{\pi(R^2 - \frac{\ell^2}{4})}{\pi R^2} \Big|_0^\ell = \frac{\ell^2}{4R^2} = \frac{\ell^2}{D^2} \quad (\text{VI-3})$$

where  $D$  is the diameter of the void. Therefore, Farris concludes, if a histogram is plotted on log-log paper, it should have a slope of 2 and an intercept of  $1/D^2$ .

A graphical model was constructed with spheres of one size. The Rosiwal equation  $100x/(x+y+z)$  was used to calculate the volume of voids and a plot was made to determine the slope. The results were slightly in error, presumably because of the small size of the graphical model, but sufficiently accurate to proceed with this experiment.

#### VOID VOLUME

An experimental run was made on Sample 82, which is visually similar to the sample in Figure VI-2 a, to determine the void volume. Two different microscopic methods were used. Both made use of the linear method of traversing the thin section and recording the linear intercepts of propellant and void along a line. In one method, an eyepiece micrometer was used to measure each intercept distance and resulted in a tabulation of each void. In the other method, the Leitz Integrating Stage was used which gives a cumulative reading of all intercepts and the number of voids was not recorded.

On the test sample, the length of the linear traverse was 7.48 cm and the percent void volume calculated was 11.4% using the eyepiece micrometer. A short traverse of 1.3 cm gave 11.0% void volume using the integrating stage. A density determination on the bulk samples by an oil displacement method on an analytical balance gave a void volume of 12.5%. The 1% discrepancy should be due to a few larger pores in the bulk sample that were deliberately avoided in microtomizing the thin section. The method using the integrating stage required 20 min while the eyepiece micrometer method required all day.

#### VOID SIZE DISTRIBUTION

When the above eyepiece measurements of individual voids were plotted on log-log paper, the slope of the line was approximately 1, which indicates a distribution of void sizes. The mathematical procedure developed by R. Farris could be extended to determine the void size distribution from this single line, but would require several weeks. Lacking this method, an experimental method was attempted. In studying the voids at high magnification, it was noticed that the walls of the voids passing through the thin section were cusped up or down, and a few were vertical. From the geometry of these voids, it is apparent that cusped walls are formed by minor circles in a sphere and the vertical walls are from a great circle. Thus, by scanning the thin section and measuring the diameter of holes with vertical walls, the void size distribution can be recorded. Voids that do not pass through the section always give a great circle projection and all of these can be measured. To find sufficient voids for measurement, several thin sections were cut from different parts of the block sample No. 82. A total of 207 voids were recorded with a size range from 1204 to 17  $\mu$ . The data were statistically reduced and placed on normal probability paper, Figure VI-3. There is a dog leg in the curve at the median point and another where three very large voids appear. Two dog legs were expected on the basis that there is a bias in counting a greater number of voids that do not pass through the thin section and, secondly, as previously reported, some of the very large voids were obviously the result of coalescence of the two smaller voids. Interestingly, the bias on the graph of the smaller voids is in the wrong direction and the size is about twice the thickness of the thin section. This corresponds to the size range of the voids which are enclosed in the unique binder shells shown in Figures VI-2 b and c. Disregarding the few cases of coalescence, it appears that there may be a bimodal distribution of void sizes.

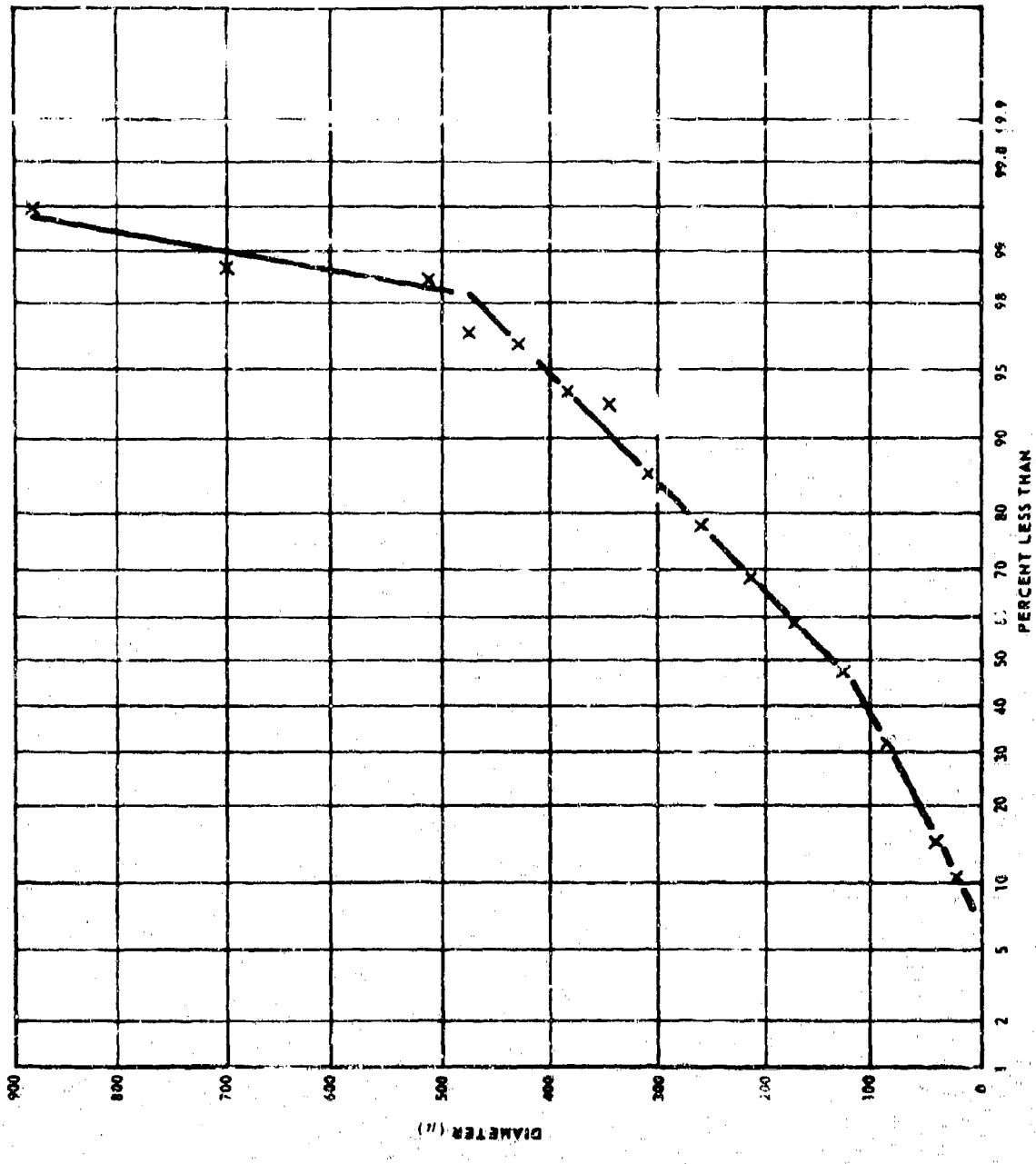


Figure VI-3. Distribution of Pore Sizes.

## CONCLUSIONS

By microscopic study of microtomed propellant thin sections, the void content by volume and the size distribution of voids larger than  $10 \mu$  can be determined. Although the number of counts must be increased, sufficient data can be obtained for statistical analysis. Both mathematical and experimental approaches agree and can be improved upon. The void size distribution could be determined from one set of measurements by expanding the math of Ferris instead of the two sets of measurements made above. The statistical bias and possibility of bimodal distributions could be experimentally investigated by adding polystyrene beads of predetermined size range to a polymer and then carrying out the microscopic analysis.

APPENDIX VII  
SHOCK PRESSURE ATTENUATION IN PLEXIGLAS

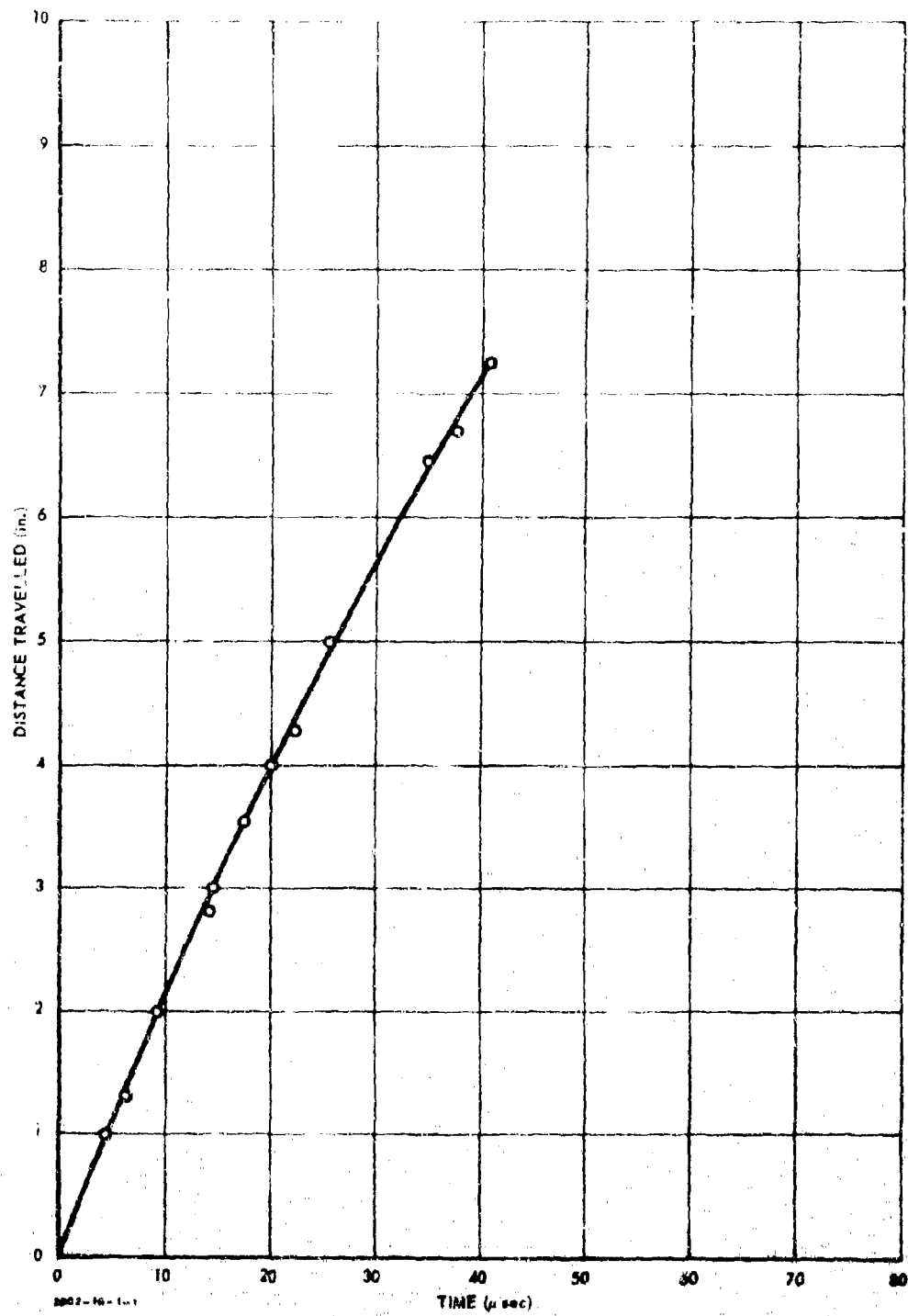


Figure VII-1. Shock Wave Attenuation in 8-in. Squares of Stacked PMMA Plates, TNT Rocster.

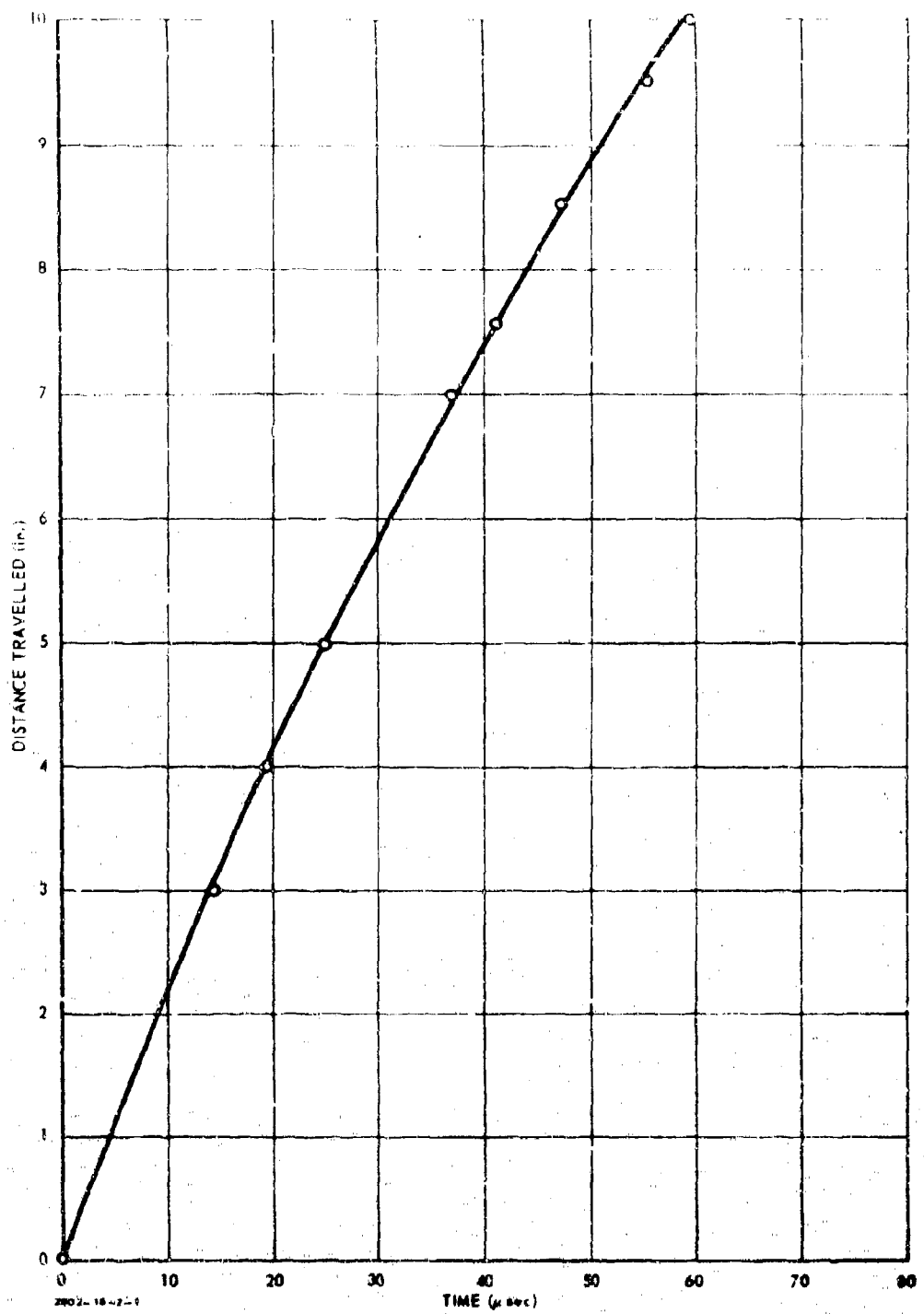


Figure VII-2. Shock Wave Attenuation in 10-in. Squares of Stacked PMMA Plates, TNT Booster.

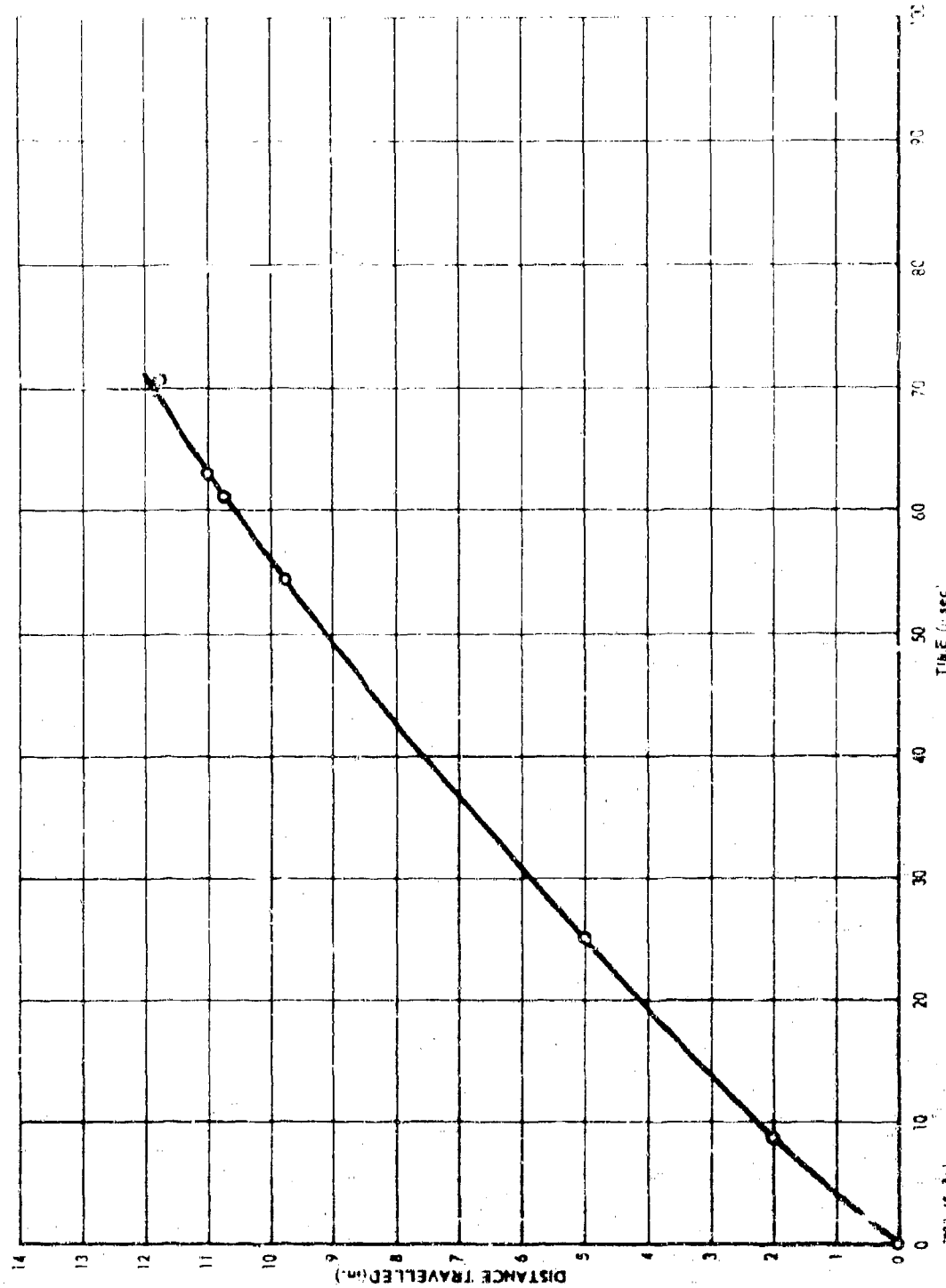


Figure VIII-3. Shock Wave Attenuation in 12-in. Squares of  
Stacked PMMA Plates, TNT Booster.

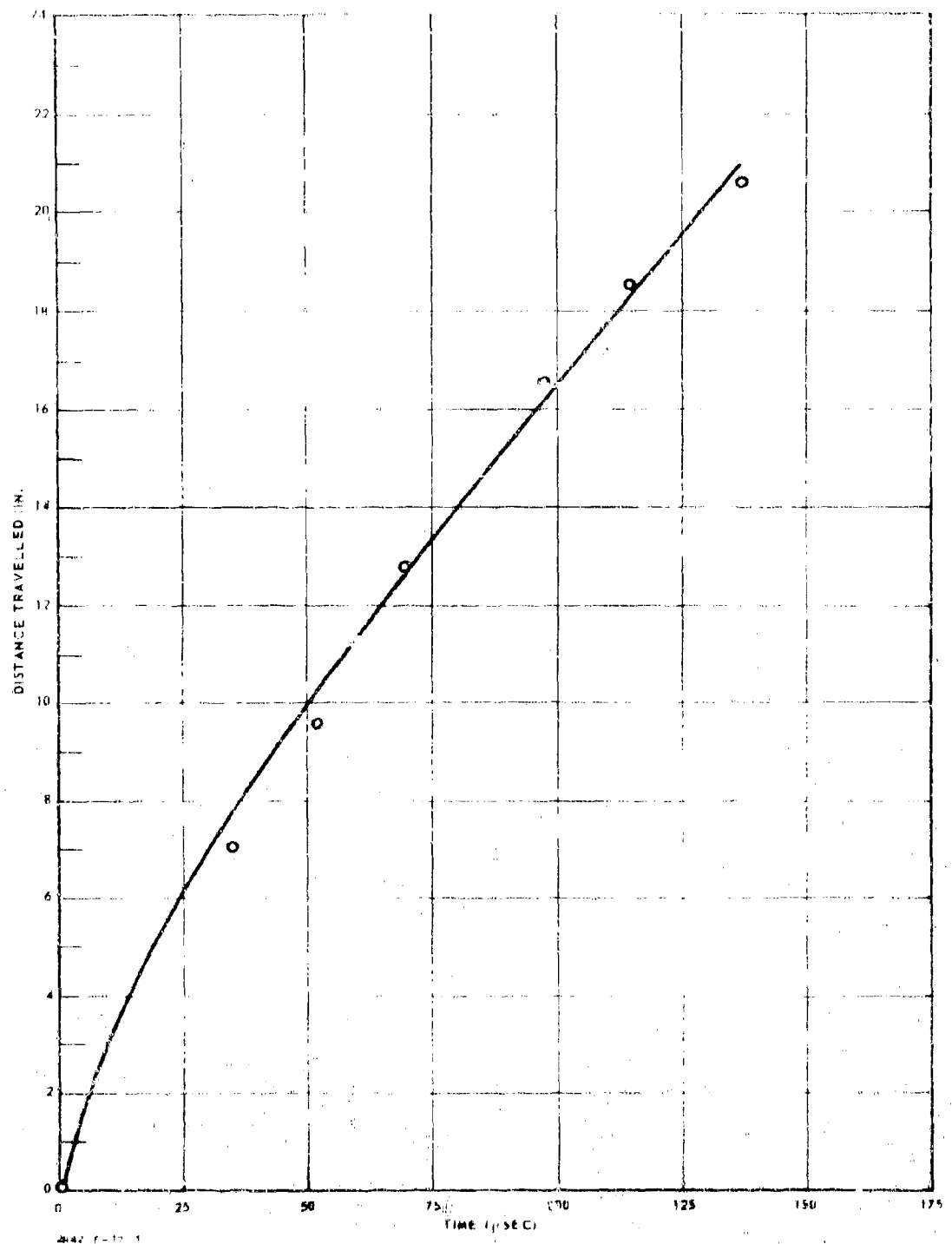


Figure VII-4. Shock Wave Attenuation in 20-in. Squares of Stacked PMMA Plates, TNT Booster.

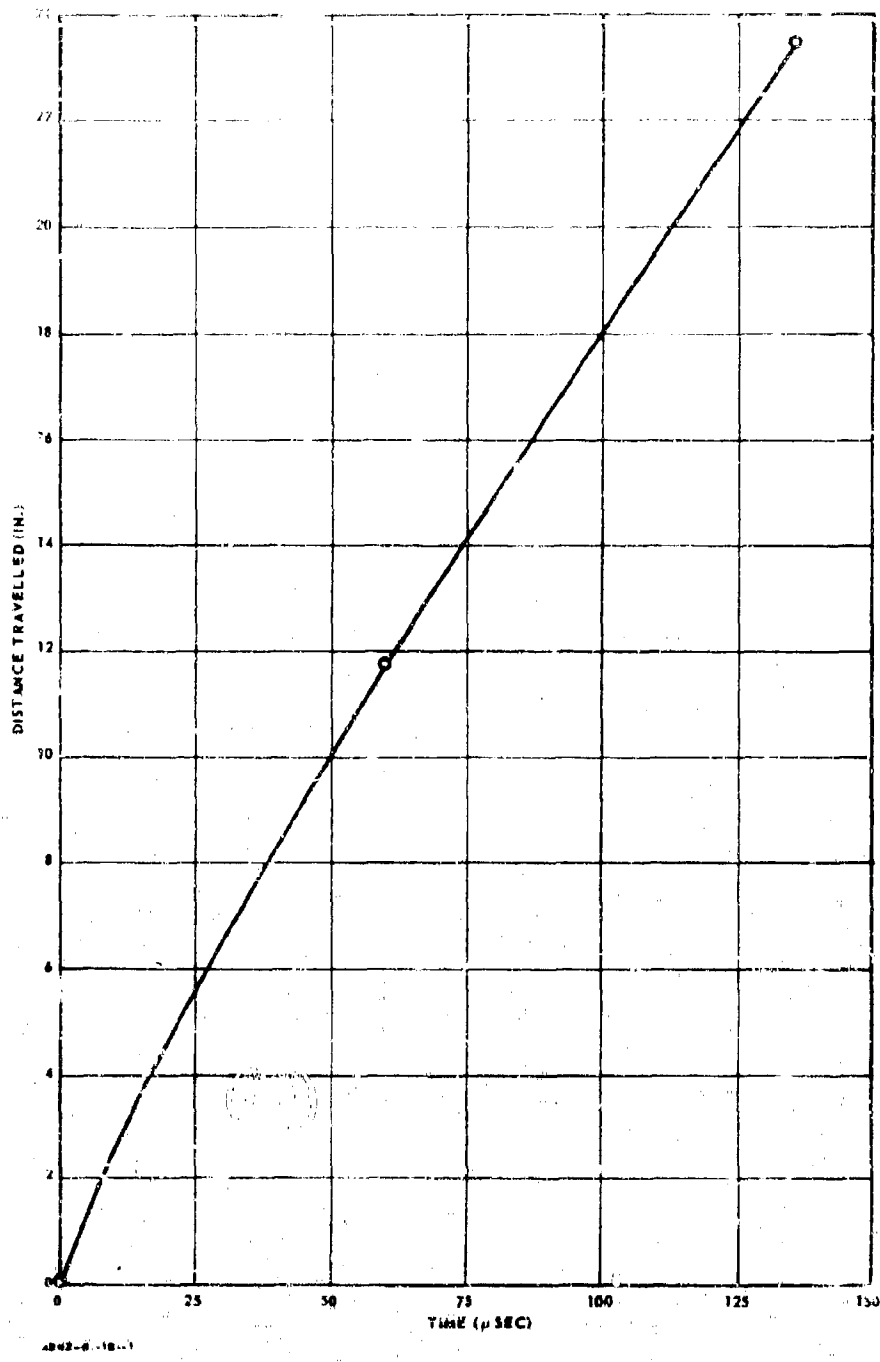


Figure VII-5. Shock Wave Attenuation in 24-in. Squares of Stacked PMMA Plates, TNT Booster.

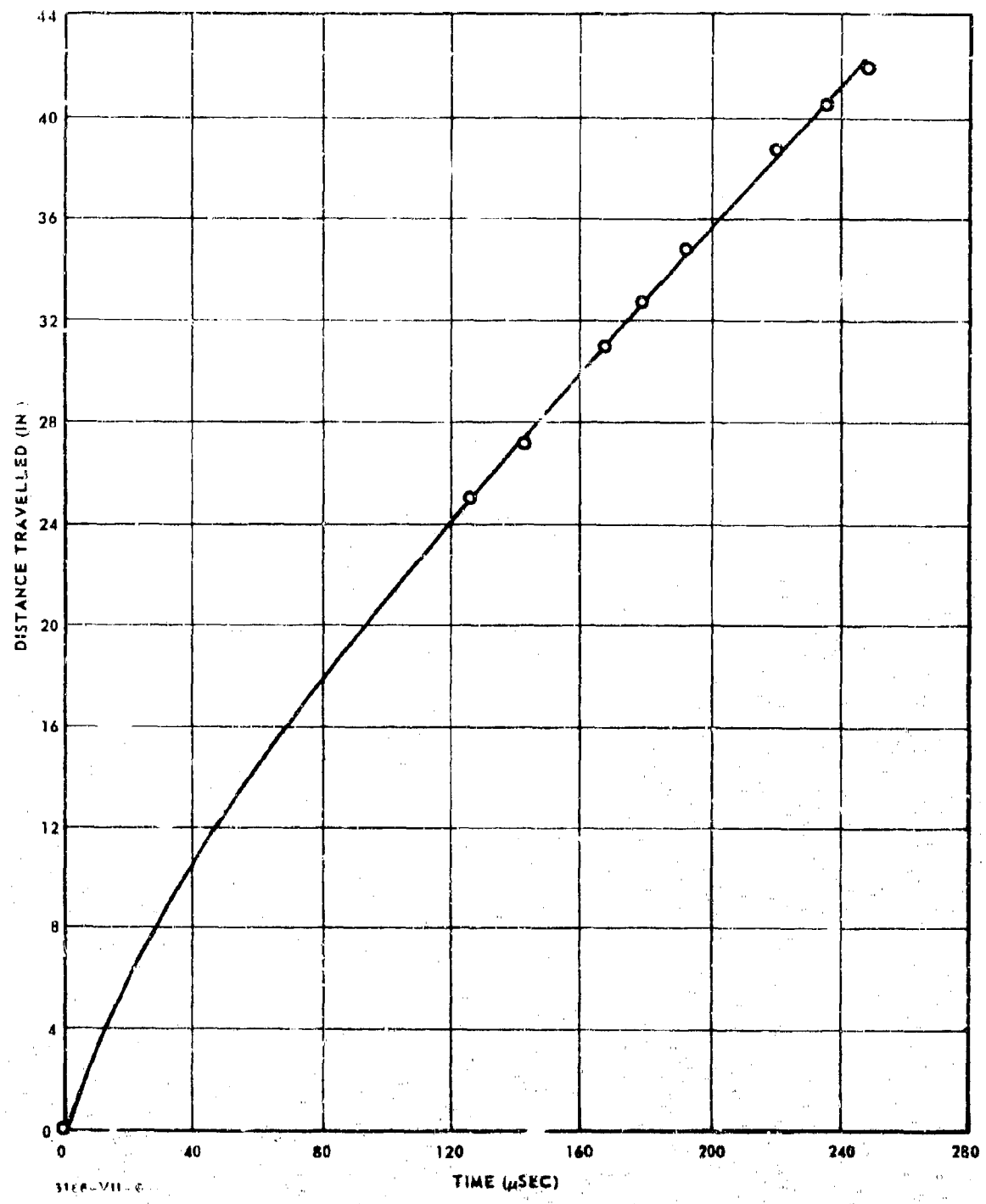


Figure VII-6. Shock Wave Attenuation in 42-in. Squares of  
Stacked PMMA Plates, TNT Booster.

APPENDIX VIII  
SHOCK PRESSURE AND WAVE AREA DATA

Table VIII-I. Circular Cylindrical Acceptor.

Test No.	Time (μsec)	h (in.)	r (in.)	x <sub>1</sub> (in.)	Average Pressure (kbar)	Shock Wave Area (in.) <sup>2</sup>
3.3.7.1	5.0	-0.88	1.84	0	31.43	11.1
	10.0	-0.54	2.31	0.67	16.04	15.85
	15.0	-0.62	3.04	1.24	9.91	22.60
	20.0	-0.63	3.60	1.85	6.35	25.60
	25.0	-0.59	4.06	2.50	3.97	24.86
	30.0	-0.29	4.23	3.23	2.26	18.99
	35.0	0.23	4.14	3.95	1.03	10.94
3.3.7.2	5.0	-0.34	1.65	0.21	52.79	11.40
	10.0	0.30	2.03	1.12	33.27	15.49
	15.0	0.51	2.67	1.69	25.70	24.90
	20.0	1.07	2.93	2.45	21.90	28.50
	25.0	1.42	3.34	3.04	20.25	31.15
	30.0	1.48	4.01	4.14	28.00	33.99
	35.0	1.80	4.48	5.13	34.30	32.45
3.3.7.3	5.0	0.06	1.04	0.44	41.33	4.29
	10.0	-0.71	2.69	0.42	29.74	26.38
	15.0	-0.20	3.02	1.25	20.77	29.80
	20.0	0.81	2.75	2.30	14.59	21.76
	25.0	1.03	3.15	2.92	10.50	24.90
	30.0	1.12	3.65	3.54	7.40	28.30
	35.0	0.83	4.47	4.14	5.55	32.47
3.3.7.4	5.0	-0.52	1.56	0.10	34.54	9.24
	10.0	0.13	1.77	0.93	24.70	10.82
	15.0	0.17	2.47	1.38	19.40	19.50
	20.0	0.60	2.77	2.07	15.66	22.68
	25.0	0.92	3.12	2.67	13.01	26.76
	30.0	1.08	3.60	3.20	11.09	33.31
	35.0	1.25	4.03	3.94	10.99	33.91
3.3.7.5	5.0	-0.83	2.08	0.00	55.10	16.34
	10.0	-0.57	2.79	0.52	36.05	29.87
	15.0	-0.11	3.25	1.26	29.53	38.43
	20.0	0.33	3.68	2.46	34.35	35.80
	25.0	0.57	4.26	3.59	41.86	33.07
	30.0	0.74	4.91	4.63	50.58	31.56
	35.0	1.45	5.10	5.57	60.80	31.27

Table VIII-I. Circular Cylindrical Acceptor (Cont.)

Test No.	Time (usec)	h (in.)	r (in.)	$x_1$ (in.)	Average Pressure (kbar)	Shock Wave Area (in.) <sup>2</sup>
3.3.7.6	10.0	0.30	1.94	1.13	28.02	13.49
	15.0	0.50	2.52	1.72	20.96	20.81
	20.0	0.97	2.80	2.41	17.23	24.01
	25.0	1.37	3.11	3.03	15.34	28.37
	30.0	1.82	3.34	3.63	14.59	32.09
	35.0	2.33	3.50	4.22	14.70	35.35
3.3.7.7	5.0	0.51	0.75	0.77	47.68	2.31
	10.0	0.44	1.71	1.09	38.20	11.39
	15.0	0.68	2.35	1.64	32.17	20.57
	20.0	1.56	2.39	2.59	28.06	20.48
	25.0	2.42	2.42	3.50	25.53	20.42
	30.0	3.20	2.47	4.32	24.18	20.93
	35.0	3.84	2.56	5.01	23.62	22.32
3.3.7.8	10.0	-0.17	1.98	0.76	21.99	13.05
	15.0	-0.02	2.56	1.31	16.60	19.80
	20.0	0.48	2.76	2.03	13.03	20.96
	25.0	0.94	2.92	2.69	10.62	21.50
	30.0	1.47	2.99	3.36	8.79	20.68
	35.0	2.04	2.99	4.02	7.40	19.00
3.3.7.12	10.0	0.56	1.79	1.45	18.77	10.11
	15.0	0.50	2.53	1.87	14.56	18.40
	20.0	0.74	3.00	2.39	14.00	25.48
	25.0	0.89	3.48	2.70	16.39	36.42
3.3.7.14	5.0	0.46	0.84	0.73	58.11	3.02
	10.0	1.36	0.93	1.81	20.88	2.83
	15.0	0.23	2.78	1.59	19.77	24.83
	20.0	0.69	3.10	3.35	15.27	28.14
	25.0	1.42	3.16	3.19	13.11	27.54
	30.0	1.72	3.50	3.71	12.57	33.20
	35.0	2.31	3.59	4.33	13.02	35.44

Table VIII-II. Rectangular Acceptor.

Test No.	Time (usec)	h (in.)	R (in.)	k (in.)	r (in.)	Average Pressure (kbar)	Shock Wave Area (in.) <sup>2</sup>
3.3.8.2	5.0	-3.02	4.16	-1.69	2.91	120.02	22.92
	10.0	-2.11	4.16	-1.80	3.89	111.89	32.84
	15.0	-1.41	4.35	0.02	3.01	107.85	40.49
	20.0	-0.62	4.45	0.61	3.29	101.13	41.81
	25.0	-0.07	4.77	0.99	3.78	93.42	40.00
	30.0	0.67	4.92	1.76	3.90	89.11	39.23
	35.0	1.44	5.05	2.62	3.93	86.52	38.73
	40.0	2.09	5.31	3.52	3.93	84.86	38.02
	45.0	2.81	5.48	4.13	4.22	84.24	37.28
	50.0	3.54	5.66	3.88	5.33	84.01	36.36
	55.0	4.03	6.06	4.95	5.16	85.89	35.88
	60.0	4.60	6.38	5.48	5.52	88.83	35.28
	65.0	5.24	6.66	6.38	5.52	93.43	33.84
	70.0	5.48	7.29	7.55	5.52	100.09	34.76
3.3.8.3	5.0	-5.06	6.32	-3.61	4.89	124.30	31.00
	10.0	-3.29	5.47	-2.37	4.57	112.69	36.88
	15.0	-0.95	4.03	-0.81	3.94	106.64	37.48
	20.0	-1.93	5.85	-0.77	4.70	91.40	36.40
	25.0	-1.14	5.47	1.36	3.48	86.77	37.36
	30.0	-1.17	6.85	0.38	5.31	78.51	35.04
	35.0	0.01	6.52	2.40	4.20	77.15	35.92
	40.0	-3.87	11.27	3.10	4.36	72.41	34.00
	45.0	1.45	6.81	3.83	4.51	74.27	35.44
	50.0	0.38	8.75	4.44	4.75	73.62	34.32
	55.0	0.59	9.42	5.30	4.80	75.43	34.08
	60.0	-1.91	12.08	6.08	4.88	77.91	30.80
	65.0	4.19	7.61	6.73	5.14	85.36	34.60
	70.0	3.19	9.42	7.18	5.52	90.39	33.80
	75.0	2.55	10.96	7.81	5.77	99.23	33.44

APPENDIX IX  
FLYER PLATE DATA

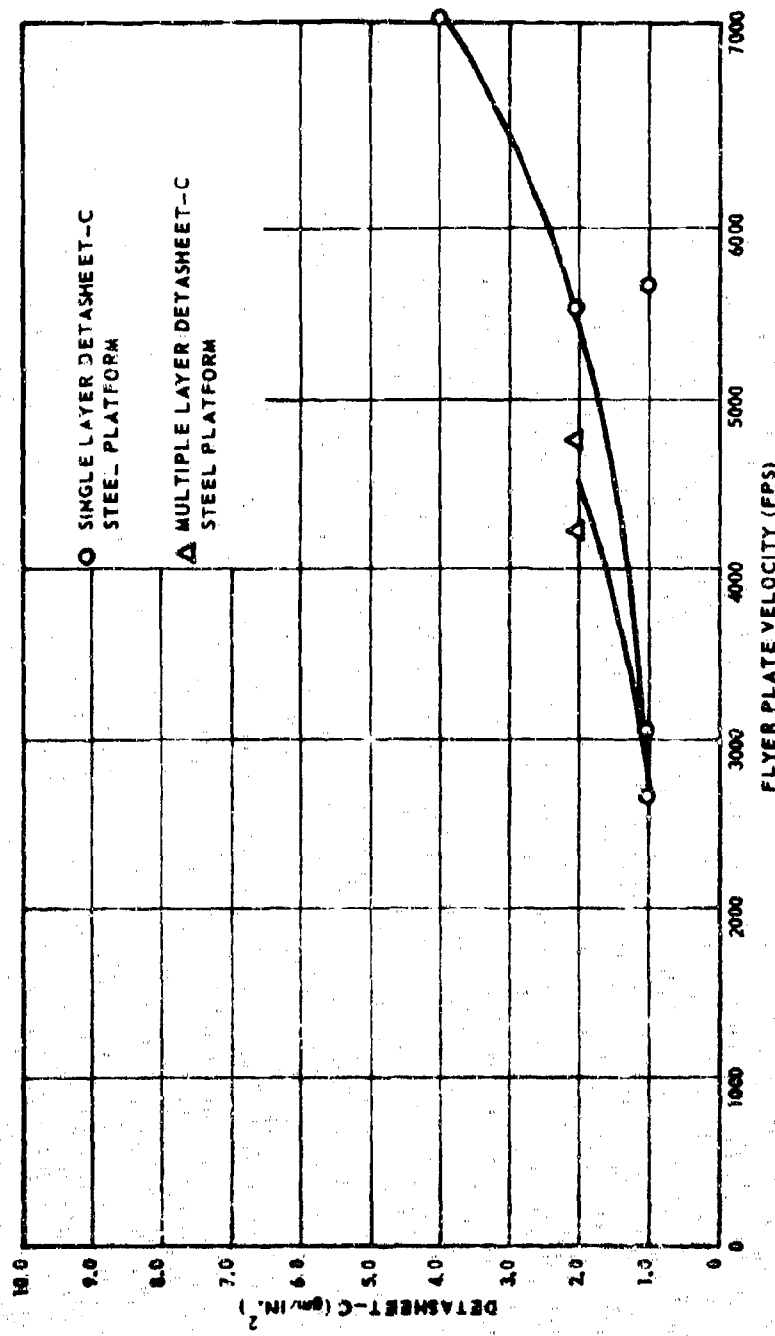


Figure IX-1. Flyer Plate Velocity vs Wt/Sq In. of Datasheet-C.  
(Aluminum Flyer Plate 0.0625 in. by 5 in.)

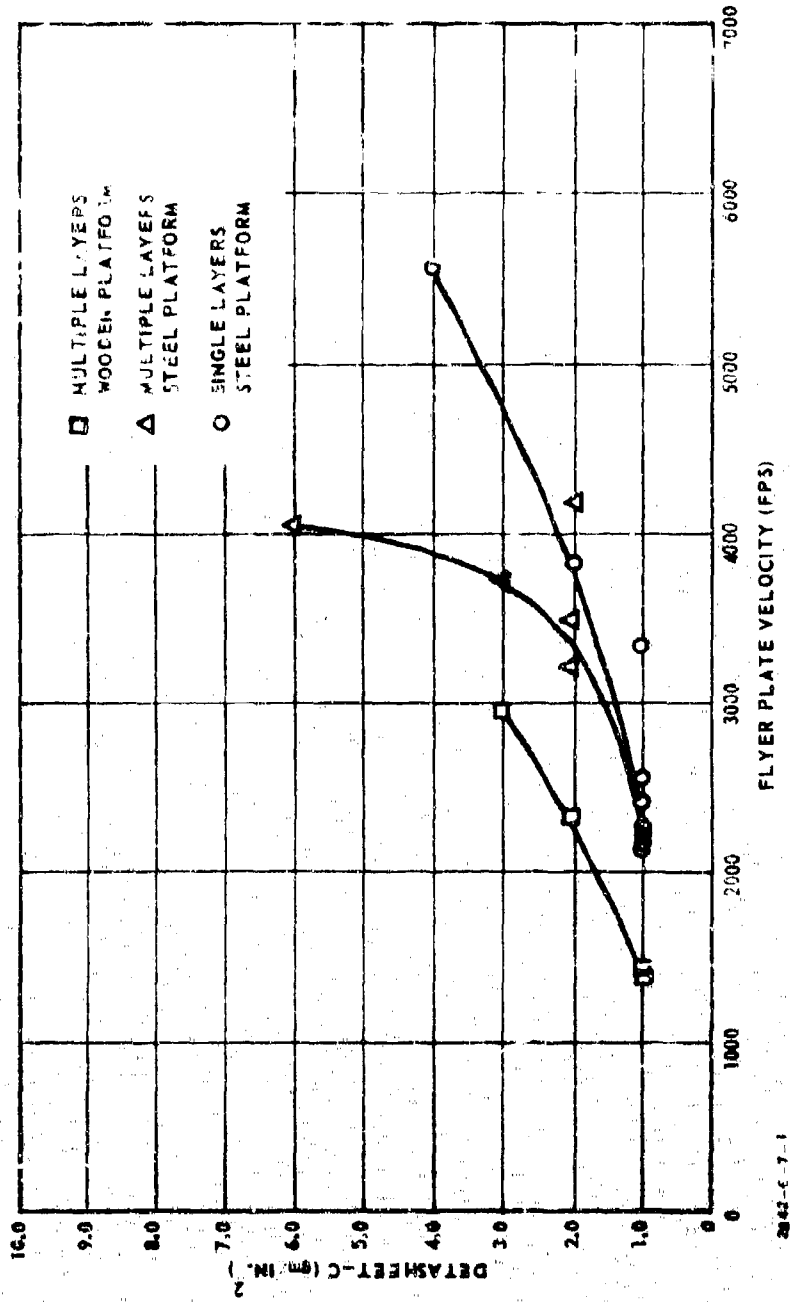


Figure IX-2. Flyer Plate Velocity vs Wt/Sq In. of Detonating Cord (Aluminum Flyer Plate 1/8 in. by 5 in.).

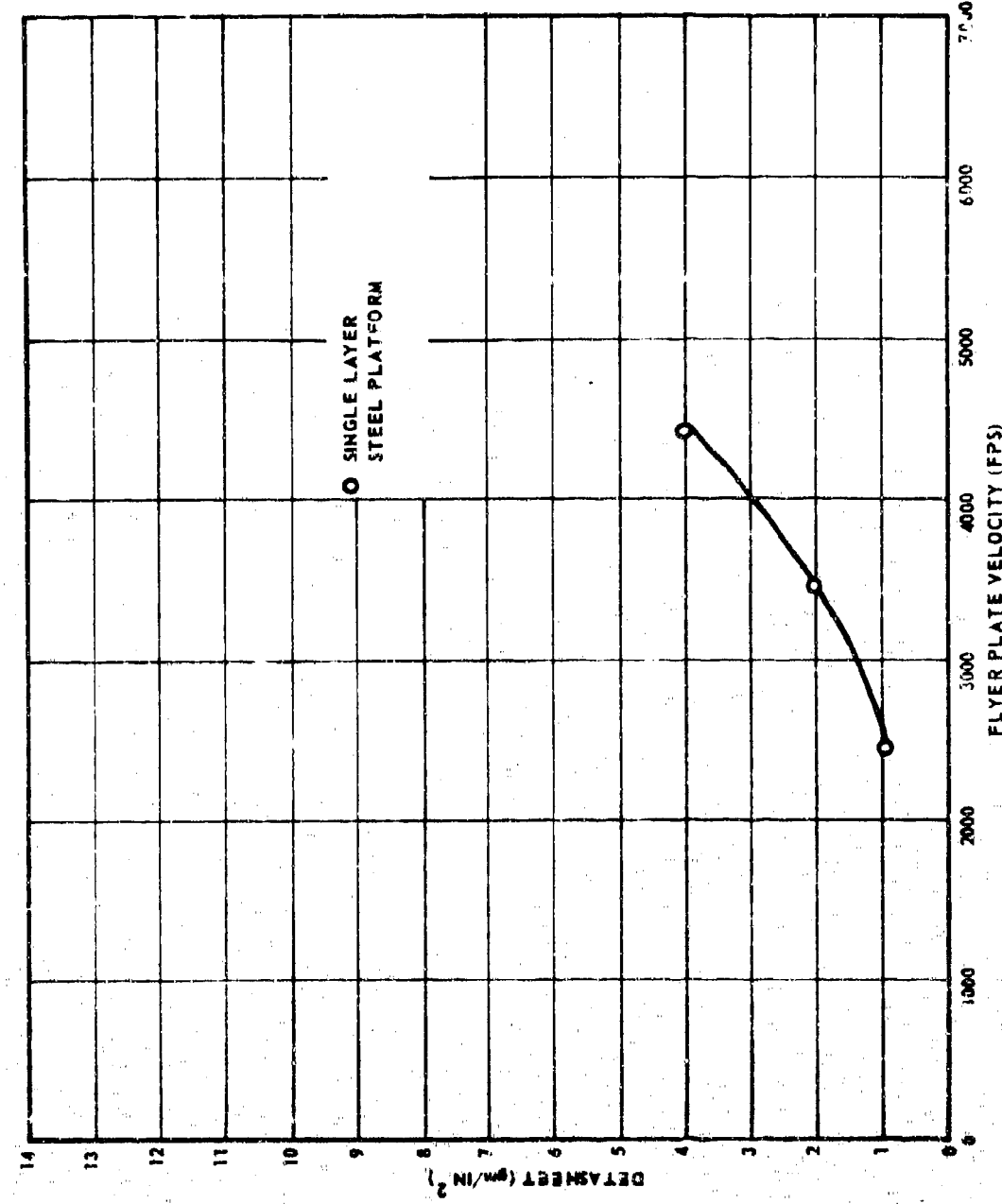


Figure IX-3. Flyer Plate Velocity vs Wt/Sq. In. of Detasheet-C.  
(Flyer Plate 3/16 in. by 5 in. by 5 in.)

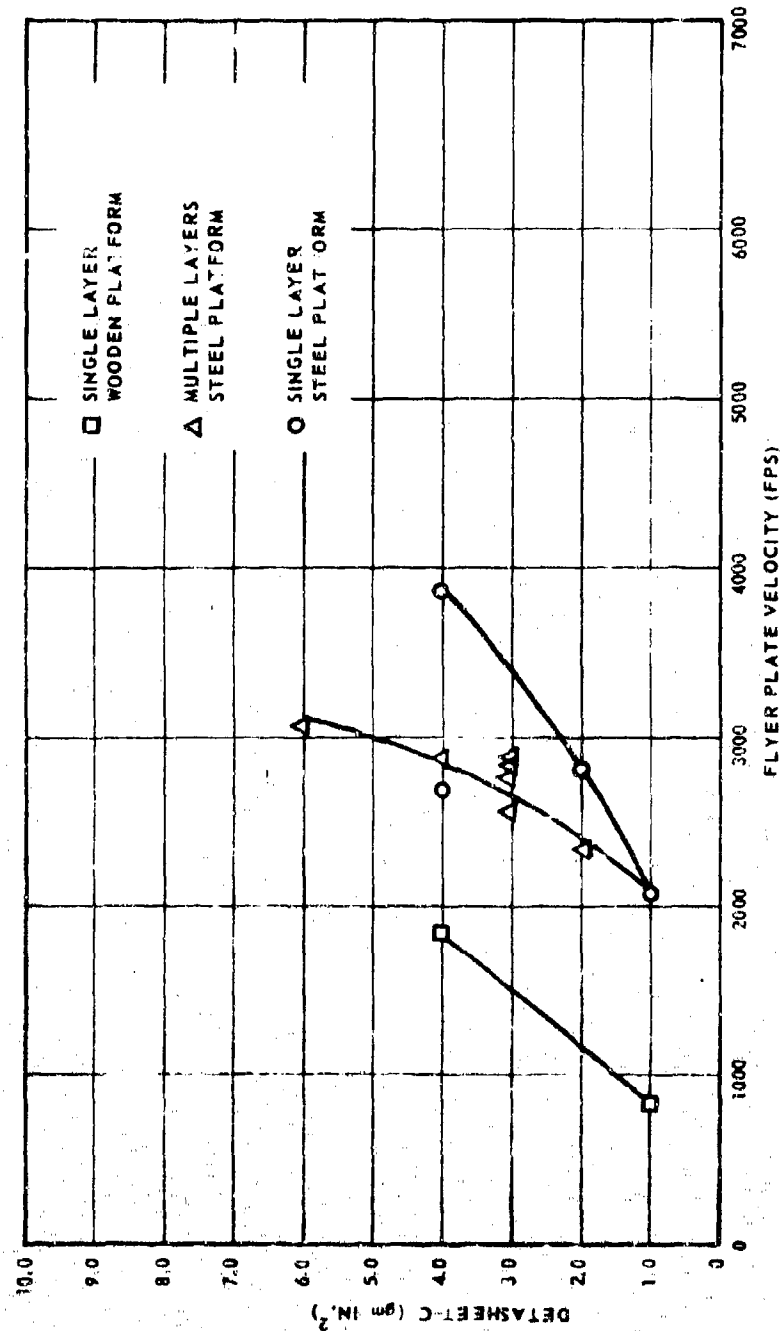


Figure IX-4. Flyer Plate Velocity vs Wt/Sq In. of Datasheet-C.  
(Aluminum Flyer Plate 0.250 in. by 5 in.)

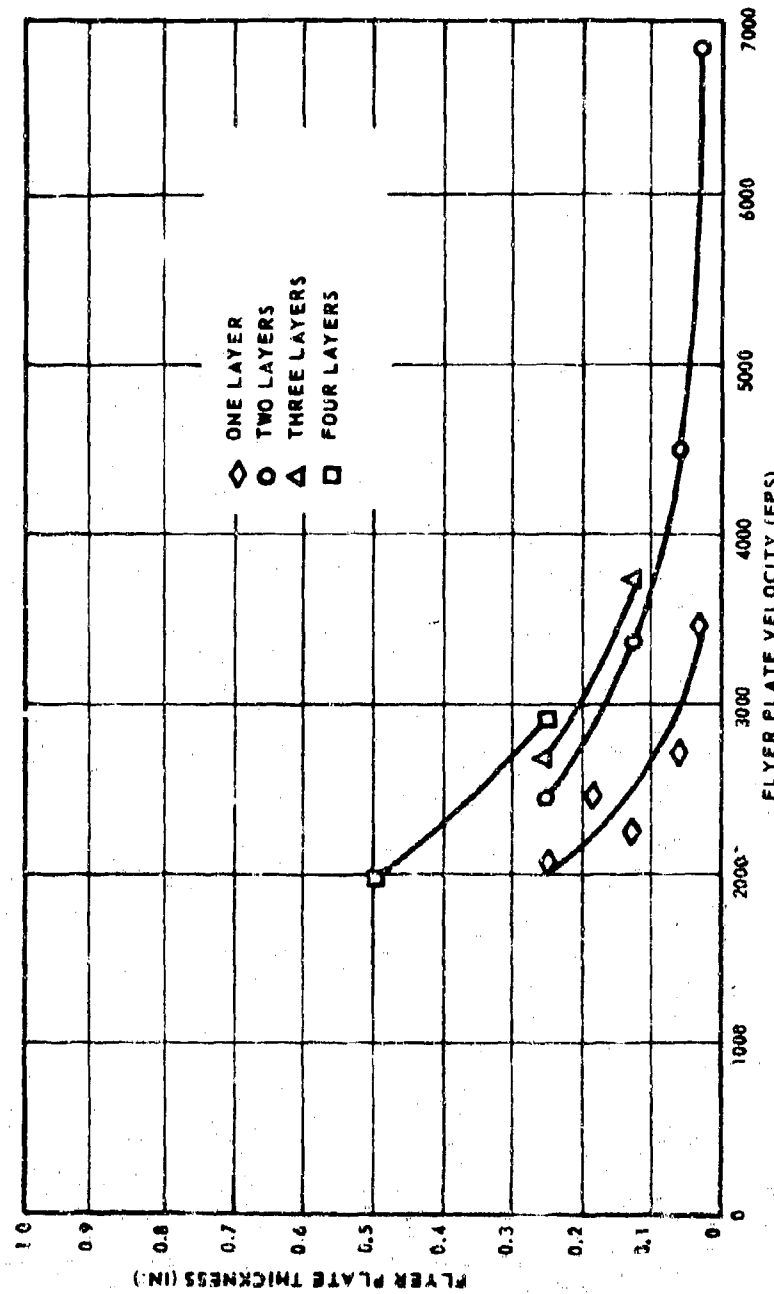


Figure IX-5. Flyer Plate Velocity vs Thickness of Flyer Plate.  
 (Test Materials: Aluminum Flyer Plate, Layers of Deta-  
 sheet C-1, and Steel Platform)

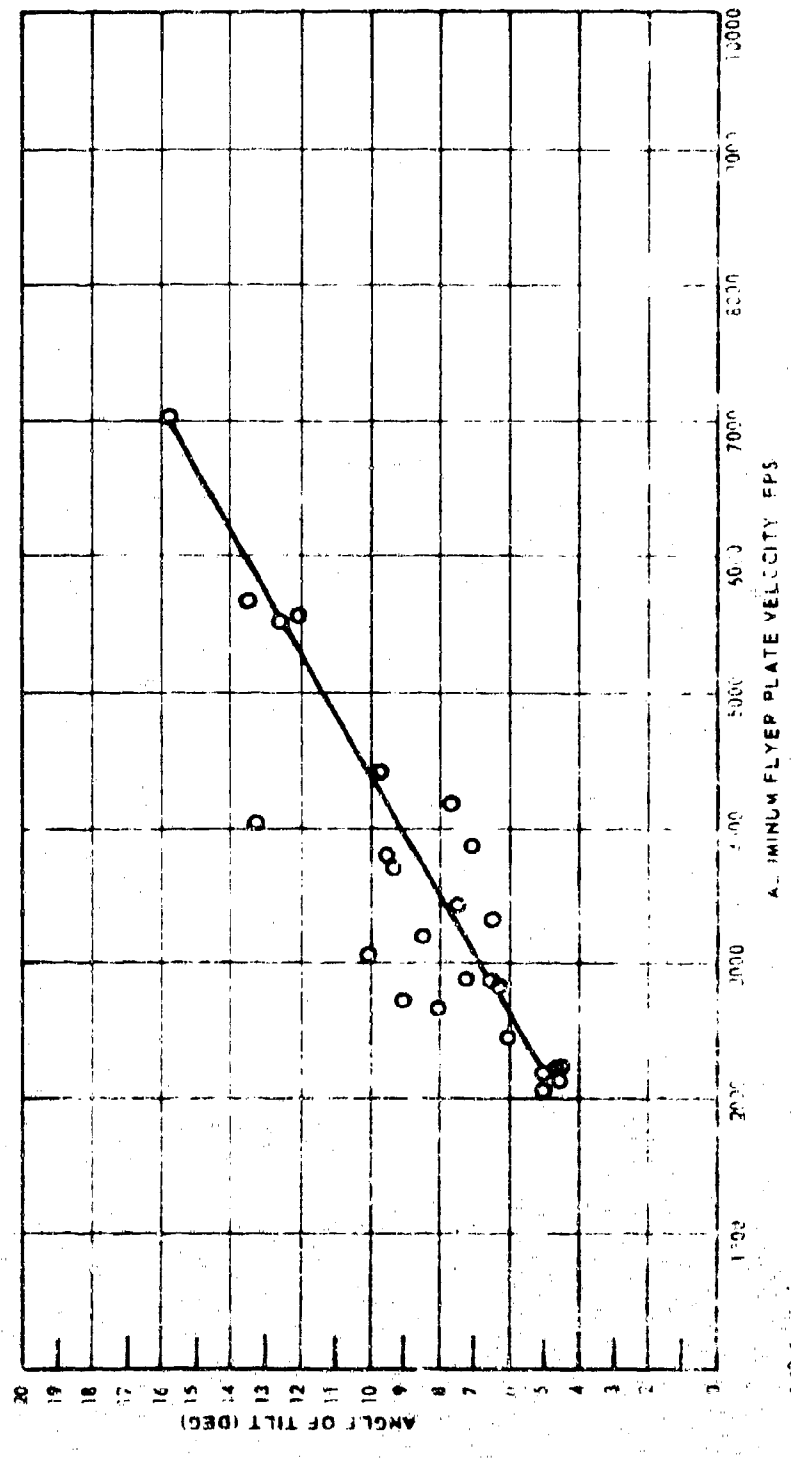


Figure IX-6. Angle of Tilt Required to Obtain Simultaneity of Impact at Target as a Function of the Aluminum Flyer Plate Velocity.

Table X-1. Peak Side-On Overpressure and Impulse.

Test No. 3.3.5.36  
 Propellant Composition AAB-3225  
 Propellant Size 7.15 in.  
 Propellant dia by 44.0 in. long  
 Booster Weight 24.0 lb  
 1.553 lb  
 796 lb  
 Test Site Temperature 63°  
 No Go

Range	35 ft	75 ft	105 ft	140 ft	160 ft	195 ft	250 ft	320 ft	375 ft	475 ft	500 ft	600 ft	700 ft
Instrumentation Loc (o'clock)	2	2	2	2	2	2	2	2	2	2	2	2	2
Measured Over- pressure (psi)						6.17		3.29					1.14
Computed Over- pressure (psi)*													
Sample-Contributed OP (psi)													
A. From Measured OP													
B. From Calculated OP													
Measured Impulse: (psi-sec.)													
Sample-Contributed Impulse (psi-sec.)													
64.3							34.2				16.9		*

\*Computed from shock velocity measurements using Rankine-Hugoniot equation.  
 \*\*Applicable data.

Table X-II. Peak Side-On Overpressure and Impulse.

Test No. 3.2.5-37  
 Propellant Composition AAB-3225  
 7.1% RDX  
 Propellant Size 24.0 in. dia by 43.5 in. long  
 Propellant Weight 1,555 lb  
 Booster Weight 796 lb  
 Test Site Temperature 52°F  
 Test Result Go

Range	35 ft	70 ft	100 ft	140 ft	160 ft	195 ft	250 ft	320 ft	375 ft	475 ft	600 ft	720 ft
Instrumentation Leg (o'-clock)	2	2	2	2	2	2	2	2	2	2	2	2
Measured Over-pressure (psi)	52.9	12.1				3.72				1.26		1.84
Computed Over-pressure (psi)	3.29	68.3	21.4		10.6	5.04		3.32	2.38	1.79		1.22
Sample-Contributed O <sub>2</sub> (psi)												
a. From Measured OP	44.4	10.5				3.30						
b. From Calculated OP	2.97	60.4	18.2		9.48	5.24		3.06	2.07	1.66		1.15
Measuring Impulse (ps.-sec.)								55.7			30.9	21.1
Sample-Contributed Impulse (psimsec.)								43.8			24.9	16.1

\* Computed from shock velocity measurements using Rankine-Hugoniot equation.

Table X-III. Peak Side-On Overpressure and Impulse.

Test No. 3.3.5.38  
 Propellant Composition AAB-3225  
 7.1% RDX  
 Propellant Size 24.0 in. dia by 48.0 in. long  
 Propellant Weight 1,553 lb  
 Booster Weight 796 lb  
 Test Site Temperature 57°  
 Test Result G<sub>c</sub>

Range	35 ft	70 ft	105 ft	140 ft	160 ft	195 ft	250 ft	320 ft	375 ft	435 ft	500 ft	600 ft	700 ft
Instrumentation Loc (o'clock)	2	2	2	2	2	2	2	2	2	2	2	2	2
Measured Over- pressure (psi)	36.5		10.7				4.12						
Computed Over- pressure (psi)*	393	65.1	17.8		10.1	6.45							
Sample-Distributed OP (psi)													
a. From Measured OP	366	26.9	8.95		6.9	5.68	3.66	2.96	1.77	1.36	1.28	1.28	0.75
b. From Calculated OP		57.1	14.4										
Measured Impulse (psi-sec)					109			56.0				31.1	21.5
Sample-Distributed Imp. ... (psi-sec)												25.3	17.3

\*Computed from shock velocity measurements using Rankine-Hugoniot equation.

Table X-IV. Peak Side-On Overpressure and Impulse.

Test No. 3.3.5.55  
 Propellant Composition AAB-3267  
 Propellant Size 5.0" RDX  
 Propellant Size 42.0 in. dia by 84.0 in. long  
 Propellant Weight 7,276 lb  
 Booster Weight 4,033 lb  
 Test Site Temperature 50°F  
 Test Result No Go

Range	70 ft	125 ft	180 ft	195 ft	250 ft	320 ft	375 ft	475 ft	500 ft	600 ft	700 ft	750 ft	850 ft	1000 ft
Instrumentation														
Long (5° slope)	2	2	2	2	2	2	2	2	2	2	2	2	2	2
Measured over-pressure (psi)														
Computed over-pressure (psi)														
161	147.8	14.0			6.43	3.99	2.95			1.77		1.42	1.19	
Sample-Distributed														
From Measured or True Calculated Or Sample (psi)														
110	140.0	11.0	6.41	5.54	3.26	2.52	2.23			1.41	1.30	1.18	0.98	0.79
Measured Impulse Impulse														
Sample-Distributed Impulse			229	147						83.4		56.4		39.3
					161	111				66.0		43.1		26.8

\*Compared from shock velocity measurements using Rankine-Hugoniot equation.

Table X-V. Peak Side-On Overpressure and Impulse.

Test No. 3.3.5.59  
 Propellant Composition AAB-3267  
 5.0% RDX  
 Propellant Size 42.0 in. dia by 84.0 in. long  
 Propellant Weight 7,276 lb  
 Booster Weight 4,023 lb  
 Test Site Temperature 50°F  
 Test Result Go

Range	70 ft	125 ft	140 ft	195 ft	250 ft	320 ft	375 ft	475 ft	500 ft	600 ft	700 ft	750 ft	850 ft	1000 ft
Instrumentation lag (o'clock)	2	2	2	2	2	2	2	2	2	2	2	2	2	2
Measured Over-pressure (psi)		35.6		10.6					3.33			1.85		1.04
Computed Over-pressure (psi)*	267	66.9	17.2		7.92	5.04	3.65			2.10		1.43	1.00	
Empirical-Contributed Over-pressure (psi)														
a. From Measured OP	246	55.9	29.5	14.5	9.10	7.12	4.42	3.28	2.49	1.81	1.64	1.29	0.71	0.39
b. From Calculated OP														
Measured Impulse (psi-sec)														
Empirical-Contributed Impulse (psi-sec)														
	273			153						80.6		71.5		49.1

\*Computed from shock velocity measurements using Rankine-Hugoniot equation.

Table X-VI. Peak Side-On Overpressure and Impulse.

Test No. 3-3-5-60  
 Propellant Composition AAB-3267 50% RDX  
 Propellant Size 42.0 in. dia by 84.0 in. long  
 Propellant Weight 7,276 lb  
 Booster Weight 4,023 lb  
 Test Site Temperature 50°F  
 Test Result Go

Rangle	70 ft	125 ft	140 ft	195 ft	250 ft	320 ft	375 ft	475 ft	500 ft	600 ft	700 ft	750 ft	850 ft	1000 ft
Instrumentation Lat (o'clock)	2	2	2	2	2	2	2	2	2	2	2	2	2	2
Measured Over- pressure (psi)*									3.16	1.95				1.25
Computed Over- pressure (psi)*	237	68.6		18.7		8.25	5.11	3.72		2.17		1.77	1.52	
Sample-Contributed Impulse (psi-sec)														
a. From Measured OP														
b. From Calculated OP	235	61.7	34.4	16.0	9.10	7.46	4.49	3.35	2.81	1.88	1.77	1.60	1.37	1.14
Measured Impulse (psi-sec)										97.0	80.0			5.19
Sample-Contributed Impulse (psi-sec)										81.1	69.4			43.9

\*Compared from shock velocity measurements using Rankine-Hugoniot equation.

**Table X-VII. Peak Side-On Overpressure and Impulse.**

Test No. CD-79  
 Propellant Composition AAB-3191 4.75% RDX  
 Propellant Size 11.0 in. dia by 44.0 in. long  
 Propellant Weight 278 lb  
 Booster Weight 75 lb  
 Test Site Temperature 59°F  
 Test Result No Go

Range	12.5 ft	20 ft	32.5 ft	40 ft	82.5 ft	90 ft	140 ft	145 ft	175 ft	250 ft
Instrumentation Loc (6' clock)	6	6	6	6	6	6	6	6	6	6
Measured Over- pressure (psi)				4.73			2.16			1.25
Computed Over- pressure (psi)*	613	252	91.5		11.8	3.14		3.35	0.89	
Sample-Contributed Op (psi)										
a. From Measured Op	572	233	84.9	4.29	11.0	7.47	1.73	3.63	+	1.11
b. From Calculated Op										
Measured Impulse (psi-sec)					11.0		18.8			17.8
Sample-Contributed Impulse (psi-sec)					99.2		14.0			15.5

\*Computed from shock velocity measurements using Rankine-Hugoniot equation.

\*Questionable data.

**Table X-VIII. Peak Side-On Overpressure and Impulse.**

Test No. 3D-3C  
 Propellant Composition AAB-3191 4.75% RDX  
 Propellant Size 12.5 in. dia by 45.0 in. long  
 Propellant Weight 361 lb  
 Booster Weight 106 lb  
 Test Site Temperature 76°F  
 Test Result Go

Range	12.5 ft	20 ft	32.5 ft	40 ft	82.5 ft	90 ft	140 ft	145 ft	195 ft	250 ft
Instrumentation Leg (o'clock)	6	6	6	6	6	6	6	6	6	6
Measured Over-pressure (psi)			53.6				3.5C			1.72
Computed Over-pressure (psi)*	904	374	140		16.5	11.3		6.04	2.22	
Sample-Contributed OP (psi)										
a. From Measured OP	864	353	132		52.7	15.6	11.0	3.10	5.79	2.01
b. From Calculated OP										1.59
Measured Impulse (psi-msec)					55.2			34.0		21.2
Sample-Contributed Impulse (psi-msec)					73.9			20.3		10.5

\*Computed from shock velocity measurements using Rankine-Hugoniot equation.

Table X-IX. Peak Side-On Overpressure and Impulse.

Test No. CD-81  
 Propellant Composition AAB-3198  
 3.4% RDX  
 Propellant Size 18.0 in. dia by 72.0 in. long  
 1.191 lb  
 Booster Weight 340 lb  
 Test Site Temperature 79°F  
 Test Result Co

Range	35 ft	70 ft	105 ft	140 ft	160 ft	195 ft	250 ft
Instrumentation Leg (o'clock)	10	10	10	10	10	10	10
Measured Over-pressure (psi)*	22.3			8.53			2.82
Computed Over-pressure (psi)*	269	60.3	18.9		9.46	5.33	
Sample-Contributed OP (psi)							
a. From Measured OP	254	17.6		7.74			
b. From Calculated OP	254	56.9	17.4		8.95	4.98	2.56
Measured Impulse (psi-msec)							
Sample-Contributed Impulse (psi-msec)	99.0			66.3			30.5

\*Computed from shock velocity measurements using Rankine-Hugoniot equation.

Table X-X. Peak Side-On Overpressure and Impulse.

Test No. CD-82  
 Propellant Composition AAB-3195  
 Propellant Size 2.9% RDX  
 24.0 in. dia by 96.0 in. long  
 Propellant Weight 2,749 lb  
 Booster Weight 795 lb  
 Test Site Temperature 69°F  
 Go

Range	35 ft	70 ft	105 ft	140 ft	160 ft	195 ft	250 ft	320 ft	375 ft	475 ft	500 ft	600 ft	700 ft
Instrumentation Leg (o'clock)	10	10	10	10	10	10	10	10	10	10	10	10	10
Measured Over-pressure (psi)*	44.3		13.9				4.56				1.75		1.11
Computed Over-pressure (psi)*	52.3	104	35.2		15.4	8.34				4.42	3.00	1.98	0.63
Sample-Contributed OP (psi)													
a. From Measured OP	35.8		12.4			4.13				1.63			1.06
b. From Calculated OP	96.9	32.4		14.4	7.65		4.21	2.83	1.76		0.19		
Measured Impulse (psi-nsec)		175		140			64.3				37.0		3.13
Sample-Contributed Impulse (psi-nsec)		133		124			53.5				31.5		*

\*Computed from shock velocity measurements using Rankine-Hugoniot equation.

\*Questionable data.

Table X-XI. Peak Side-On Overpressure and Impulse.

Test No.	CD-83
Propellant Composition	AAB-3198
Propellant Size	27.0 in. dia by 108.0 in. long
Propellant Weight	3,841 lb
Booster Weight	1,110 lb
Test Site Temperature	73°F
Test Result	Go

Computed from shock velocity measurements using Rankine-Hugoniot equation.

Table X-XI. Peak Side-On Overpressure and Impulse (Continued).

Test No. CD-B3  
 Propellant Composition AAB-3198  
 Propellant Size 3.4% RDX  
 27.0 in. dia by 108.0 in. long  
 Propellant Weight 3,841 lb  
 Booster Weight 1,110 lb  
 Test Site Temperature 73°F  
 Gc  
 Test Result

Range	35 ft	70 ft	105 ft	140 ft	160 ft	195 ft	250 ft	320 ft	375 ft	475 ft	500 ft	600 ft	700 ft
Instrumentation Leg (o'clock)													
Measured Over-pressure (psi)*	*	*	*	*	*	*	*	*	*	*	*	*	*
Computed Over-pressure (psi)*	568	14	55.1	*	*	*	*	*	4.07	*	4.30	*	0.98
Sample-Centribalized GIP (psi)													
a. From Measured OP	541	133	52.8	*	*	*	*	3.77	*	4.22	*	0.78	1.04
b. From Calculated OP													
Measured Impulse (psi-sec)	*	*	*	*	*	*	*	*	*	*	*	*	36.1
Sample-Centribalized Impulse (psi-sec)													31.6

\* Computed from shock velocity measurements using Rankine-Hugoniot equation,  
 questionable data.

\* No data.

Table X-XI. Peak Side-On Overpressure and Impulse (Concluded).

Test No. 3198  
 Propellant Composition AAB-3198  
 Propellant Size 3.45" x 2.8X  
 Propellant Weight 27.0 in. dia by 108.0 in. long  
 Booster Weight 3.841 lb  
 Test Site Temperature 1.110 lb  
 Test Result 73% Go

\*Computed from shock velocity measurements using Rankine-Hugoniot equation

Table X-XII. Peak Side-On Overpressure and Impulse.

Test No. 2D-84  
 Propellant Composition AA3-3178  
 Proj. Illant Size 3.05 in.  
 Propellant Weight 2,752 lb  
 Booster Weight 796 lb  
 Test Site Temperature 91°F  
 $G_0$   
 Test Result

Range	15 ft	70 ft	105 ft	140 ft	160 ft	195 ft	250 ft	320 ft	375 ft	475 ft	500 ft	600 ft	700 ft
Instrumentation Line (feet)	2	2	2	2	2	2	2	2	2	2	2	2	2
Measured Over- pressure (psi)*	*		15.1			3.38					1.59		1.01
Computed Over- pressure (psi)*	500	96.2	32.4		14.3	7.71			3.96	2.60	1.86		1.01
Side-Side-Distributed OP (psi)													
Side-Side-Distributed OP Measured OP vs. Side Calculated OP	6.79	89.5	23.6	13.6	10.3	7.03	2.87	3.74	2.42	1.75	1.47	C, Q,	C, Q,
Measured Impulse (psi-sec)									60.5		43.1		25.2
Side-Side-Distributed Impulse (psi-sec)								49.2			38.3		21.3

\*Computed from shock velocity measurements using Rankine-Hugoniot equation.

\*Questionable date.

Table X-XII. Peak Side-On Overpressure and Impulse (Continued).

Test No.	CD-84
Propellant Composition	AAB-3198
Propellant Size	3.4 <sup>2</sup> PRDX
Propellant Weight	24.0 in. dia by 96.0 in. long
Booster Weight	2.752 lb
Test Site	796.1b
Temperature	91.8° F
Test Result	6n

\*Computed from shock velocity measurements using Rankine-Hugoniot equation.

questionable data.

Table X-XII. Peak Side-On Overpressure and Impulse (Concluded).

Test No. CP-84  
 Propellant Composition AAB-3138  
 3.4% RDX  
 24.0 in. dia by 56.0 in. long  
 Propellant Size 2.752 lb  
 Booster Weight 796 lb  
 Test Site Temperature 91°F  
 G<sub>0</sub>  
 Test Result

Range	35 ft	70 ft	105 ft	140 ft	160 ft	195 ft	230 ft	320 ft	375 ft	425 ft	500 ft	600 ft	700 ft
Instrumentation													
1st (o'clock)	10	10	10	10	10	10	10	10	10	10	10	10	10
Measured Over-pressure (psi)													
12.5													
Computed Over-pressure (psi)*													
51.3	92.3	29.9			14.1	8.06							
Sample-Contributed OP (psi)													
a. From Measured OP													
b. From Calculated OP	494	85.4	27.0	10.9	13.1	7.39	2.98	3.78	2.37	1.85	1.77	1.16	1.06
Measured Impulse (psi-sec)													
+													
Sample-Contributed Impulse (psi-sec)													
+													

\* Computed from shock velocity measurements using Rankine-Hugoniot equation.

† Questionable data.

Table X-XIII. Peak Side-On Overpressure and Impulse.

Test No. CD-85  
 Propellant Composition AAB-3204  
 1.8% RDX  
 Propellant Size 24.0 in. dia by 96.0 in. long  
 Booster Weight 3,107 lb  
 Test Site Temperature 796 lb  
 63°F  
 Test Result No Go

Range	35 ft	70 ft	105 ft	140 ft	160 ft	195 ft	250 ft	320 ft	375 ft	475 ft	500 ft	600 ft	700 ft
Instrumentation Leg (o'clock)	2	2	2	2	2	2	2	2	2	2	2	2	2
Measured Over-pressure (psi)	+		11.6				2.94				5.35		
Computed Over-pressure (psi)*	516	80.3	23.6		12.3	7.55					1.23		
Sample-Contributed OP (psi)									3.88	2.55	1.94		
a. From Measured OP	495	73.1	20.5	9.93	11.3	6.85	2.37	3.66	2.37	1.83	5.31	1.17	
b. From Calculated OP													
Measured Impulse (psi-sec)	+			168			45.7				41.9	32.2	
Sample-Contributed Impulse (psi-sec)	+			153			32.1			37.1		26.8	

\*Computed from shock velocity measurements using Rankine-Hugoniot equation.

†Quotientable data.

Table X-XIII. Peak Side-On Overpressure and Impulse (Concluded).

Test No. CD-85  
 Propellant Composition AAB-3204 1.8% RDX  
 Propellant Size 24.0 in. dia by 96.0 in. Long  
 Propellant Weight 3,107 lb  
 Booster Weight 796 lb  
 Test Site Temperature 63°F  
 Test Result No go

Range	35 ft	70 ft	105 ft	140 ft	160 ft	195 ft	250 ft	320 ft	375 ft	475 ft	500 ft	600 ft	700 ft
Instrumentation Leg (o'clock)	10	10	10	10	10	10	10	10	10	10	10	10	10
Measured Over- pressure (psi)*	67.2		10.7										
Computed Over- pressure (psi)*	352	61.7	29.0		13.6	7.71			4.05	2.72	2.13		
Sample-Contributed OP (psi)													
B. From Measured OP C. From Calculated OP	323	59.5 74.5	26.1	8.99	12.6	7.03		3.84	2.55	2.03	1.65		.16
Measured Impulse (psi-msec)		310		166								39.2	30.5
Sample-Contributed Impulse (psi-msec)		230		151							34.1	27.0	

\*Computed from shock velocity measurements using Rankine-Hugoniot equation.  
 \*\*Questionable data.

Table X-XIV. Peak Side-On Overpressure and Impulse.

Test No.	Propellant Composition	AAB-3203
Propellant Size	2.4%	RDX
Propellant Weight	24 in.	dia by 96 in. long
Booster Weight	3,113 lb	
Test Site Temperature	796 lb	
Test Result	77% Ca	

Range	Instrumentation lag (o'clock)	35 ft	70 ft	105 ft	140 ft	160 ft	195 ft	250 ft	320 ft	375 ft	475 ft	500 ft	600 ft	700 ft
Measured Over- pressure (psi)	2	2	2	2	2	2	2	2	2	2	2	2	2	2
Computed Over- pressure (psi)	+	10.4					2.58					1.55		1.17
Sample-Contributed OF (psi)	649	90.9	30.9		13.4	7.05			3.54	2.27	1.65		0.93	
a. From Measured OF b. From Calculated OF	625	84.0	28.1	8.69	12.4	6.34	1.92		3.32	2.07	1.52	1.43	0.79	1.11
Measured Impulse (psi-msec)	+								40.3				38.0	26.3
Sample-Contributed Impulse (psi-msec)	+								25.4				32.8	23.3

Computed from shock velocity measurements using Rankine-Hugoniot equation.  
Spectrable data.

Table X-XIV. Peak Side-On Overpressure and Impulse (Continued).

Test No.		CD-86 2.4% RDX												
Propellant Composition AAB-3203		24 in. dia by 96 in. long												
Propellant Size		3.113 in. dia												
Propellant Weight		796 lb												
Booster Weight		770 lb												
Test Site Temperature		60°												
Test Result														
Range	Instrumentation Leg (o'clock)	35 ft	70 ft	105 ft	140 ft	160 ft	195 ft	250 ft	320 ft	375 ft	475 ft	500 ft	600 ft	720 ft
	Measured Over-pressure (psi)	6	6	5	6	6	6	6	6	6	6	6	6	6
	Computed Over-pressure (psi)*	90.2		11.1										
	Sample-Contributed OP (psi)	432	89.5	30.7		13.4	7.05							1.02
	a. From Measured OP													
	b. From Calculated OP	408	83.3	27.8	9.46									
	Measured Impulse (psi-msec)		82.6			12.3	6.36							
	Sample-Contributed Impulse (psi-msec)													
		254			102									
		221			82.2									
													25.7	

\*Computed from shock velocity measurements using Rankine-Hugoniot equation.  
\*\*Questionable data.

Table X-XIV. Peak Side-On Overpressure and Impulse (Concluded).

CD-86													
2.4% RDX													
24 in. dia by 96 in. long													
Propellant Composition AB-3203													
Propellant Size													
Propellant Weight													
Booster Weight													
Test Site Temperature													
Test Result													
G <sub>0</sub>													
Range	35 ft	70 ft	105 ft	140 ft	160 ft	195 ft	250 ft	320 ft	375 ft	475 ft	500 ft	600 ft	700 ft
Instrumentation													
Ring (o'clock)	10	10	10	10	10	10	10	10	10	10	10	10	10
Measured Grain- transverse (psi)	59.2	10.9				+					1.17		0.97
Calculated Grain- pressure (psi)*	48.5	93.7	31.5		13.6	7.16			3.54	2.23	1.66		0.99
Sample-Distributed OP (psi)													
a. From Measured OP	46.2	51.2 86.9	28.6	9.25	12.6	6.45	+	3.32	2.03	1.53	0.99	0.86	0.89
b. From Calculated OP													
Measured Impulse (psi-sec)		236		156			+				36.9	30.3	
Sample-Distributed Impulse (psi-sec)			201		140		+				31.7	26.8	

\*Computed from shock velocity measurements using Rankine-Hugoniot equation.  
†Questionable data.

Table X-XV. Peak Side-On Overpressure and Impulse.

Conducted measurements using Rankine-Hugoniot equation.

protestable date.

Table X-XV. Peak Side-On Overpressure and Impulse (Continued).

Computed from shock velocity measurements using Rankine-Hugoniot equation.

Questionable date.

Table X-XV. Peak Side-On Overpressure and Impulse (Concluded).

CD-88 0% RDX 44.0 in. dia by 115.0 in. long 9,240 lb 4,475 lb 93° F No Go									
Test No.	Composition ANB-2105								
	Propellant Size	Propellant Weight	Booster Weight	Test Site Temperature	Test Result				
Range	35 ft	70 ft	105 ft	140 ft	160 ft	195 ft	250 ft	320 ft	375 ft
Instrumentation deg (o'clock)	10	10	10	10	10	10	10	10	10
Measured Over- pressure (psi)*	+	+	+	+	+	+	+	+	+
Computed Over- pressure (psi)*	762	236	108	3.77	20.5		8.90	5.55	3.97
Sample-Contributed $\Delta P$ (psi)									
a. From Measured OP	674	211	97.1	†	33.4	17.7	†	8.67	4.92
b. From Calculated OP									
Measured Impulse (psi-sec)									
Sample-Contributed Impulse (psi-sec)									

\*Computed from shock velocity measurements using Rankine-Hugoniot equation.

†Questionable data.

Table X-XVI. Peak Side-On Overpressure and Impulse.

		CD-39													
		Propellant Composition AP-3205					0.75% RDX								
		Propellant Size		48 in. dia by 152 in. long			21.825 lb			5.875 lb					
		Booster Weight			96.0 <sup>a</sup>			Gc			Gc				
		Test Site Temperature													
		Test Result													
Range		70 ft	125 ft	140 ft	195 ft	250 ft	320 ft	375 ft	475 ft	500 ft	600 ft	700 ft	750 ft	850 ft	1000 ft
Instrumentation															
Lag (o'clock)		2	2	2	2	2	2	2	2	2	2	2	2	2	2
Measured Over-pressure (psi)															
Computed Over-pressure (psi)*		116		16.4											
Sample-Contributed OP (psi)															
From Measured OP															
From Calculated OP															
Measured Impulse (psi-sec)															
Sample-Contributed Impulse (psi-sec)															

\* Computed from shock velocity measurements using Rankine-Hugoniot equation.

<sup>a</sup> Questionable data.

\*\* No date.

Table X-XVI. Peak Side-On Overpressure and Impulse (Continued).

Test No. Composition AAB-3205  
 Propellant Size 48 in. dia by 192 in. long  
 Propellant Weight 21,829 lb  
 Booster Weight 5,875 lb  
 Test Site Temperature 96°F  
 Go

Rang:	70 ft	125 ft	140 ft	195 ft	250 ft	320 ft	375 ft	475 ft	500 ft	600 ft	700 ft	750 ft	800 ft	1,120 ft
Instrumentation Lat. (0 C clock)	6	6	6	6	6	6	6	6	6	6	6	6	6	6
Measur. Pressure (psi)	*				16.9					*				
Calculated Over- pressure (psi)*	47.0	123	39.3	*	*		6.10							
Sample-Contributed OP (psi)														
a. From Measured OP b. From Calculated OP	44.7	115	*	36.0	15.0	*	*	5.70	**	*	**	**	2.25	2.25
Measured Impulse (psi-sec)														
Sample-Contributed Impulse (psi-sec)														

\* Computed from shock velocity measurements using Rankine-Hugoniot equation.

\*\* Questionable data.

\*\*\* No data.

Table X-XVI. Peak Side-On Overpressure and Impulse (Concluded).

		CD-69													
		CD-89													
		0.73% RDX													
		4.5 in. dia by 132 in. long													
		21,829 lb													
		5,175 lb													
		96°F													
		G <sub>0</sub>													
Test No.		AAU-3205													
Propellant Composition		0.73% RDX													
Propellant Size		4.5 in. dia by 132 in. long													
Propellant Weight		21,829 lb													
Booster Weight		5,175 lb													
Test Site Temperature		96°F													
Test Result		G <sub>0</sub>													
Range	Instrumentation	70 ft	125 ft	140 ft	145 ft	250 ft	320 ft	375 ft	475 ft	500 ft	600 ft	700 ft	750 ft	850 ft	1,050 ft
Instrumentation	Log (1/2-clock)	10	10	10	10	10	10	10	10	10	10	10	10	10	
Measured Over-pressure (psi)		108			17.7										
Computed Over-pressure (psi)		48.2	14.2	49.4		14.8	7.83	5.69		3.40		2.44	1.84		
Sample-Contributed OP (psi)															
a. From Measured OP		460	134	132	46.4	15.8	13.9	7.09	5.28	*	3.12	3.16	2.26	1.57	
b. From Calculated OP															
Measured Impulse (psi-sec)										*		133			
Sample-Contributed Impulse (psi-sec)										*		121			
												92.5			

\* Computed from shock velocity measurements using Rankine-Hugoniot equation.

#Q testable date.

\*\*No data.

Table X-XVII. Peak Side-On Overpressure and Impulse.

CD-9C 0.5% RX									
Test No. 3213 Propellant Composition AAB-3213 Propellant Size 46.0 in. dia by 192.0 in. long									
Propellant Weight 21,959 lb Booster Weight 5,187.16 Test Site Temperature 98° G <sub>0</sub> Test Result									
Range	70 ft	125 ft	140 ft	195 ft	250 ft	320 ft	375 ft	475 ft	500 ft
Instrumentation									
Lag (o'clock)	2	2	2	2	2	2	2	2	2
Measured Over-pressure (psi)*									
Computed Over-pressure (psi)*	125		15.7				4.11	3.28	3.28
Sample-Contributed OP (psi)									
a. From Measured OP	420	122	41.1		14.8	8.75	6.20	3.53	2.58
b. From Calculated OP									
Measured Impulse									
Sample-Contributed Impulse (psi-sec)									
Impulse (psi-sec)	396	114	38.0	13.8	13.9	8.05	5.80	3.63	3.11
								3.26	2.40
								1.80	1.63
								1.30	1.10
								1.19	1.05

\* Computed from shock velocity measurements using Rankine-Hugoniot equation.

\*\* No data.

Table X-XVII. Peak Side-On Overpressure and Impulse (Continued).

Test No.	CD-90
Propellant Composition	AAB-3213
Propellant Size	0.5% RDX
Propellant Weight	48.0 in. dia by 192.0 in. long
Booster Weight	21,959 lb
Booster Weight	5,875 lb
Test Site Temperature	98°F
Test Result	Gc

Computed from shock velocity measurements using Parkin-Hanriot equation.

\* Quasi-locatable data.

THE DRAFT.

Table X-XVII. Peak Side-On Overpressure and Impulse (Concluded).

Test No. GD-90									
Propellant Composition AAB-3213 0.5% RDX									
Propellant Size 48.0 in. dia by 192.0 in. long									
Propellant Weight 21,950 lb									
Booster Weight 5,875 lb									
Test Site Temperature 98°F									
Test Result G <sub>o</sub>									
Range	70 ft	125 ft	140 ft	155 ft	250 ft	320 ft	375 ft	475 ft	500 ft
Instrumentation	10	10	10	10	10	10	10	10	10
Leg (o'clock)	10	10	10	10	10	10	10	10	10
Measured Over-pressure (psi)*	88.4			23.1				7.73	3.78
Computed Over-pressure (psi)*	555	127		37.6		14.8	9.18	6.61	
Sample-Contributed OP (psi)								3.93	2.98
a. From Measured OP	536	119	81.8	34.4	11.0	13.9	8.5C	6.23	
b. From Calculated OP								7.42	
Measured Impulse (psi-sec)								3.68	3.11
Sample-Contributed Impulse (psi-sec)								245	125
									53.5
								233	113
									74.8

\* Computed from shock velocity measurements using Rankine-Hugoniot equation.

\*\* No data.

Table X-XVIII. Peak Side-On Overpressure and Impulse.

Computed from shock velocity measurements using Rankine-Hugoniot equation.

Questionable data.  
No data.

Table X-XVIII. Peak Side-On Overpressure and Impulse (Continued).

Range	Instrumentation Leg (o'clock)									
	70 ft	125 ft	140 ft	195 ft	250 ft	320 ft	375 ft	475 ft	520 ft	500 ft
Measured Over-pressure (psi)	6	6	6	6	6	6	6	6	6	6
Computed Over-pressure (psi)					1.16					C.38
Sample-Contributed OP (psi)	**	9.29	**	**	**	*	0.95	**	**	0.64
a. From Measured OP	**	9.55	**	1.00	**	*	0.92	**	0.35	**
b. From Calculated OP									0.63	0.27
Measured Impulse (psi-sec)						1.09		**	4.33	2.94
Sample-Contributed Impulse (psi-sec)						6.02		**	3.36	2.23

\* Computed from shock velocity measurements using Rankine-Hugoniot equation.

\*\* Questionable data.

\*\*\* No data.

Table X-XVIII. Peak Side-On Overpressure and Impulse (Concluded).

		CD-91													
		1.75% RDX													
		11 in. dia by 44 in. long													
		278 lb													
		75 lb													
		91°F													
		No Go													
Range	Instrumentation Line (for clock)	70 ft	125 ft	140 ft	195 ft	250 ft	320 ft	375 ft	475 ft	500 ft	600 ft	700 ft	750 ft	850 ft	1000 ft
Measured Over- pressure (psi)		10	10	10	10	10	10	10	10	10	10	10	10	10	10
Computed Over- pressure (psi)*			2.52		1.19				0.49		0.35			0.20	
Sample-Contributed OP (psi)															
a. From Measured OP	15.8	8.01	2.16	1.19	1.04	0.73	0.46	0.33	0.42	0.10	0.31	0.11	0.09	0.18	
b. From Calculated OP															
Measured Impulse (psi-sec)				19.7		13.6				6.34		4.91		2.61	
Sample-Contributed Impulse (psi-sec)					15.2	11.3				5.05		4.01		1.84	

\* Computed from shock velocity measurements using Rankine-Hugoniot equation.

Table X-IX. Peak Side-On Overpressure and Impulse.

Test No. CD-92  
 Propellant Composition AAB-3215  
 0.25% RDX  
 Propellant Size 48.0 in. dia by 192.0 in. leng  
 21,971 lb  
 Propellant Weight 5,875 lb  
 Test Site Temperature 99°F  
 Test No Go

Range	70 ft	ft	ft	25	ft	320	ft	375	ft	475	ft	500	ft	600	ft	700	ft	750	ft	850	ft	1000	ft
In. Minimization Leg (Clock)	2		2		2		2		2		2		2		2		2		2		2		2
Measured Over-pressure (psf)*				23.5							3.72						-4.9						1.50
Calculated Over-pressure (psf)*	325	103	35.8	1		13.2		7.73		5.46		5.46											
Sample-Contributed Imp (ips)																							
a. From Measured Up	2.96	44.6	32.6		.1.8		.1.2		6.99		3.06		7.55		.6		2.26		2.03		1.51		1.36
b. From Calculated Up																							
Sample-Contributed Impulse (psi-sec)																							77.6
Sample-Contributed Impulse (psi-sec)																							68.3
Sample-Contributed Impulse (psi-sec)																							

\* Remained from shock velocity measurements using Klemm-Burg for equation.

\* No data.

Table X-XIX. Peak Side-On Overpressure and Impulse (Continued).

Test No. CD-92  
 Propellant Composition AAB-921S  
 Propellant Size 48.0 in. dia by 192.0 in. long  
 Propellant Weight 21,971 lb  
 Booster Weight 5,875 lb  
 Test Site Temperature 99°F  
 Test Result Nc Go

Range	70 ft	125 ft	195 ft	250 ft	320 ft	375 ft	475 ft	500 ft	600 ft	700 ft	750 ft	850 ft	1000 ft
Instrumentation Leg (o'clock)	6	6	6	6	6	6	6	6	6	6	6	6	6
Measured Over-pressure (psi)*													
Computed Over-pressure (psi)*	34.7	95.9	29.8		11.5	6.78	4.59		4.59		2.90	**	
Sample-Contributed Imp (psi)													
A. Prod Measured O.P.	31.9	86.8	26.4	16.1	10.5	6.00	4.12	2.33	4.12	**	0.91	1.29	
B. Prod Calculated O.P.													
Measured Impulse (psi-sec)					298				1444		**		66.9
Sample-Contributed Impulse (psi-sec)					264				125	**		60.2	

\* Computed from shock velocity measurements using Rankine-Hugoniot equation.

\*\* No data.

Table X-XIX. Peak Side-On Overpressure and Impulse (Concluded).

Range	Instrumentation tag (o'clock)	Test No. 3215										
		70 ft	125 ft	195 ft	250 ft	325 ft	375 ft	475 ft	500 ft	700 ft	750 ft	850 ft
10	10	10	10	10	10	10	10	10	10	10	10	10
Measured Over- pressure (psi)	**											
Computed Over- pressure (psi)*	372	166	34.0		14.6	9.38	6.62			2.65		1.86
Impulse-Contributed Imp (psi)												
From Measured OP From Calculated OP	323	97.5	31.4	**	13.6	8.70	6.24	2.82	6.24	2.44	2.96	1.75
Measured Impulse (psi-msec)				**				**		103		77.7
Impulse-Contributed Impulse (psi-msec)				**				**		39.5		68.4

\* Computed from shock velocity measurements using Rankine-Hugoniot equation.

\*\* No data.

Table X-XX. Peak Side-On Overpressure and Impulse.

Test No. CD-93  
 Propellant Composition ABU-3192  
 Propellant Size 6.07 lbX  
 1.5 in. dia by 52 in. long  
 Propellant Weight 435 lb  
 Booster Weight 145 lb  
 Test Site Temperature 92°F  
 Test Result Go

Range	75 ft	125 ft	140 ft	155 ft	210 ft	320 ft	375 ft	475 ft	500 ft	600 ft	700 ft	750 ft	850 ft	1000 ft
Instrumentation Set (Clock)	2	2	2	2	2	2	2	2	2	2	2	2	2	2
Measured Over- pressure (psi)	5.08		1.84					0.53		0.42				0.35
Computed Over- pressure (psi)*	4C.C	16.3	3.55		1.36	0.71	0.58		0.42		0.26			
Sample-Contributed														
True Measured OP at 1.5 in. from Calculated OP (psi)	36.3	15.9	4.66	3.33	1.68	1.41	0.52	0.46	0.41	0.33	0.39	0.17	0.33	
Measured Impulse (lb-sec)			++		22.1				11.4		9.05		7.65	
Sample-Contributed Impulse (lb-sec)			++		18.6				9.56		7.52		6.86	

\* Computed from shock velocity sensor elements using Rankine-Hugoniot equation.

\*\* Quasi-stationary data.

+ No data.

Table X-XX. Peak Side-On Overpressure & Impulse Computation

Test No. 10  
Proper Liquid Composition AAE-3-92  
Proper Liquid Size 1/2 in.  
Proper Weight 43.6 lb  
Proper Weight 43.6 lb  
Test Size Temperature  
Test Result 60° F

Range	T (ft)	Et (ft)	225 ft	140 ft	125 ft	250 ft	321 ft	275 ft	212 ft	207 ft	175 ft	170 ft	165 ft	160 ft	155 ft	150 ft	145 ft	140 ft	135 ft	130 ft	
Instrumentation Level (feet above measured over-	E	0	6	6	6	6	6	6	6	6	6	6	6	6	6	6	6	6	6	6	
Measured Over- pressure (psi)			4.1*			1.42															
Computed Over- pressure (psi), Sample-Contributed OP (psi)	21.8	12.1		2.47			1.37				6.32		6.32		6.32						
a. From Measure' OP b. From Gairland'd OP																					
Measured Impulse (psi-sec.)																					
Sample-Contributed Impulse (psi-sec.)																					

\* Computed from shock velocity measurements using Rankine-Hugoniot equation.

+ Questionable data.

Table X-XX. Peak Side-On Overpressure and Impulse (Concluded).

Test No. Propellant Composition AAB-3192 Propellant Size Propellant Weight Booster Weight Test Site Temperature Test Result:									
Range	70 ft	125 ft	141 ft	195 ft	250 ft	320 ft	375 ft	475 ft	500 ft
Instrumentation Loc (o'clock)	10	10	10	10	10	10	10	10	10
Measured Over- pressure (psi)*									
Computed Over- pressure (psi)*	5.1	5.1	2.36						
Sample-Contributed Op (psi)	31.6	14.1	3.01	1.68	1.14	0.90	0.60	0.40	0.20
a. From Measured Op	29.6	13.7	5.1	2.79	2.23	1.60	1.05	0.80	0.54
b. From Calculated Op									0.55
Measured Impulse (psi-sec)			**				10.7	9.65	5.44
Sample-Contributed Impulse (psi-sec)			**				8.86	8.49	5.32

\* Computed from shock velocity measurements using Rankine-Hugoniot equation.

\*\* No data.

Table X-XXI. Peak Side-On Overpressure and Impulse.

Test No. CG-55  
 Propellant Composition ANB-3226  
 Propellant Size 72.0 mm dia by 268.0 in. long  
 Propellant Weight 74.0 lb  
 Booster Weight 16.0 lb  
 Test Site Temperature 81°F  
 Test Result 20

Range	125 ft	250 ft	375 ft	475 ft	500 ft	600 ft	700 ft	750 ft	850 ft	1000 ft	1100 ft	1200 ft	1300 ft	1400 ft
Instrumentation Leg (or lock)	2	2	2	2	2	2	2	2	2	2	2	2	2	2
Measured Over-pressure (psi)*	56.2			10.3										
Computed over-pressure (psi)*	257	61.7	20.2	13.1		6.36		4.73	3.46		2.44		2.22	
Sample-Contributed OP (psi)														
a. From Measured OP	239	52.1	13.6	12.2	9.4	6.28	5.56	4.25	3.15	3.25	2.22	2.02	1.87	
b. From Calculated OP		51.7												
Measured Impulse (psi-sec)	572				342	256								
Sample-Contributed Impulse (psi-sec)	457				306	231								

\* Computed from shock velocity measurements using Rankine-Hugoniot relation.

Table X-XXI. Pe<sub>2</sub> Side-On Overpressure and Impulse (Continued).

Test No. 3226  
 Propellant Composition ANB-3226  
 2. Propellant Size  
 a. Propellant Weight  
 b. Carter Weight  
 c. Site Temperature  
 d. Site Pressure  
 e. Result  
 Go

Range	125 ft	250 ft	375 ft	475 ft	500 ft	600 ft	700 ft	750 ft	850 ft	1000 ft	1100 ft	1150 ft
Instrumentation												
Lag (o'clock)	6	6	5	6	6	6	6	6	6	6	6	6
Measured Over-pressure (psi)	51.4			**								
Computed Over-pressure (psi)*	246	60.4	19.9	12.9	5.77			4.74	3.54	2.56	2.25	
Sample-Contributed Or (psi)												
4. True Measured OP	47.2			**								
5. True Calculated OP	228	56.3	18.2	12.0	5.18			4.17	3.25	2.22	1.95	
Measured Impulse (psi-sec)	470			**						311		
Sample-Contributed Impulse (psi-sec)	351			**						194		

\* Computed from shock velocity measurement using Rankine-Hugoniot equation.  
 \*\* No data.

Table X-XXI. Peak Side-On Overpressure and Impulse (Concluded).

Test No. 2E-95  
 Propellant Composition AN-11225  
 0% SDX  
 Propellant Size 72.35<sup>a</sup> dia by 268.0 in. long  
 Propellant Weight 74.30<sup>b</sup> lb  
 Booster Weight 18.15<sup>c</sup>  
 Test Site Temperature 31.2<sup>d</sup> F  
 Test Result Go

Range	125 ft	250 ft	375 ft	475 ft	500 ft	600 ft	700 ft	750 ft	850 ft	1000 ft	1100 ft	1200 ft	1300 ft	1400 ft
Instrumentation Line (o'clock)	10	10	10	10	10	10	10	10	10	10	10	10	10	10
measured over- pressure (psi)*														
Computed Over- pressure (psi)*	50.6		*					5.75						
Shock-Contributed dp (psi)														
a. From Measured dp	43.8													
b. From Calculated dp	55.6	19.0	11.7					5.35						
Measured Impulse (psi-sec)								5.60	3.38	2.82	3.34	2.85	2.73	
Shock-Contributed Impulse (psi-sec)		**						**	254		257			
									207		137			

\* Computed from shock velocity measurements using Rankine-Hugoniot equation.

† Questionable data.

\*\* No data.

Table X-XXXII. Peak Side-On Overpressure and Impulse.

		CD-33					
		OS BX					
		60 ft	41.2 ft	24.0 in. long			
Propellant Composition		ANB-3226					
Propellant Size		42.5 in.					
Propellant Weight		15.00 lb					
Booster Weight		1.35 lb					
Test Site Temperature		10.3°F					
Test Result		No GC					
Range	7) Ft	125 ft	250 ft	320 ft	475 ft	500 ft	600 ft
Instrumentation Set (Clockwise)							
2	2	2	2	2	2	2	2
Measured Over-pressure (psi)*		133	32.9		6.49		1.15
Computed Over-pressure (psi)*		35.5					
Sample-Contributed Δε (psi)							
a. From Measured Δε							
b. From Calculated Δε							
Measured Impulse (psi-sec)							
Sample-Contributed Impulse (psi-sec)							

\* Computed from shock velocity measurements using Rankine-Hugoniot equation.

\* Questionable data.

+ No data.

Table X-XXII. Peak Side-On Overpressure and Impulse (Continued).

Test No.		CD-98																				
		C4 RDX																				
		dia by 240 in. long																				
Propellant Composition AAB-3226		44,900 15																				
Propellant Size		10,700 15																				
Propellant Weight		1030F																				
Booster Weight		No. 30																				
Test Site Temperature																						
Test Result																						
Range	70 ft	125 ft	180 ft	240 ft	300 ft	475 ft	500 ft	600 ft	700 ft	730 ft	850 ft	1000 ft	1030 ft	1050 ft	1070 ft	1090 ft	1110 ft	1130 ft	1150 ft	1170 ft	1190 ft	
Instrumentation																						
Lag (o'clock)	6	6	6	6	6	6	6	6	6	6	6	6	6	6	6	6	6	6	6	6	6	
Measured Over-pressure (psi)*																						
Computed Over-pressure (psi)*																						
Stampie-Contributed CP (psi)																						
a. From Measured CP																						
b. From Calculated CP																						
Measured Impulse (psi-sec)																						
Stampie-Contributed Impulse (psi-sec)																						

\* Computed from shock velocity measurements using Rankine-Hugoniot equations.

+ Quotientable data.

Table X-XXII. Peak Side-On Overpressure and Impulse (Concluded).

Test No. CD-98  
 Propellant Composition ANB-3226  
 Propellant Size 60 in. dia by 240 in. long  
 Propellant Weight 42,800 lb  
 Boated Weight 10,700 lb  
 Test Site Temperature 103°F  
 Test Result No Go

Range	70 ft	125 ft	140 ft	250 ft	320 ft	475 ft	500 ft	600 ft	700 ft	750 ft	850 ft	1000 ft	1250 ft	1500 ft
Instrumentation Leg (o'clock)														
Measured Over-pressure (psi)														
Computed Over-pressure (psi)*														
Sample-Contributed CP (psi)														
a. From Measured OP														
b. From Calculated OP														
Measured Impulse (psi-sec)														
Sample-Contributed Impulse (psi-sec)														

\* Computed from shock velocity measurements using Rankine-Hugoniot equation.  
 † Quantifiable data.  
 \*\* No data.

This Document Contains Missing  
 Page/s That Are Unavailable In  
 The Original Document

This Document  
Reproduced From  
Best Available Copy

UNCLASSIFIED

Security Classification

DOCUMENT CONTROL DATA - R&D		
(Security classification of title, body of abstract and indexing annotation must be entered when the overall report is classified)		
1 ORIGINATING ACTIVITY (Corporate author) Aerojet-General Corporation 11711 Woodruff Avenue Downey, California 90241		2a REPORT SECURITY CLASSIFICATION Unclassified
3 REPORT TITLE  PROJECT SOPHY - SOLID PROPELLANT HAZARDS PROGRAM		2b GROUP N/A
4 DESCRIPTIVE NOTES (Type of report and inclusive dates) Final Report covering the period from 1 September 1965 through		
5 AUTHOR(S) (Last name, first name, initial) Elwell, Robert B. Irwin, Owen R. Vail, Jr., Richard W.		17 May 1967
6 REPORT DATE August 1967		7a TOTAL NO OF PAGES 266 pp (Vol I), 152 pp (Vol II)
7c CONTRACT OR GRANT NO AF04(611)-10919		7d NO OF REFS 50
8a PROJECT NO. 63A00201		8b ORIGINATOR'S REPORT NUMBER(S) 0977-01(01)FP
9d OTHER REPORT NO(S) (Any other numbers that may be assigned this report) AFRPL-TR-67-211 (Two Volumes)		
10 AVAILABILITY/LIMITATION NOTICES  Qualified requestors may obtain copies of this report from DDC.		
11 SUPPLEMENTARY NOTES None		12 SPONSORING MILITARY ACTIVITY Air Force Rocket Propulsion Laboratory Hazards Analysis Branch Air Force Systems Command, Edwards AFB Edwards, California 93523
13 ABSTRACT  The critical diameter of a typical composite propellant was determined to be between 60 and 72 in. The selection of test sample sizes was facilitated by the detonation model developed during the solid propellant hazards program, under Contracts AF04(611)9945 and AF04(611)10919. The final form of the critical geometry relationship states that for any shape other than the right solid circular cylinder, four times the cross sectional area of the critical sample, divided by its total perimeter, equals 92% of the critical diameter. The minimum shock pressure required to initiate detonation of composite propellant is estimated to be 25 to 30 kbar for a critical size sample, and 8 to 10 kbar for an ideal diameter sample. A study of the effect of pulse width on the minimum initiating shock pressure for 4-in. diameter samples of an adulterated propellant showed that with a 2mm pulse the minimum pressure is between 50 and 64 kbar, and that the minimum pressures approach a lower limit of 26 to 32 kbar as the pulse width increases. New techniques were developed to prepare and characterize porous and cracked propellant samples. Correlations of the blast and fireball data from 22 propellant tests have been made. The average TNT equivalence of the peak overpressure data is 197%. The average TNT equivalence of the positive-phase impulse data is 138%, for those samples that detonated.		

DD FORM 1 JAN 64 1473

UNCLASSIFIED

Security Classification

This Document  
Reproduced From  
Best Available Copy

**UNCLASSIFIED**

**Security Classification**

14	KEY WORDS	LINK A		LINK B		LINK C	
		ROLE	WT	ROLE	WT	ROLE	WT
Propellant Hazards Critical Geometry Jetting Phenomena Critical Diameter Sensitivity SOPHY Porosity Blast Fireball							
<b>INSTRUCTIONS</b>							
1. ORIGINATING ACTIVITY: Enter the name and address of the contractor, subcontractor, grantees, Department of Defense activity or other organization (corporate author) issuing the report.							
2a. REPORT SECURITY CLASSIFICATION: Enter the overall security classification of the report. Indicate whether "Restricted Data" is included. Marking is to be in accordance with appropriate security regulations.							
2b. GROUP: Automatic downgrading is specified in DoD Directive 5200.10 and Armed Forces Industrial Manual. Enter the group number. Also, when applicable, show that optional markings have been used for Group 3 and Group 4 as authorized.							
3. REPORT TITLE: Enter the complete report title in all capital letters. Titles in all cases should be unclassified. If a meaningful title cannot be selected without classification, show title classification in all capitals in parenthesis immediately following the title.							
4. DESCRIPTIVE NOTES: If appropriate, enter the type of report, e.g., interim, progress, summary, annual, or final. Give the inclusive dates when a specific reporting period is covered.							
5. AUTHOR(S): Enter the name(s) of author(s) as shown on or in the report. Enter last name, first name, middle initial. If military, show rank and branch of service. The name of the principal author is an absolute minimum requirement.							
6. REPORT DATE: Enter the date of the report as day, month, year, or month, year. If more than one date appears on the report, use date of publication.							
7a. TOTAL NUMBER OF PAGES: The total page count should follow normal pagination procedures, i.e., enter the number of pages containing information.							
7b. NUMBER OF REFERENCES: Enter the total number of references cited in the report.							
8a. CONTRACT OR GRANT NUMBER: If appropriate, enter the applicable number of the contract or grant under which the report was written.							
8b, 8c, & 8d. PROJECT NUMBER: Enter the appropriate military department identification, such as project number, subproject number, system numbers, task number, etc.							
9a. ORIGINATOR'S REPORT NUMBER(S): Enter the official report number by which the document will be identified and controlled by the originating activity. This number must be unique to this report.							
9b. OTHER REPORT NUMBER(S): If the report has been assigned any other report numbers (either by the originator or by the sponsor), also enter this number(s).							
10. AVAILABILITY/LIMITATION NOTICES: Enter any limitations on further dissemination of the report, other than those imposed by security classification, using standard statements such as:							
(1) "Qualified requesters may obtain copies of this report from DDCI."							
(2) "Foreign announcement and dissemination of this report by DDCI is not authorized."							
(3) "U. S. Government agencies may obtain copies of this report directly from DDCI. Other qualified DDCI users shall request through"							
(4) "U. S. military agencies may obtain copies of this report directly from DDCI. Other qualified users shall request through"							
(5) "All distribution of this report is controlled. Qualified DDCI users shall request through"							
If the report has been furnished to the Office of Technical Services, Department of Commerce, for sale to the public, indicate this fact and enter the price, if known.							
11. SUPPLEMENTARY NOTES: Use for additional explanatory notes.							
12. SPONSORING MILITARY ACTIVITY: Enter the name of the departmental project office or laboratory sponsoring (paying for) the research and development. Include address.							
13. ABSTRACT: Enter an abstract giving a brief and factual summary of the document indicative of the report even though it may also appear elsewhere in the body of the technical report. If additional space is required, a continuation sheet shall be attached.							
It is highly desirable that the abstract of classified reports be unclassified. Each paragraph of the abstract shall end with an indication of the military security classification of the information in the paragraph, represented as (TS), (SI), (C), or (U).							
There is no limitation on the length of the abstract. However, the suggested length is from 150 to 225 words.							
14. KEY WORDS: Key words are technically meaningful terms or short phrases that characterize a report and may be used as index entries for cataloging the report. Key words must be selected so that no security classification is required. Identifiers, such as equipment model designation, trade name, military project code name, geographic location, may be used as key words but will be followed by an indication of technical context. The assignment of links, rules, and weights is optional.							

GEN REG-531

**UNCLASSIFIED**

**Security Classification**